Detection of Neutrinos from Gamma-Ray Bursts

Cover: Jeannette van Bergen, Rotterdam © 2005 jeannettevanbergen@planet.nl

Detection of Neutrinos from Gamma-Ray Bursts

ACADEMISCH PROEFSCHRIFT

TER VERKRIJGING VAN DE GRAAD VAN DOCTOR
AAN DE UNIVERSITEIT VAN AMSTERDAM
OP GEZAG VAN DE RECTOR MAGNIFICUS
PROF.MR. P.F. VAN DER HEIJDEN
TEN OVERSTAAN VAN EEN DOOR HET COLLEGE VOOR PROMOTIES
INGESTELDE COMMISSIE, IN HET OPENBAAR TE VERDEDIGEN
IN DE AULA DER UNIVERSITEIT
OP DONDERDAG 7 JULI 2005, TE 11:00 UUR

door

Maria Constance Bouwhuis

geboren te Eindhoven

Promotor:	Prof. Dr. K.J.F. Gaemers
Co-promotor:	Dr. M. de Jong

Faculteit der Natuurwetenschappen, Wiskunde en Informatica

Contents

Introduction

The common way to study astrophysical sources is by the detection of electromagnetic radiation. Most of the knowledge we have about these sources is obtained in this way. However, photons are not in every respect the most suitable particles to study astrophysics. There are regions in the Universe from which photons cannot escape. Photons can also be absorbed on their way to the Earth. An alternative way to study astrophysical sources is by the detection of cosmic neutrinos. Neutrinos interact weakly with matter. Dense regions of matter can be traversed by neutrinos but not by photons. Because neutrinos carry no charge, they are not deflected by magnetic fields. This means that once a cosmic neutrino is detected and its direction is determined, its origin can be found.

The only cosmic neutrinos that have been detected so far are neutrinos from the Sun and from the supernova SN 1987a. The detection of neutrinos from this supernova by the Kamiokande II [1] and IMB [2] detectors shows that a large amount of energy is released by supernovae in the form of neutrinos. The combined results from the detection of solar neutrinos by the Homestake, SuperKamiokande, and SNO detectors confirmed the solar model [3], and lead to the discovery of neutrino oscillations [4]. The detected cosmic neutrinos have energies of the order of a few MeV. Several other experiments are dedicated to the detection of cosmic neutrinos at these energies (see for a review [5]).

From the detection of high-energy cosmic rays, it is suggested that in some astrophysical sources particles are accelerated to very high energies [6]. When protons are accelerated, high-energy neutrinos could be produced. Candidate sources of these cosmic accelerators include gamma-ray bursts, active galactic nuclei, supernova remnants, and microquasars. Gamma-ray bursts (GRBs) are the prime sources considered in this work, and they are described in chapter 1. Many GRBs have been detected up to now by satellites capable of detecting high-energy gamma rays. GRBs and their counterparts have extensively been studied by the observation of the electromagnetic radiation they emit in a broad wavelength range. The origin of a GRB and the processes taking place during the burst that give rise to the observed radiation are poorly understood. Most likely things will remain unclear as long as only electromagnetic radiation is observed. Considering the energy involved, and the assumption that protons are being accelerated, high-energy neutrinos could be produced. The detection of neutrinos from GRBs would give more insight into the origin of GRBs and the processes taking place.

With a new generation of neutrino detectors the objective is to detect high-energy cosmic neutrinos. These detectors are much larger than the ones mentioned above. They can be considered as a telescope as they are capable of determining the direction of a neutrino. Several such telescopes have been (or are) operating, like AMANDA [7], Baikal [8], and NESTOR [9]. The ANTARES neutrino telescope that will become operational in the near future is considered in this work. The detection principle and a description of the ANTARES detector are given in chapter 2. In the future, neutrino telescopes will be constructed that are even larger [10, 11].

GRBs occur at random times and at various positions in the sky. They are usually detected when the right part of the sky is monitored by a GRB satellite. Astronomers have developed warning systems that immediately announce the detection of a GRB by such a satellite. These messages are distributed quickly around the world to increase the chance to observe the GRB on Earth with a telescope. As the GRB lasts only for about a minute, and its counterpart, which is observable on Earth, fades quickly, a fast distribution of this message with the position of the GRB on the sky is crucial. A possible neutrino signal produced by a GRB is expected to arrive in coincidence with the observed gamma rays. Although a neutrino telescope takes data in the same way 24 hours a day, a special way of data taking can be applied during short periods, like during a GRB. This is only possible when the readout of the detector can be triggered by these GRB warning systems. The ANTARES detector is currently the only neutrino telescope that makes use of such systems. The design of the readout system of the ANTARES telescope, described in detail in chapters 3 and 4, is such that it can be triggered by these warning systems. It can save all data during a GRB instantaneously when a GRB is announced. The knowledge of the position of the GRB, and thus the direction of the neutrinos, is used to analyse these data. In general, as neutrinos can come from anywhere, a neutrino telescope is built in such a way that it is sensitive to neutrinos from (almost) all directions. For the data taken during a GRB, a special analysis procedure has been developed, described in detail in chapters 4 and 5, that looks for neutrinos from a particular direction. This results in a high detection efficiency.

The performance of the methods developed and described in this work is quantified in chapter 6. It is shown that these methods increase the discovery potential for neutrinos from GRBs considerably compared to other methods. Obviously, also other transient sources with a duration similar to that of a GRB and that are detected by satellites can be analysed in this way. In chapter 6 it is also shown how non-transient sources for which the position on the sky is known can be followed. Not just for neutrinos from GRBs, but also for neutrinos from any source for which the direction is known, the detection efficiency will be increased with the methods described in this work.

Chapter 1

Gamma-ray bursts

Gamma-ray bursts are very short and intense flashes of MeV gamma rays at various locations in the sky and at random times. The observations made in the last decade in the research of gamma-ray bursts have led to the development of various models. The aim of these models is to describe what causes these apparent explosions and which processes take place during the explosion that lead to the observations. There is a rich variety in timescales and spectra observed in gamma-ray bursts. This diversity is poorly understood. The prevailing model suggests that a specific type of these bursts is related to the collapse of a massive star, possibly accompanied by the formation of a black hole. However, it is not certain that all gamma-ray bursts can be explained this way.

In most models it is assumed that baryonic matter plays an important role during the burst. Because this matter is ejected at relativistic speeds during the burst, it is generally believed that protons are accelerated up to very high energies. These particles can interact and produce charged pions, which in their decay produce neutrinos. The detection of these neutrinos would give more insight in the origin of gamma-ray bursts and the processes taking place during the explosion.

The prompt emission of the gamma rays lasts for about a minute. The models that describe the gamma-ray bursts are partly based on the observations of the so-called afterglow, which can last for a much longer period. The afterglow is the emission of radiation at other wavelengths, subsequent to the emission of the MeV gamma rays. The intensity of the afterglow decays rapidly. To detect it, knowledge of the accurate location of the burst is required as soon as possible after its detection to be able to point a ground based telescope in that direction. For this purpose, warning systems have been developed that distribute a warning of the burst occurrence and its location quickly around the world. Such systems offer a great potential for neutrino telescopes as well, as the same feature holds for neutrinos from these sources: they most likely arrive close to the moment the gamma rays are detected. The ANTARES neutrino telescope will be the first neutrino experiment that will use these systems in the same way: it will look in the direction of the gamma-ray burst at the moment it occurs.

1.1 GRB characteristics

Gamma-ray bursts were discovered by accident with the Vela satellite system in the late 1960s [12]. In the data of the X-ray and gamma-ray detectors onboard these widely separated satellites a short burst of gamma rays was observed sixteen times in a period of three years. Each of these bursts was detected in a coincidence between at least two of the four satellites. The photons were detected in the energy range from 0.2 MeV to 1.5 MeV. The burst durations varied from less than 0.1 second to 30 seconds, and their fluences from 10^{-5} erg cm^{-2} to 2×10^{-4} erg cm^{-2} †. The detailed time structure of each burst was observed in the data of all satellites that detected it. From the directional information the Sun and Earth were excluded as the sources of these bursts. These unexplained phenomena were named gamma-ray bursts (GRBs).

Since then other gamma-ray instruments on various satellites detected these transient events, but no celestial object could be identified as the prime source. The Compton Gamma Ray Observatory [13], launched in 1991, had the BATSE detector on board, which was especially designed for GRB observations. It operated for about nine years and detected nearly 3000 GRBs. The observations of these GRBs gave more insight in the characteristics of GRBs in addition to what was observed with the Vela satellites. The GRBs show a wide variety in duration, intensities, and time profiles. Figure 1.1 shows the light curves of some GRBs detected by BATSE. Each GRB seems to produce a different signal. The detected photons have energies ranging from about 1 keV to a few GeV. GRBs generally show a hard photon spectrum. Most of the measured gamma-ray fluences are in the range from 10^{-6} erg cm^{-2} to 10^{-4} erg cm^{-2}.

BATSE could determine the location of GRBs with an accuracy no better than 2°. The locations of the GRBs showed an isotropic distribution in the sky [15]. The results from BATSE also showed that the durations of GRBs range from about 30 milliseconds to over 1000 seconds. The distribution of burst durations is shown in figure 1.2. Based on the observed durations two types of GRBs were classified: long (longer than 2 seconds) and short (shorter than 2 seconds) bursts [16]. About one third of the bursts are short. The two types of GRBs can also be differentiated by their photon spectrum. For both types the distribution of the hardness ratio, which is defined as the ratio of the total photon count in a high and low energy range, is shown in figure 1.2. Short bursts, indicated by the dashed line, have on average a harder spectrum than long bursts.

For a better understanding of the origin of GRBs a longer observation time is required. This can be done by detecting the radiation at other wavelengths (X-ray, optical, and radio) that is emitted by the GRB subsequent to the initial burst. This phenomenon is known as the afterglow of the GRB. The detection of the afterglow is done with more sensitive instruments that detect photons at other wavelengths than MeV gamma rays, and that can be pointed in the direction of the GRB. For this the

---

[†] In the GRB literature the energy is usually expressed in the unit erg (1 erg ≡ 10^{-7} J).

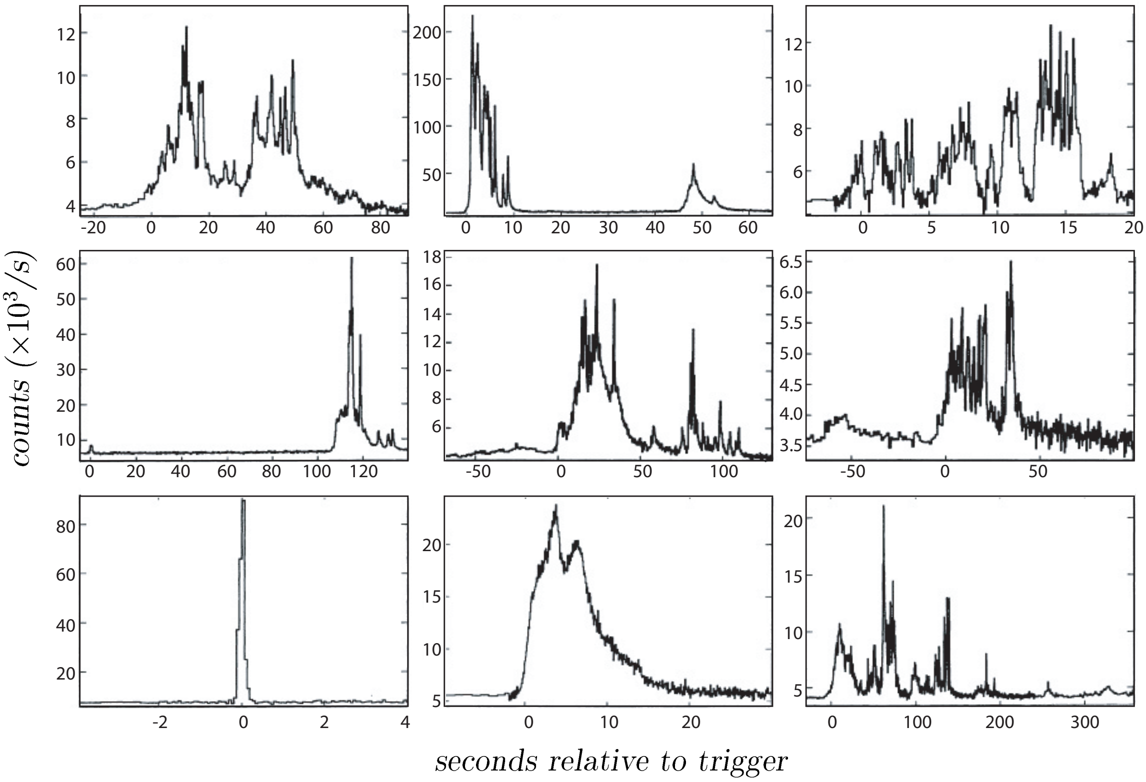

Figure 1.1: *Light curves of different GRBs detected by BATSE [14].*

location of the GRB has to be known accurately. As the intensity of the X-ray and optical afterglow of a GRB decays rapidly, these follow-up observations have to be done quickly after the detection of the burst. The BeppoSAX satellite [17], launched in 1996, was able to localise a GRB with an accuracy of about 3 arcminutes. This feature, combined with the fast distribution of the notification of a GRB event with its location (see section 1.4) made it possible to detect the afterglow of a GRB at different wavelengths [18].

By observing the GRB afterglow it is in principle possible to determine the redshift, and thus the distance of the GRB. The redshift is determined from the wavelengths of the absorption and emission lines in the spectrum [19]. Shortly after the discovery of the afterglow also the redshift of a GRB was determined for the first time [20]. This was the proof that GRBs are at cosmological distances. Figure 1.3 shows the distribution of measured redshifts (z) of 41 GRBs. The mean redshift is 1.3, which corresponds to a distance of about 2.5 Gpc[†]. Afterglows have up to now only been observed for long bursts. Very little additional information on short bursts has been obtained since their discovery.

The detection of a GRB in coincidence with a supernova explosion lead to the conclusion that there is a connection between long GRBs and supernovae. Such a

---

[†] This is about 7×10^{25} m. For comparison, the Galaxy is about 30 kpc across.

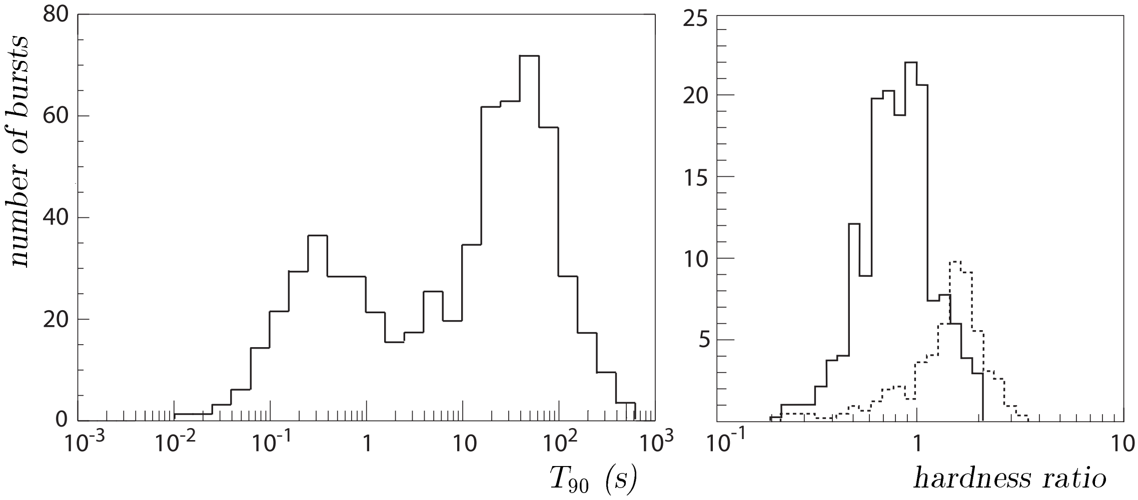

Figure 1.2: *Left: The bimodal distribution of the durations of GRBs detected by BATSE. The duration of the GRB, indicated by T_{90}, is defined as the time interval during which 90% of the photons were detected. Right: The distribution of the hardness ratio of the long (solid line) and short (dashed line) bursts. The hardness ratio is defined as the ratio of the total photon count in the 100–300 keV and 50–100 keV energy ranges.*

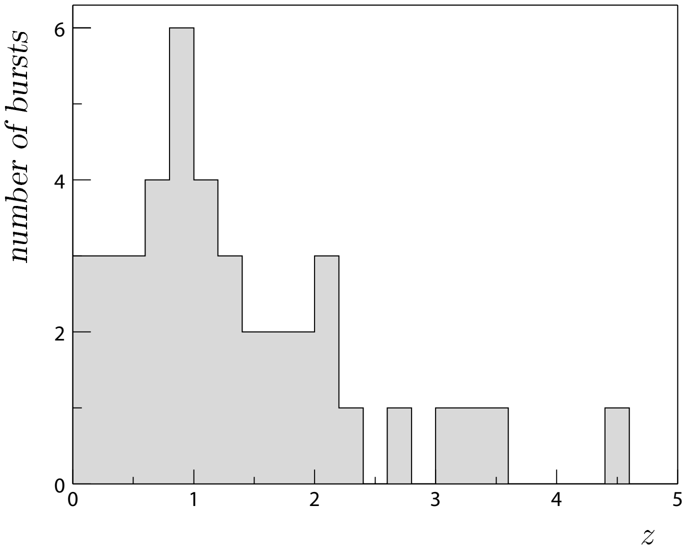

Figure 1.3: *Distribution of the measured redshifts (z) of 41 GRBs.*

coincidence was noticed with the detection of the supernova SN 1998bw in coincidence with GRB 980425[†] [21], and SN 2003dh in coincidence with GRB 030329 [22], a GRB that will be considered in detail later in this work. In both these cases the supernova explosion was classified as a hypernova, which is the core collapse of a very massive star.

[†] GRBs are named after their date of detection (GRB yymmdd).

1.2 GRB models

Even before the discovery of GRBs by the Vela satellite system a theory was proposed that supernovae would give rise to a phenomenon similar to what is now called a GRB. Since their discovery and the many GRB observations made so far, several models were developed that describe the possible origin of the GRBs and the processes that produce the observed emission of radiation. An extensive overview of the developments in this field can be found in [23]. The most widely accepted model that describes the actual emission of radiation of the GRB is the fireball model in combination with the internal/external shock model, described in detail in [24]. A short description of the assumed sources of GRBs, as well as the commonly accepted model of GRBs is given in the following sections. An alternative model that describes the observed GRB prompt and afterglow emission is also given.

1.2.1 Sources of GRBs

The above-mentioned association of long GRBs with supernovae resulted in the general belief that these GRBs are caused by hypernovae. The underlying model is the so-called collapsar model [25]. In the collapsar model the core of a rapidly rotating massive star collapses and forms a rapidly rotating black hole surrounded by an accretion disc consisting of leftover material. From the accretion disc two opposite jets arise that cause the GRB. It is however not clear if all GRBs can be associated with supernovae. Especially short bursts may be caused by compact binary mergers [26]. In this model a binary system consisting of two compact objects, like a neutron star and a black hole, or two neutron stars, spiral towards each other and merge into one. This could also result in the formation of a black hole surrounded by an accretion disk. Each of the models is believed to give rise to the production of radiation in accordance with the observations of GRBs.

1.2.2 The fireball model

Regardless of what mechanism actually initiates the GRB, the GRB itself is believed to be caused by a jet of material moving at relativistic speeds. The processes taking place within this jet give rise to the production of radiation. The assumed jetted outflow of the GRB is based on the distance of the GRB and the observed fluence. The total energy emitted in gamma rays ranges from 10^{51} erg to 10^{54} erg[†]. This enormous amount of energy release emitted by a single source made the early models that assumed an isotropic explosion of the GRB questionable. Nowadays the outflow of the inner engine is presumed to be collimated into a small solid angle, which reduces the total energy output [27].

The jet is believed to be formed by a very compact object consisting of a plasma of photons, electrons, positrons, and baryonic matter. The matter originates from

---

[†] For comparison: the solar luminosity is about 10^{41} erg in one year.

the source that produces the compact object. The initial energy density near the compact object is very high. The high energy density requires a temperature higher than 1 MeV, so most of the energy is concentrated in a very over-pressured e^+e^-–photon plasma, called the fireball. Due to the large pressure the fireball starts to expand. An explosion takes place and a shell of particles moving at relativistic speeds is ejected from the compact object. In a jetted outflow the fireball explosion is collimated by a surrounding torus of material. With the expansion, the internal energy of the fireball is converted into kinetic energy of a cold, expanding shell, or a collection of shells in which the thermal energy of the e^+e^-–photon plasma has been transferred to the baryons. Finally the expanding material becomes optically thin and the photons can escape.

1.2.3 The shock model

When the ejected shell has expanded to a sufficiently large radius, its kinetic energy can be converted into internal energy such that the charged particles emit radiation. To convert the kinetic energy back into internal energy the flow of the shell must be slowed down. This is proposed in the internal and external shock models [28, 29].

In the internal shock model many shells are ejected by the compact object. The Lorentz factors of the shells depend, among other things, on the amount of matter they contain. As a result, each shell has a different Lorentz factor. A late but faster shell can collide with an early slower shell. When they collide an internal shock is produced. This is visualised schematically in figure 1.4. Via the relativistic shock acceleration mechanism, charged particles in the shells can be accelerated further [30]. A charged particle can cross the shock front. On the other side of

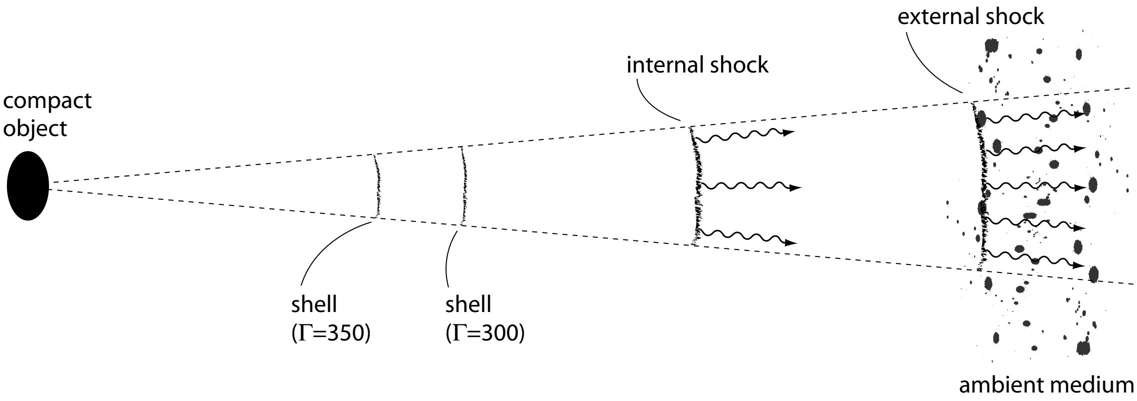

Figure 1.4: *Schematic view of the internal/external shock models. Internal shocks are produced when two shells with different Lorentz factors (*Γ*), ejected by the compact object, collide. This shock gives rise to the GRB prompt emission. The external shock is produced when the ejected shells run into the ambient medium. The radiation produced in external shocks has a broad range of wavelengths and is observed as the GRB afterglow.*

the shock front it can be scattered by inhomogeneities or bent by (local) magnetic fields, and cross the shock front again. Each time a particle crosses the shock front it gains energy. The accelerated particles will emit gamma rays through synchrotron radiation and possibly through inverse Compton scattering. The radiation of high-energy gamma rays is observed as the prompt emission of the GRB.

The ejecta continue to move outward and run into the ambient medium, which can be the interstellar medium, or a stellar wind that was emitted earlier by the source that produced the compact object. The external shocks are the collisionless shocks produced when the ejecta interact with this medium. This interaction takes the form of a pair of shocks: a forward shock or blast wave driven into the ambient medium by the ejecta, and a reverse shock propagating back into the ejecta. In the forward shock the ambient medium is accelerated and heated, and kinetic energy is converted into internal energy. As the energy is shared between the charged particles (electrons and protons), the electrons are accelerated again to relativistic speeds. As a result they will emit synchrotron radiation. When the shell sweeps up more and more matter of the ambient medium its Lorentz factor decreases further. This gives rise to the emission of radiation at lower energies. The emission of X-ray, optical, and radio photons caused by the forward shock can last for a long period and is observed as the afterglow. The reverse shock can produce a short and extremely bright optical flash due to synchrotron emission from electrons accelerated in the reverse shock [31]. This observation suggests that some energy is ejected from the compact object in the form of proton kinetic energy, as the observed radiation is compatible with a shock propagating into a fireball composed of protons, positrons, and electrons, rather than positrons and electrons.

The variability in the light curves can be explained with the internal and external shock models. In the internal shock model the emission is produced each time two ejected shells collide. In the external shock model the variability is attributed to irregularities in the ambient medium. Each time the ejecta run into a higher density environment, a peak is produced in the emission.

When assuming a jetted outflow, the radiation produced can only be observed when the jet is pointed in the direction of the gamma-ray detectors. This implies that GRBs occur at a much higher rate than the current detection rate.

1.2.4 The cannonball model

In the cannonball model [32] large objects consisting of atomic matter with a mass comparable to that of the Earth, called cannonballs, are ejected from the compact object. The compact object is believed to be produced by a supernova core collapse. Like in the collapsar model, the compact object is surrounded by an accretion disk that consists of matter from the collapsed star. Each time part of the matter from the accretion disk falls into the compact object, it is emitted as a single cannonball. The cannonballs travel with relativistic speeds into the ambient medium, which includes the supernova shell. When they propagate through the supernova shell and the interstellar medium, photons are produced which are observed as the GRB and afterglow respectively. Each pulse in the light curve of a GRB corresponds to one cannonball. The sequence of the individual pulses in the light curve, and thus the sequence of the emission of cannonballs, reflects the chaotic behaviour of the accretion disk.

1.3 Neutrino production in GRBs

In the proposed models it is generally believed that charged particles are accelerated to high energies to explain the emission of high energy photons. Among these particles are electrons, positrons, and protons. The protons can interact with photons –already present in the medium, or emitted by synchrotron radiation– and produce charged and neutral pions. Via inelastic $p - p$ or $p - n$ collisions, also $\pi^{\pm}$ and π^0 particles can be produced. The decay of π^0 leads to a photon signal, whereas the decay of charged pions leads to the production of neutrinos

$$\begin{array}{rcl} \pi^0 & \rightarrow & \gamma + \gamma \\ \pi^+ & \rightarrow & \mu^+ + \nu_\mu \rightarrow e^+ + \nu_e + \bar{\nu}_\mu + \nu_\mu \\ \pi^- & \rightarrow & \mu^- + \bar{\nu}_\mu \rightarrow e^- + \bar{\nu}_e + \nu_\mu + \bar{\nu}_\mu \end{array} \tag{1.1}$$

At very high energies ($\sqrt{s} \gg \mathrm{m}_\pi$) the three types of pions are produced in equal amounts because of the isospin symmetry of the strong interaction.

From a comparison between the arrival time and duration of the neutrino signal and the photon signal, models of neutrino production in GRBs can be excluded.

1.3.1 Inelastic collisions

According to the collapsar model, the collapse of a massive star gives rise to the GRB. The jet that produces the observed radiation is formed inside the star. As long as the jet is inside the star it produces no observable gamma rays. During this period it is called the substellar jet [33]. Protons that are accelerated in this jet can collide with protons and neutrons in the jet or star that are not accelerated. Neutrinos result from these collisions and escape, but the characteristic gamma-ray signal can only escape once the jet has broken out of the star. If there is such a gamma-ray signal, the neutrinos produced by this mechanism precede the gamma rays by about 10–100 seconds.

In both the fireball and cannonball models $p - p$ collisions are anticipated when the material ejected from the compact object collides with the emitted supernova shell. In the cannonball model this is the only neutrino production mechanism [34]. When the relativistic cannonball penetrates the supernova shell, the nucleons in the cannonball collide with the nucleons in the supernova shell and in this way produce pions. Neutrinos are produced by the decay of these pions. The gamma rays are also produced when the cannonball collides with the supernova shell, but they are only observable when the cannonball reached the outer layers of the shell. Only at this stage the photons can escape. Neutrinos however penetrate this shell and are observable from the moment the cannonball hits the shell. The neutrino pulse duration is expected to be a fraction of the gamma-ray burst duration, and it precedes the high-energy gamma-ray emission with a time comparable to the duration of the GRB.

In the fireball model the neutrino signal from $p-p$ collisions due to the collision of an ejected shell with the supernova shell is believed to be coincident with the GRB and of similar duration [35]. Several other mechanisms suggest $p-p$ or $p-n$ collisions in the GRB jet, see for example [36, 37]. The resulting neutrinos are also assumed to be produced in coincidence with the GRB prompt emission.

1.3.2 Photomeson production

The highest energy neutrinos are believed to be produced by $p-\gamma$ interactions. This interaction takes place via the Δ^+ resonance. The centre of mass energy of the photon and proton has to be sufficiently high to produce a Δ^+. The Δ^+ decays into a nucleon and a pion

$$\begin{aligned} \Delta^+ &\rightarrow n+\pi^+ \\ \Delta^+ &\rightarrow p+\pi^0 \end{aligned} \tag{1.2}$$

The probability that the Δ^+ decays into a p and a π^0 is twice the probability that it decays into a n and a π^+. These interactions occur in the internal shocks and external shocks of ejected shells, and inside the collapsed star. In the internal shocks MeV photons can be produced by the synchrotron radiation emitted by particles accelerated by the same shocks. The interaction rate between the photons and protons is high due to the high density of photons, and leads to a significant production of pions [38]. The neutrinos that result from the decay of these pions are in coincidence with the prompt gamma-ray emission of the GRB.

In the reverse shock –the shock that propagates back into the ejecta– electrons are re-accelerated and radiate photons which are observed in the 10 eV–1 keV energy range. Protons accelerated to a very high energy can interact with these photons and produce Δ^+ particles. This will result in the production of very high energy neutrinos [39]. The neutrino production in the reverse shock occurs during a period similar to that of the GRB. It follows the neutrino signal produced in the internal shocks (and thus the prompt gamma-ray emission) after a time comparable to the duration of the GRB. Neutrinos can also be produced by $p-\gamma$ interactions when the ejected shell meets the supernova shell of the collapsed star [35].

In the substellar jet also $p-\gamma$ interactions take place. While the jet is finding its way out of the star it produces X-rays with a typical energy of 1 keV [33]. In the substellar jet internal shocks take place that accelerate protons. These protons interact with the X-ray photons to produce Δ^+ particles and subsequently high energy neutrinos. This neutrino signal will precede the observable gamma-ray signal by 10–100 s. If the jet does not break through the star, these neutrinos cannot be announced by an observable gamma-ray signal.

1.3.3 Neutrino fluxes

In figure 1.5 the calculated ν_μ and $\bar{\nu}_\mu$ fluxes at Earth from GRB 030329 and the associated supernova SN 2003dh are shown, taken from [40]. These fluxes will be used

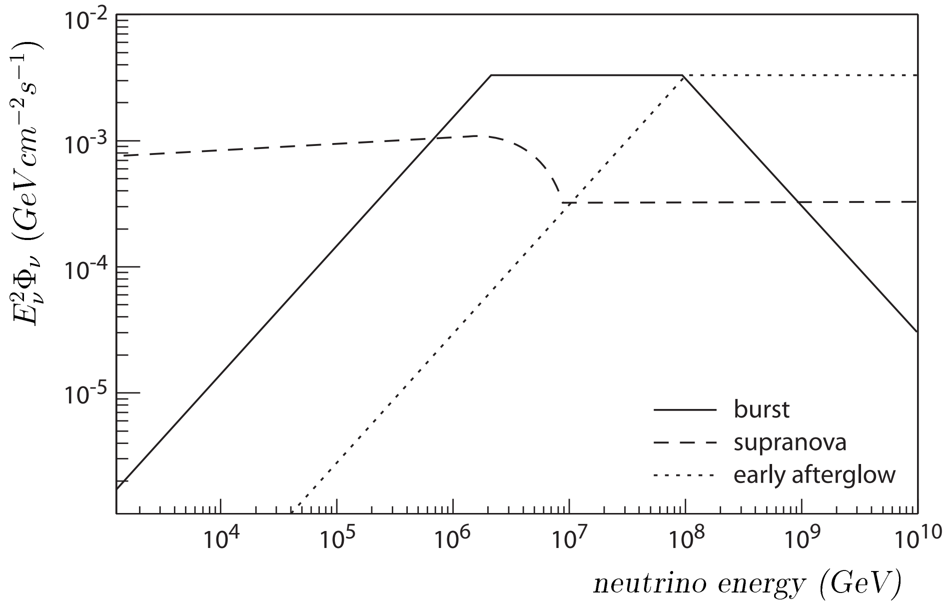

Figure 1.5: *The ν_μ and $\bar{\nu}_\mu$ fluxes at Earth from GRB 030329 and the associated SN 2003dh as a function of the neutrino energy. Indicated are the neutrino fluxes from $p-\gamma$ interactions in the internal shocks (solid line), $p-p$ and $p-\gamma$ interactions when the ejected shells collide with the supernova shell (dashed line), and $p-\gamma$ interactions when the ejected shells collide with the ambient medium (dotted line). For the arrival times of the neutrinos with respect to the GRB see text.*

to calculate the discovery potential of a neutrino signal from GRBs for ANTARES. Several other calculations of neutrino fluxes from GRBs exist [41, 34, 42, 43, 44, 45, 46, 47]. The observed duration of the GRB was about 30 seconds. The scenario is chosen where a supernova shell is ejected from the collapsing star about 2 days before the GRB event [22]. It is assumed that the ambient medium consists of a high density wind, ejected earlier by the massive star. Neutrino oscillations are taken into account. Above 10^{10} GeV the neutrino flux is strongly suppressed as no protons are expected to be accelerated to energies much higher than that.

The figure includes the neutrino fluxes produced during the prompt gamma-ray emission phase (burst), when the ejecta meet the supernova shell (supranova), and when the ejecta meet the ambient medium (early afterglow). The sum of these fluxes can be considered as the total neutrino flux from this GRB. The neutrino flux produced by the substellar jet finding its way out of the star is not included. The presence of such a component in the scenario that a supernova shell was ejected a few days before the GRB event is uncertain. If this component is present, its contribution is expected to be very small.

The neutrino flux labeled burst is due to $p-\gamma$ interactions in the internal shocks. The neutrino spectrum is determined by the proton and gamma-ray spectra. The observed gamma-ray spectrum is well described by a broken power law [48]

$$\frac{dN_\gamma}{dE_\gamma} \propto E_\gamma^{-\beta} \tag{1.3}$$

where E_γ is the photon energy and β is the spectral index. A break point at 0.5 MeV was observed for this GRB. Below this energy $\beta \simeq 1$, and above this energy $\beta \simeq 2$. The accelerated protons are assumed to follow an E^{-2} spectrum. The interactions of the protons with the GRB photons result in a broken power law neutrino spectrum. The break point of the neutrino flux is then fixed at 2×10^6 GeV due to the threshold energy of the Δ^+ resonance. Below this energy the neutrino flux can be described with an E^{-1} spectrum, above this energy with an E^{-2} spectrum. At energies higher than 10^8 GeV the neutrino production is suppressed due to the synchrotron radiation of the charged pions and secondary muons. During this phase also the observable gamma rays are produced. The assumed neutrino flux is therefore coincident with the gamma rays, and lasts for a period comparable to the GRB duration.

The neutrino flux labeled supranova is due to interactions of the protons accelerated by the internal shocks with the supernova shell. Protons with an energy below the photo-production threshold of Δ^+ can interact with protons in the supernova shell. Neutrinos with an energy of 10^7 GeV or more can be produced via $p-\gamma$ interactions by protons that escaped the internal shocks with the thermal photons in the supernova shell. At these energies the neutrino flux follows the E^{-2} proton spectrum. Due to a smaller magnetic field inside the supernova shell compared to that in the internal shock, the synchrotron radiation of pions and secondary muons is reduced. As a consequence, the neutrino flux is not suppressed at very high energies. The duration of this neutrino signal is comparable to the duration of the neutrino burst signal. These signals are expected to overlap in time.

The neutrino flux labeled early afterglow arises when the ejecta run into the ambient medium. The medium is here assumed to be composed of a high density stellar wind that was emitted by the massive star prior to its collapse. This causes a reverse shock. The accelerated protons can interact with photons produced by the reverse shock. For this GRB however the reverse shock was not observed. The characteristic reverse shock photon spectrum was taken. Because of the energy of the optical photons (few eV) the protons require a high energy to produce Δ^+ particles. The neutrino production during the early afterglow is not suppressed at very high energies as the magnetic fields are smaller in the ambient medium, and hence the pion synchrotron radiation is suppressed. The neutrino signal during the early afterglow follows the neutrino burst signal in time as the reverse shock takes place after the internal shocks. Its duration is comparable to the GRB duration. After this only the forward shock into the ambient medium survives.

1.4 GRB warning systems

A failure on the Compton Gamma Ray Observatory (CGRO) lead to the development of the first GRB warning system. The instruments on CGRO, including BATSE, recorded their data on board on a tape recorder. Data covering several hours were transmitted to ground. After the failure of the tape recorders, shortly after the launch of CGRO, it was decided to transmit the data to ground in real time instead. The data were coming in as the burst was still happening. By doing a quick automated analysis of the BATSE data on ground, a rough position of the GRB could be calculated. At first these positions were distributed to the world over telephone lines, later also using the Internet. This system was called the BATSE Coordinates Distribution Network (BACODINE). The very approximate positions were used to try to find the GRB counterparts with ground based telescopes. Scientists anywhere in the world could find out the position of a burst within 5 seconds of its detection by BATSE, when the majority of the bursts was still going on.

The BACODINE system was maintained, and even expanded to incorporate the distribution of GRB announcements that were detected by other satellites capable of detecting GRBs. The system was then renamed to GRB Coordinates Network (GCN) [49]. Another such system, the INTEGRAL Burst Alert System (IBAS), became operational with the launch of the INTEGRAL satellite, end of 2002. The Interplanetary Network (IPN) does not contribute to the real time distribution of the occurrence of detected GRBs, but distributes accurate GRB locations at a later time.

These GRB warning systems appear to be a successful way to observe GRBs. All satellites capable of detecting GRBs that were launched since BATSE became part of these systems, as will future GRB satellites. By subscribing to these systems, interested parties like ANTARES can be updated rapidly with the most recent GRB information. The distributed messages are made up of a predefined and documented format, depending on the satellite that triggered, and the message type. These formats enable the subscriber to extract the necessary information from the messages. All messages distributed through the GRB warning systems contain a unique ID that identifies the trigger. Often a trigger results in the distribution of several messages. With the ID the subscriber can recognise messages that belong to the same trigger. The functioning of the existing GRB warning systems, and the associated message types are described in the following sections.

The real time distribution of a location of a GRB is essential for the detection of the afterglow. As the afterglow fades quickly, a fast response is required to allow afterglow observations on ground. Moreover, an accurate location of the GRB is required to be able to point the telescopes in the right direction, since they have a limited field of view. As will become clear in the course of this thesis, the ANTARES experiment can also profit from GRB warning systems, provided that the initial message that a GRB is detected arrives within about 20 seconds after the detection of the burst. The maximum allowed delay depends mainly on the amount of raw data that can be buffered by the data acquisition system of ANTARES (see chapter 4). The buffering is done with the memories of the data processing PCs. With the standard PCs of today, a maximum delay of about 100 seconds is feasible. This can increase with the developments of standard PCs. A shorter delay is desirable to also cover a possible early neutrino signal prior to the detection of the photons. The location of the burst is not needed immediately. When the message with the GRB location arrives within 6 hours after the detection of the burst, sufficient time will be available to process the data before the next alert message arrives.

There has been a trade-off in the data handling of the GRB satellites that became operational since BATSE between getting an alert message within the shortest possible time, and desiring the most accurate results about the significance of the signal and the GRB location. After all, when the initial message is distributed too quickly, this often results in a false trigger. The decision taken for the Swift satellite to first try to determine the validity of the GRB event and the location of the GRB as accurately as possible, is at the expense of real time distribution of the initial GRB messages, but it prevents the distribution of many false triggers per day. The GRB community prefers to have more accurate information in the first message to be able to point telescopes sensitive for other wavelengths immediately in the right direction to observe the GRB afterglow. Unfortunately for ANTARES and other future neutrino telescopes, this will reduce the chance to detect neutrinos from GRBs.

1.4.1 GRB Coordinates network

The three most important satellites currently operational that have their GRB observations distributed by the GCN in real time are HETE [50], INTEGRAL [51], and Swift [52]. In the future the GLAST [53] and AGILE [54] satellites will become part of the system. The GCN distributes two types of messages: GCN Notices and GCN Circulars. The GCN Notices are the real time messages from the satellites. There are many different types of GCN Notices; for each satellite a set of message types is defined. For simplicity the GCN Notices are here divided into three subtypes: alert, update, and position messages. The alert messages are basically the first announcement that a GRB is detected, and should arrive very quickly after the detection of the first gamma rays. These messages can contain the location of the GRB, depending on the satellite. Update messages are distributed shortly after the alert message and contain updated information from the instruments onboard the satellite on the burst just detected. A location of the burst is provided, although it still might not be very accurate. Position messages are typically sent after the bursting period, and contain the best determined position known at that time. GCN Circulars are reports from ground based observers who did follow-up observations of a GRB. The GCN Circulars are provided by the observers themselves. They can be distributed via the GCN up to weeks after the GRB. The GCN Circulars may contain the duration of the burst, which is of great importance for the analysis of GRB data in ANTARES, as described in chapter 6.

All GCN Notices and Circulars are collected into a central location and automatically transmitted from there to all subscribers. There are different methods used to distribute the messages. The fastest way, that is also used by ANTARES, is an Internet socket connection. In this method there is a socket connection between the GCN and the site. A status check of this connection is done every 60 seconds. If necessary, the connection will be remade. In general it takes the messages less than 1 second to arrive at the site. All information distributed via the GCN is archived and accessible through the Internet.

The frequency at which alert messages were distributed by the GCN over the last few years is indicated in figure 1.6. At high frequencies the alert messages are mainly false triggers; they are distributed during short periods of high satellite trigger rates. There are periods in which the distribution of alert messages is restricted, for example during times when the particle density in the satellite's orbit is high [55]. Long delays in the delivery of an alert message from HETE are the result of significant interference during transmission of the data to ground, or when ground stations are offline. Most of the alert messages included in the figure were initiated by false triggers. For the triggers that appeared to be a GRB the time delay between the detection of the photons and the delivery of the alert message to

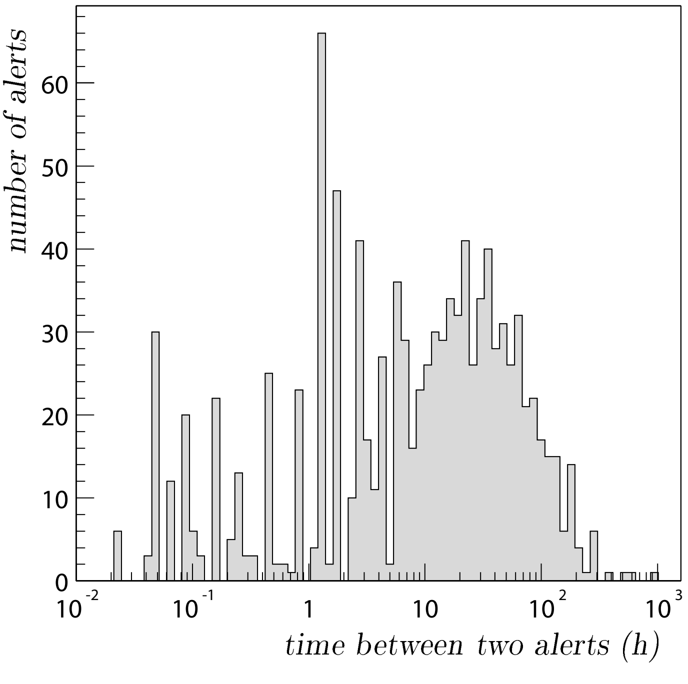

Figure 1.6: *Distribution of the time between the arrivals of the alert messages sent by the GCN. The figure includes all alert messages that were distributed by the GCN between 1/1/2001 and 1/1/2005.*

the GCN in seconds is given in figure 1.7. For 40% of these GRBs the delay was less than 20 seconds, and for 75% it was less than 100 seconds. Most of these GRBs were detected by HETE. The delay time includes the time to detect the burst, the transmission time, and the network delay to the central computer of the GCN. Not included is the time it takes the message to arrive at the site, but this takes less than 1 second when using the socket distribution method.

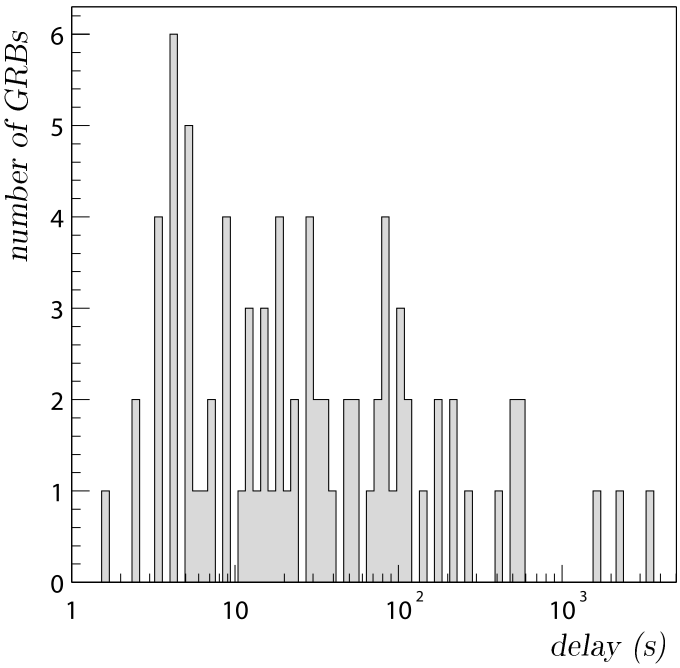

Figure 1.7: *Distribution of the delay between the detection of the GRB by the satellite and the time the alert message is distributed by the GCN. The figure includes all GRBs that were announced by the GCN in this way between 1/1/2001 and 1/1/2005.*

The GRBs included in the figure are about 30% of the total number of GRBs that were detected in the indicated period. The remaining GRBs were either not detected by satellites that have their GRB data distributed in real time, or that were below the threshold for the real time delivery, but were recognised as GRBs in the offline analysis, and announced much later.

If after ground analysis more or better information becomes available, this is also distributed through the GCN. Most GRBs that were detected in this way in this period were succeeded by such an offline message. The final location of the GRB, and the definite confirmation that it was a GRB might not be distributed at the same time. More accurate localisations may even be distributed after the GRB was already confirmed. In ANTARES the GRB analysis can start when it is confirmed that it was a real GRB, and when its position is known. Figure 1.8 shows the delay between the GRB trigger time and the time the GRB was confirmed and a location was known. For 70% of the GRBs included in the figure the location arrived within 6 hours after the detection of the burst. The location of the GRB that is distributed by the GCN is usually given with a precision of the order of arcminutes, which is accurate enough for ANTARES.

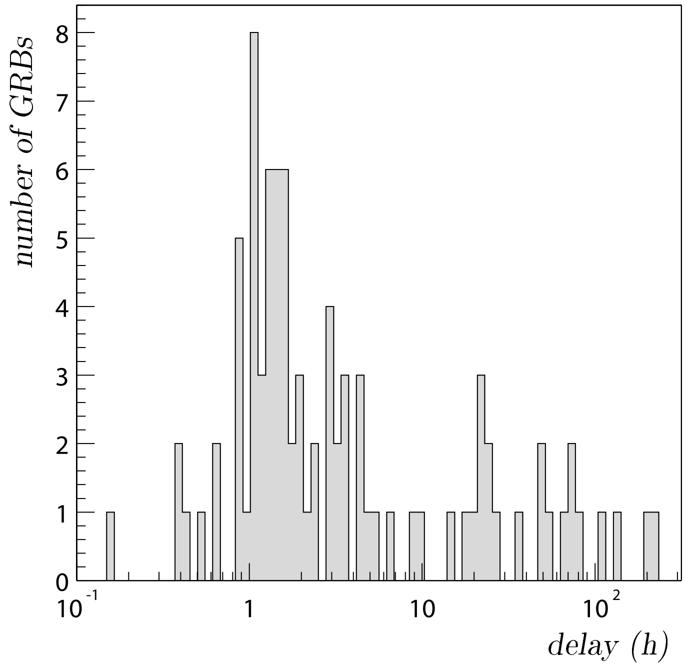

Figure 1.8: *Distribution of the delay between the detection of the GRB by the satellite and the time the GRB was confirmed and its position was distributed. The figure includes all GRBs that were announced by the GCN in this way between 1/1/2001 and 1/1/2005.*

Most of the GCN Notices and Circulars distributed in the indicated period contained data from HETE. This satellite is operational since 2000. Since that time it has been connected to the GCN. When the instruments onboard HETE are triggered by a photon counting rate above threshold, a message is transmitted to the nearest ground station. From there it is automatically sent over the Internet to the Mission Operations Centre (MOC, Massachusetts), and from there to the central location of the GCN (GSFC[†]). The alert message is immediately distributed via the GCN. During the next 4 minutes one or more update messages can be distributed that are sent by the onboard instruments and reach the MOC in the same way. These messages contain updated information from the onboard instruments, like the location of the GRB. After 4–5 minutes a message is sent that indicates that the onboard analysis has ended. The onboard determined position has an accuracy of about 10 arcminutes. Up to a few hours after the burst an offline message can be distributed by a ground based observer that contains the most accurate information. This information is obtained from a detailed analysis of the data that are transmitted by HETE to one of the three primary ground stations, 20–60 minutes after the burst.

The Swift satellite was launched recently (end of 2004), and the HETE mission will most likely finish at the end of 2005. Considering the ANTARES detector construction planning, initially ANTARES will mainly make use of the data from Swift. The sequence of events in the process from the detection of the first gamma rays by Swift to the distribution of the position message will be similar to that

---

[†] Goddard Space Flight Center, Maryland.

of HETE. However, Swift does not immediately send an alert message to ground when its gamma-ray detector triggers. First the onboard instruments calculate the location of the GRB with an accuracy of the order of a few arcminutes. A message is then sent to another NASA satellite system, which transmits the message to a ground station. On ground the message is sent via the Internet to the MOC (Pennsylvania), then to the Swift Science Centre and the central location of the GCN (GSFC). From here the message is distributed over the GCN. The first message after the detection of a GRB thus contains a position, and it is expected to arrive approximately 30 seconds after the detection of the first gamma rays. This message does however not guarantee that the trigger was caused by a GRB. The confirmation that tells if it concerns a real GRB is expected to arrive within an hour after the alert message. At this time the data analysis in ANTARES can start. Afterwards, up to about 16 hours after the burst, many messages can follow with more refined information. Like in the case of HETE, GCN Circulars can be sent with information obtained from offline analysis of the data.

The delay in the arrival of the Swift alert message, which already contains the position, is longer than it is for HETE. This will result in fewer false triggers. On the other hand, the confirmation that it concerns a real GRB and the final location are distributed more quickly. It is expected that Swift will detect at least 100 GRBs per year. Among these, also short GRBs will be detected. These might especially be interesting for ANTARES, assuming that the energy spectrum and burst duration of neutrinos are similar to those of the detected photons.

The sequence of events when a burst is detected by INTEGRAL, and the message types that are then produced, is described in section 1.4.2, as these messages are first distributed by the INTEGRAL Burst Alert Network. The GCN is also used for the distribution of the messages from the Interplanetary Network. How this is done is described in section 1.4.3.

1.4.2 INTEGRAL Burst Alert System

The equivalent of the GCN system for the INTEGRAL satellite is the INTEGRAL Burst Alert System (IBAS) [56]. INTEGRAL was launched at the end of 2002. Its main scientific objectives are the detection, accurate position determination, and identification of point sources. This is done with the spectroscopy and imaging instruments on board. With the gamma-ray detectors on board it is also capable of detecting GRBs. Although the satellite is not primarily meant for GRB detection, in combination with IBAS and the fast distribution of GRB messages, ANTARES can profit from this GRB warning system. It is expected that INTEGRAL will still be operational when a significant part of the ANTARES detector is functioning. The different message types distributed by IBAS are similar to the three GCN Notice message types (alert, update, and position).

Unlike HETE and Swift, INTEGRAL has no onboard triggering system. The operating modes of the instruments do not change when a GRB occurs. All data are continuously transmitted via a ground station to the MOC (Germany). From there they are sent over the network to the INTEGRAL Science Data Center (ISDC, Switzerland). There the data are analysed. For each instrument on board a separate algorithm is applied to the data that searches for GRBs. When one of the algorithms detects a signal an alert message is distributed. This message contains a location with an accuracy of the order of a few arcminutes, but it is not guaranteed that the trigger is due to a GRB. Update messages can follow up to about 3 minutes after the alert message with a more precise location of the GRB. The online analysis and the distribution of the alert and update messages are done automatically. Like in the case of HETE and Swift, offline messages can be distributed by ground based observers. These messages contain the most accurate information and they can confirm or reject the GRB. They can arrive several hours after the GRB trigger time.

IBAS distributes the messages via Internet using the UDP transport protocol. A connection between the ISDC and the site is established when IBAS decides to send a message. All messages that are distributed by IBAS are also sent to the central location of the GCN (GSFC), and from there distributed via the GCN. When the INTEGRAL messages arrive via this way at the site they suffer a small delay.

During its first 2.5 years of operation INTEGRAL localised 23 long GRBs. About half of these GRBs were announced by an alert message, and were later confirmed as a real GRB. For the majority of these bursts the alert message arrived within 20 seconds after the GRB, as shown in figure 1.9. The delays in the arrival of the

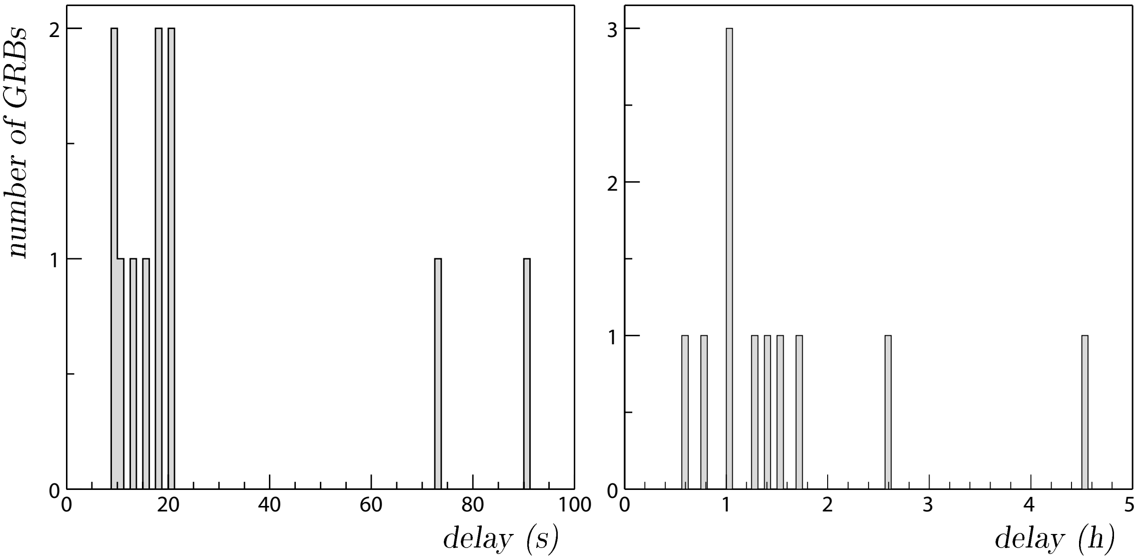

Figure 1.9: *Distribution of the delay between the detection of the GRB by INTEGRAL and the arrival time of the alert message (left) and the confirmation that it was a GRB accompanied by an accurate position (right). The figure includes all GRB announcements that were distributed by IBAS in this way up to 1/1/2005.*

alert message are due to the readout of the satellite instruments, the transmission of the data to ground, the transfer of the data to the ISDC, and the analysis of the data. The time it takes the message to arrive at the site once it is sent is negligible. The alert message contains a location with an accuracy of the order of a few arcminutes. This accuracy is sufficient to start the analysis of the data taken by ANTARES during the GRB. However, a message is needed that confirms the GRB alert before the data are analysed. Most of the messages that contain this information were distributed within 3 hours after the GRB as shown in the figure. This delay is short enough considering the expected analysis time.

1.4.3 Interplanetary network

The Interplanetary network (IPN) is used to determine locations of GRBs [57]. It consists of satellites equipped with gamma-ray detectors. These satellites are widely separated from each other. The difference in arrival times of the gamma rays from GRBs on the different detectors in the network can be tens of seconds or even minutes. The data from the different detectors are compared, and by triangulation the location of the GRB can be determined. This location can be determined with a high accuracy, of the order of arcminutes, because of the large separation of the satellites. The locations of the GRBs calculated by the IPN are distributed via the GCN.

The formation of the network changes when new satellites with gamma-ray detectors are launched, or when old ones fail. At present the gamma-ray detectors on board INTEGRAL and HETE are integrated in the IPN.

The software that calculates the locations uses the data that it receives from the participating satellites, that send their data at least once a day. The time needed to localise a GRB in this way is at least 24 hours. Considering the frequency at which alert messages are distributed and the time needed in ANTARES to process the data taken during a GRB, such a delay in the arrival of the position message is too long. For most of the bursts included in the figures 1.7 and 1.8 the position was determined earlier by the onboard instruments or by offline analysis from ground based observers. The IPN locations are usually distributed a few days after the burst.

Chapter 2

Neutrino detection

Astrophysical objects can be studied by the detection of cosmic neutrinos. Two important features of the neutrino make this particle an obvious candidate to study the astrophysical processes in these sources. Because neutrinos only interact weakly with matter they can traverse regions of matter they meet on their way to the Earth. Secondly, neutrinos carry no electric charge which makes them move in a straight line, regardless of the presence of magnetic fields on their way. The detection of a neutrino and the determination of its direction would directly give information on where it was produced.

Because of their weak interaction with matter, neutrinos are difficult to detect. When they do interact the reaction products can be detected. One way to detect the charged particles among these products is by the detection of the Cherenkov light they emit when moving through water. Because of the small neutrino cross section and the expected low neutrino fluxes from astrophysical sources, a very large detector is needed. By building the detector in the sea, the required target mass is available as well as a suitable detection medium. Such a detector is the ANTARES neutrino telescope, which is under construction.

Since real data from ANTARES are not yet available, much of the work described in this thesis is based on Monte Carlo simulations. For this, software programs are used that simulate the interaction of a neutrino, the propagation of the charged particles, and the production, propagation, and detection of the Cherenkov light. The same method of data taking and data handling is applied to these simulated data, as will be done in the experiment.

2.1 Neutrino interactions

Neutrinos interact with matter only through the weak force. This can happen in a charged current interaction by the exchange of a W^+ boson[†] via the process ν_l+$N \to l^- + X$, or in a neutral current interaction by the exchange of a Z boson via the process ν_l+$N \to \nu_l$+X [58]. At the energies considered here, the dominant cross section is the deep inelastic scattering cross section. The charged current interaction of a neutrino with a nucleon is schematically shown in figure 2.1. In this figure the neutrino ν_l can be any of the three existing neutrino types ν_e, ν_μ, or ν_τ. After the interaction of the neutrino with the nucleon N the associated charged lepton l is produced and the nucleon breaks up in hadrons, in the figure indicated by X. These will also interact with matter and cause a hadronic shower.

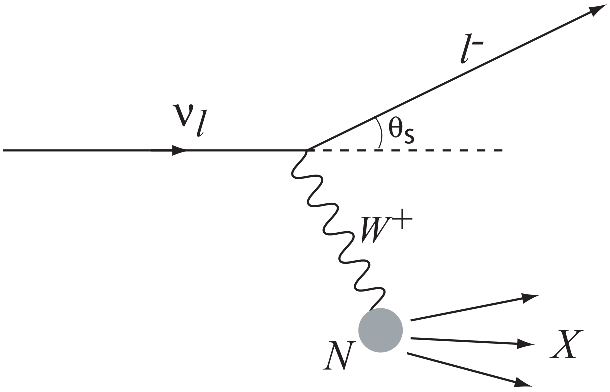

Figure 2.1: *Schematic view of the charged current interaction of a neutrino ν_l with a nucleon N.*

The cross sections of the $\nu_\mu N$ and $\bar{\nu}_\mu N$ interactions are shown in figure 2.2. For low energies the cross section increases linearly with the neutrino energy. At high energies the invariant mass (Q^2) of the (virtual) W boson could be larger than the W rest mass, reducing the increase of the total cross section.

The direction of the produced lepton after the interaction is on average the same as the direction of the incident neutrino. The scattering angle between the directions of the two particles is in figure 2.1 indicated by θ_s. The angular spread depends on the energy. Figure 2.3 shows the angular difference between the incident neutrino direction and the direction of the produced lepton in the case of a $\nu_\mu N$ interaction. On average 1/2 (3/8) of the momentum of the ν_μ ($\bar{\nu}_\mu$) is transferred to the charged lepton. Consequently the angle between the muon and neutrino is small at high energies, typically less than $1.5°/\sqrt{E_\nu[\text{TeV}]}$. This is essential for the neutrino telescope concept.

[†] in the case of an antineutrino a W^- boson is exchanged in the process $\bar{\nu}_l$+$N \to l^+ + X$

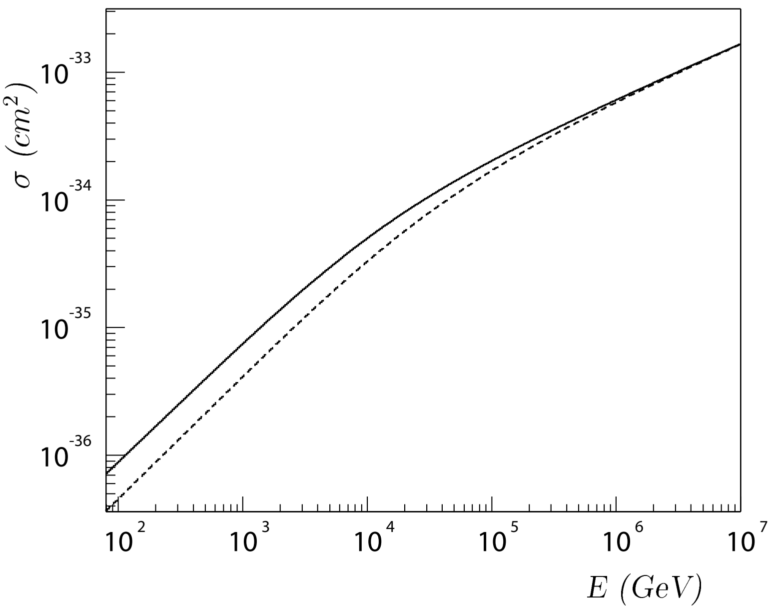

Figure 2.2: *The cross sections of ν_μ (solid line) and $\bar{\nu}_\mu$ (dashed line) interacting with a nucleon as a function of the energy.*

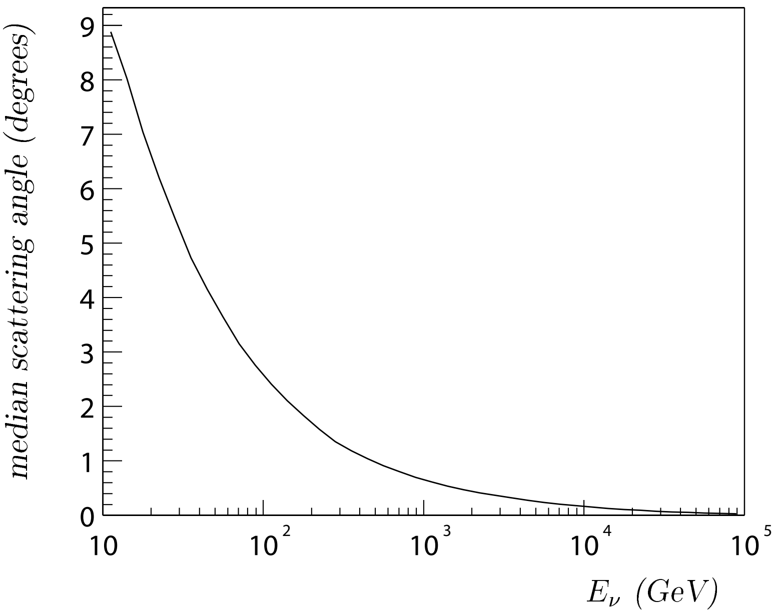

Figure 2.3: *The median angle between the initial ν_μ direction and the muon direction as a function of the neutrino energy.*

2.2 Detection principle

Neutrinos are detected indirectly by the detection of the products created at the interaction vertex. The seawater in and around the detector is used as detection medium for these products [59]. When a relativistic charged particle travels through a medium with a speed greater than the speed of light in that medium it generates a kind of electromagnetic shock wave along its path. This coherent emission of UV and optical photons is known as Cherenkov light [60]. In a neutrino telescope the charged lepton that emerges from the interaction is mainly considered. The light is emitted in a cone with a characteristic angle θ_c given by the relation

$$\cos\theta_c = \frac{1}{\beta n} \tag{2.1}$$

where β is the speed of the charged particle traversing the water (in units of the speed of light) and n is the index of refraction of the water, which is about 1.35. The Cherenkov light cone is visualised schematically in figure 2.4. The wave front has an angle of $(90^\circ - \theta_c)$ with respect to the motion of the charged particle. The Cherenkov angle in (sea)water, in the figure indicated by θ_c, is about 42.5°.

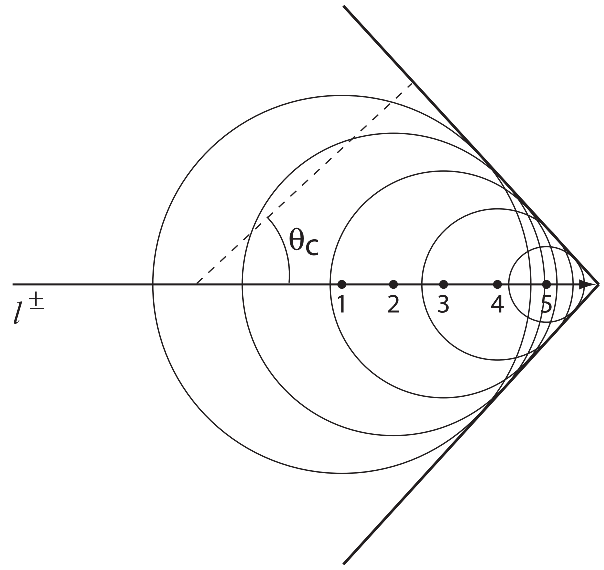

Figure 2.4: *The Cherenkov light cone. Light is emitted isotropically from each point on the track. The order indicated by the numbers corresponds to the direction of the charged particle. The interference of the light produces a coherent wave front indicated by the solid straight lines.*

The produced Cherenkov light can be detected by photomultiplier tubes (PMTs) arranged in the water. The number of emitted Cherenkov photons per unit wavelength λ and unit distance x traveled by the charged particle is

$$\frac{dN}{d\lambda dx} = \frac{2\pi\alpha}{\lambda^2}\left(1 - \frac{1}{n^2\beta^2}\right) \tag{2.2}$$

where α is the fine structure constant. For the sensitive wavelength range of the PMTs (300–600 nm) this corresponds to about 3.5×10^4 photons per meter.

The propagation of the light to the PMTs depends on the properties of the water. The seawater at the ANTARES site can be characterised with an absorption length λ_{abs} of about 60 m and a scattering length of about 260 m. Both are measured at a wavelength of 460 nm [61]. The intensity of the Cherenkov light in water decreases with the photon path length r as

$$I(r) \propto \frac{1}{r}\, e^{-\frac{r}{\lambda_{abs}}} \tag{2.3}$$

The intensity and arrival time of the Cherenkov light eventually detected by the PMTs mainly depends on the absorption length and scattering length respectively. The effect of light dispersion introduces a small spread of about 1–2 ns in the arrival time after a distance of 100 m. The small probability of large angle scattering can introduce a delay in the arrival time of up to a few hundred nanoseconds.

Depending on the neutrino type a certain Cherenkov light signal is produced as shown in figure 2.5. The charged lepton that emerges from a neutrino interaction has a specific signature which is superimposed on the light produced by the nucleon fragmentation at the same interaction.

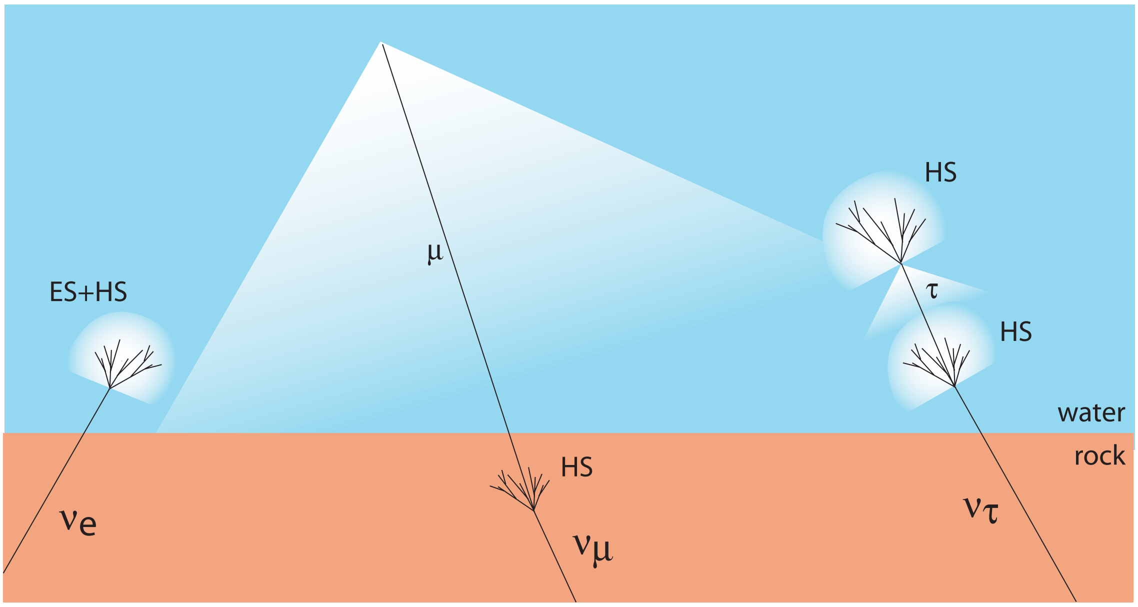

Figure 2.5: *Schematic view of the Cherenkov light signal in water produced by the different particles created by a neutrino interaction. A hadronic shower (HS) occurs at the interaction vertex for each neutrino type. The electron produced after the* ν_e *interaction shows also an electromagnetic shower (ES). The muon from the* ν_μ *and the tau from the* ν_τ *make a straight trace in the detector, meanwhile producing a Cherenkov cone. The tau decays rapidly and produces most likely a second hadronic shower. The muon can travel longer distances.*

2.2.1 Nucleon fragmentation

At the vertex of both a charged current and neutral current neutrino interaction the nucleon can break up into hadrons. Because of the high energies involved, the hadrons will produce Cherenkov light. The produced hadrons travel a certain distance before they interact with the detection medium. In water the hadronic interaction length is about 80 cm. After the interaction new hadrons are formed and the process is repeated. After each interaction their energy drops and eventually they stop producing Cherenkov light. Consequently the total length of this hadronic shower is typically a few interaction lengths. The interaction length increases only slowly with the initial energy. Due to the finite absorption length, the Cherenkov light produced by this hadronic shower will only be detected when the neutrino interaction is near or in the detector. As the distance between the PMTs in the detector is large compared to the size of the hadronic shower, this shower will cause a local signal in a few PMTs.

2.2.2 ν_e interaction

The electron produced after an ν_e interaction loses its energy quickly through the emission of bremsstrahlung photons. These photons will convert to e^+e^- pairs. The distance after which the electron loses all but 1/e of its energy is called the radiation length [62]. In water the radiation length is about 36 cm. The repeated process of bremsstrahlung and conversion will produce an electromagnetic shower. Eventually the energy will drop to a value below which no Cherenkov light is produced anymore. The size of the electromagnetic shower is limited to a relatively short distance and the light it produces shows, like the hadronic shower, a very local signal in the detector. As a result an ν_e interaction can only be detected when the interaction vertex is inside the sensitive volume of the detector.

2.2.3 ν_μ interaction

The muon produced by a ν_μ interaction can travel a large distance in water as it loses energy slowly. Due to its large mass compared to that of an electron, bremsstrahlung is suppressed. The typical energy loss is 0.2 GeV/m. Although the muon loses energy as it propagates through the water it still moves at relativistic speeds and produces Cherenkov light. The muon has a lifetime of about 2 μs. The Lorentz boosted lifetime is much longer than the time it takes to traverse the detector and eventually to stop. A muon with an energy of 100 GeV can travel for about 500 m, and this distance lengthens as its energy increases as shown in figure 2.6. A muon produced by a ν_μ interaction leaves a long straight trace in the detector, and the interaction vertex does not even need to be very close to the detector. Below the so-called critical energy of about 500 GeV the muon range in water increases linearly with its energy. Above this energy the muon behaves like a low-energy electron and radiates bremsstrahlung photons which also produce Cherenkov light (see section 2.2.2). The change in direction θ_0 due to multiple scattering of a relativistic muon on its way to the detector is given by the relation [62]

$$\theta_0 = \frac{13.6\ \mathrm{MeV}}{E_\mu}\sqrt{x/X_0}\,[1 + 0.038\ln(x/X_0)] \tag{2.4}$$

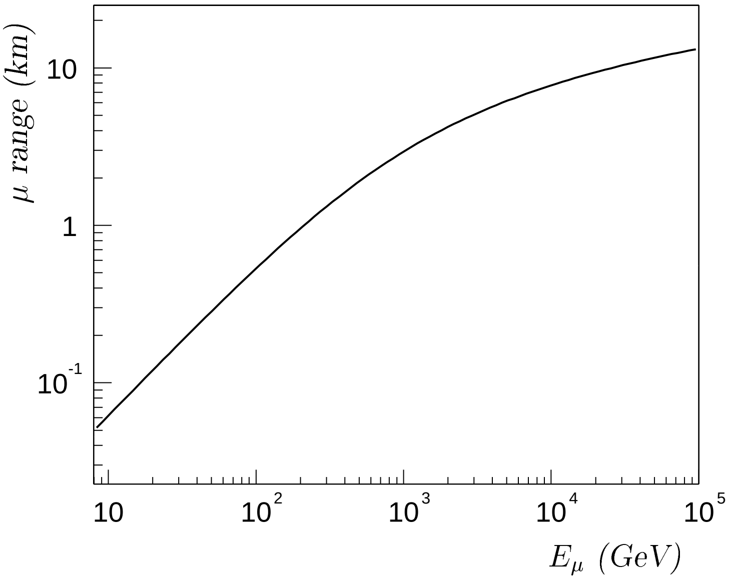

Figure 2.6: *The muon range in seawater as a function of its energy.*

where E_μ is the energy of the muon, x its path length, and X_0 the radiation length of the water. The deviation from the original muon direction is small compared to the median scattering angle shown in figure 2.3 ($\sim 0.1^\circ$ for a muon with an energy of 100 GeV), and will decrease when the energy increases. Therefore the change in direction due to multiple scattering can be safely neglected.

2.2.4 ν_τ interaction

A tau particle has a very short lifetime, about 3×10^{-13} s. Just like the muon, it produces a Cherenkov cone, although the distance it covers in the detector is very short. At very high energies, in the range of PeV, the produced tau particle covers a distance of about 100 m in the detector, which is still short compared to the distance a muon can travel. When the tau particle decays, a muon is produced in about 17% of the cases. The decay muon will cover a large distance in the water as described in section 2.2.3. Otherwise an electron or a charged hadron is produced. At the decay vertex another cascade is formed that also produces light. A detectable signature of a very high energy ν_τ is believed to consist of the signal from the initial hadronic shower at the ν_τ interaction vertex combined with the shower at the tau particle decay vertex separated from each other by a short trace caused by the tau particle [63]. The combination of these signals will be very difficult to recognise, also because of the intense light produced by both the showers, and it will be even worse at lower energies. However, in case the tau decays into a muon, the combination of the described ν_τ signal and the associated muon signal could help with the detection of a ν_τ. In this case the particle identification is not possible by the event topology.

2.3 The muon signal

As explained above, the ν_μ is the most convenient neutrino to be detected. As the produced muon makes a long trace in the detector its direction can be derived most accurately. The light the muon produces can be registered by a three-dimensional array of PMTs that form the detector. As the relative positions of these PMTs are known, and also the time when they detected the Cherenkov photons (with nanosecond precision), the Cherenkov wave front can be reconstructed and thus the direction of the muon. As the direction of the muon is comparable to that of the neutrino, as was shown in figure 2.3, the neutrino direction is found.

The PMTs are arranged in such a way that the separation between them is large to obtain a large detection volume, and small enough to still detect sufficient Cherenkov light from a single muon. The average number of PMTs that detect light from the Cherenkov cone of a passing muon as a function of its energy is given in figure 2.7. All muons are considered for which at least one Cherenkov photon (from either the cone, hadronic shower, or bremsstrahlung) is detected by a PMT. Also indicated are the number of PMTs that detect Cherenkov light from any process induced by the ν_μ interaction, including the hadronic shower and bremsstrahlung photons. Above a muon energy of about 80 GeV, when on average 5 different PMTs detected light from the Cherenkov cone, a muon trace can in principle be deduced from the signal. As the energy increases more Cherenkov photons are detected mainly due to the indirect contribution via bremsstrahlung. The number

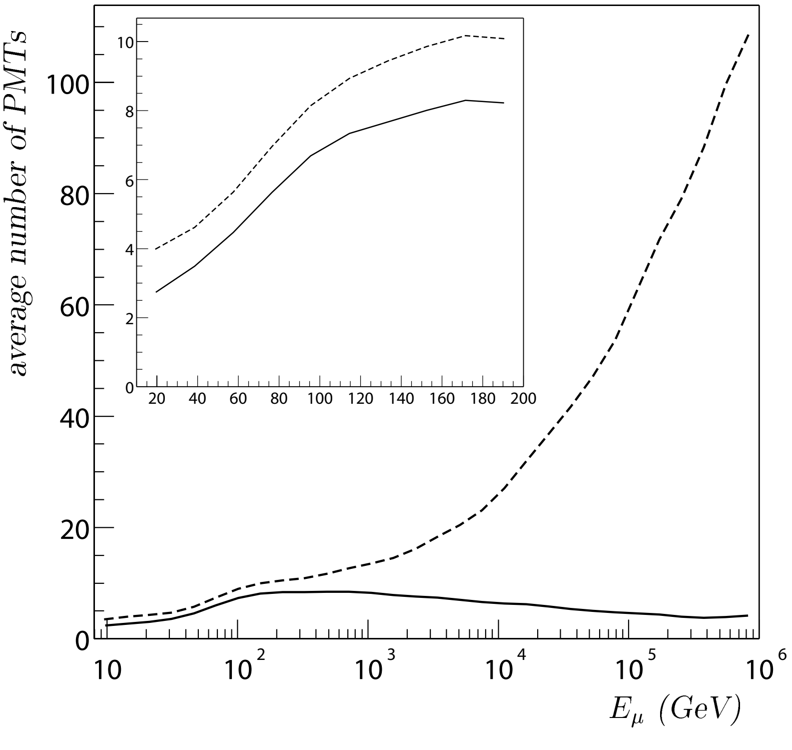

Figure 2.7: *Average number of PMTs that detect light from the Cherenkov cone of a passing muon as a function of the muon energy. Also shown is the average number of PMTs that detect any Cherenkov light produced as a result of the neutrino interaction and the muon (dashed lines). The same is shown in the inset for low energies.*

of Cherenkov photons directly from the muon does not increase because at the same time the effective volume of the detector increases. The muon can be far from the detector, but some Cherenkov photons manage to reach the detector because of the huge contribution of bremsstrahlung.

A muon created by a cosmic ray interaction in the atmosphere above the detector that reaches the detector shows a similar signal as one that is created after a neutrino interaction. In neutrino astronomy muons are only interesting when they originate from ν_μ interactions. When a muon is detected that is moving upward it is certainly produced after a ν_μ interaction, as only the neutrino is able to traverse the Earth. Figure 2.8 shows the three sources of muons that produce the signal in the detector that is searched for. When a cosmic ray interacts with the Earth's atmosphere an air shower is created consisting of different particles, among them muons. When these atmospheric muons are created in the atmosphere above the detector they can reach

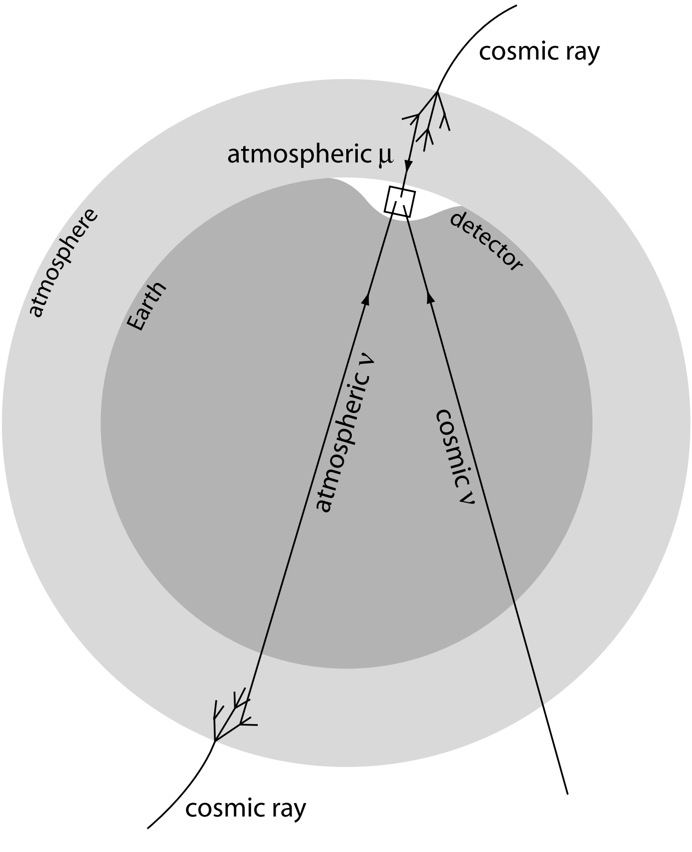

Figure 2.8: *Processes that can cause a muon signal in the detector. Cosmic rays entering the Earth's atmosphere produce atmospheric muons and atmospheric neutrinos. The atmospheric muons created above the detector will be detected when they reach the detector. Atmospheric ν_μs will be detected when they interact near the detector and produce a muon. Only upgoing muons are considered as these originate from a neutrino.*

its sensitive volume and produce a detectable signal. In the same way, by cosmic ray particles entering the atmosphere, neutrinos will be created. These atmospheric neutrinos can interact near the detector. When this happens for an atmospheric ν_μ that is produced on the other side of the Earth, a muon is produced that moves upward in the detector. It produces a similar signal in the detector as a muon from a neutrino produced by a GRB. The two different origins of the neutrinos cannot directly be distinguished. This is further discussed in the chapters 5 and 6.

2.4 Event rate

The number of detected neutrinos per unit time as a function of the energy can be expressed as

$$dN(E) = \Phi(E) \times \sigma(E) \times N_A \times \rho \times V_{\text{eff}}(E) \times dE \tag{2.5}$$

where $\Phi(E)$ is the incident ν_μ flux, $\sigma(E)$ the charged current cross section, N_A the Avogadro constant, ρ the density of the medium, and V_{eff}(E) the effective volume. The density of the medium for ANTARES is taken as 1.024 g/cm^3. In this equation the dependence of the cross section and the effective volume on the kinematics of the interaction is implicitly integrated. The effective volume is defined as the volume in which a neutrino interaction produces a detectable muon, and basically indicates the size of the detector. The number of detected neutrinos per unit time can also be written as

$$dN(E) = \Phi(E) \times A_\nu^{\text{eff}}(E) \times dE \tag{2.6}$$

where $A_\nu^{\text{eff}}(E)$ is the neutrino effective area. It indicates the sensitivity of the detector to a neutrino flux. Both the effective volume and effective area will be used to express the performance of the detector.

2.5 Detector description

The ANTARES detector will be built in the Mediterranean Sea at a depth of 2.4 km at the location 42°50′ N, 6°10′ E. The geometry of the detector is displayed in figure 2.9. The PMTs are divided over 12 vertical strings to obtain a three-dimensional array of PMTs. The bottom of each string is anchored on the seabed and held upright by a buoy at the top. A string has a total length of about 500 m. The strings are separated from each other by a distance of typically 60 m. The PMTs are grouped in triplets. Each string holds 25 triplets, called storeys, and the complete detector will contain 900 PMTs. The storeys are separated from each other by a distance of 14.5 m. The storey closest to the seabed is placed at a height of 100 m to allow the Cherenkov cone to develop. The instrumented volume of the detector is roughly 0.02 km^3.

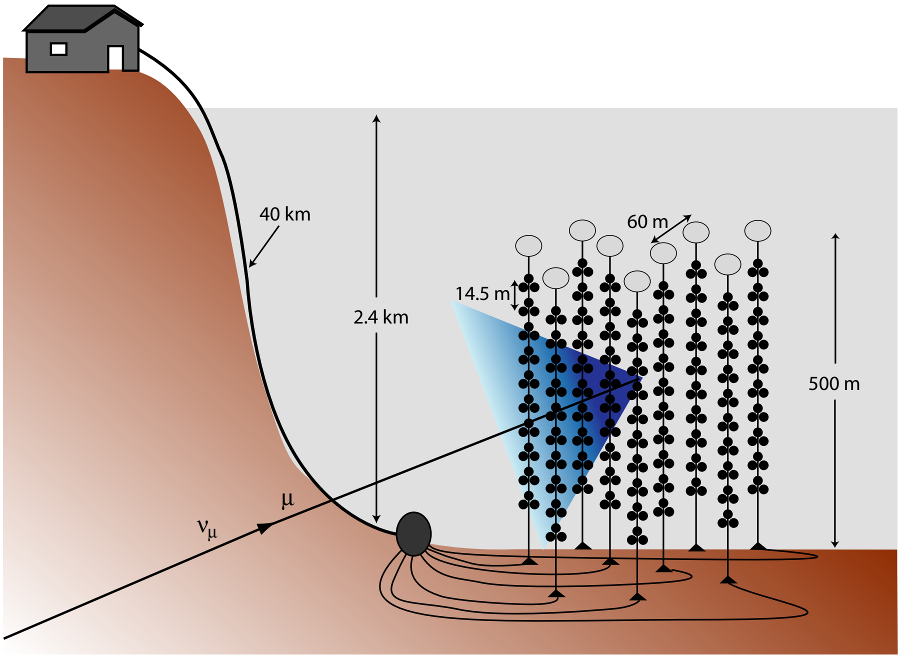

Figure 2.9: *Schematic view of the ANTARES detector.*

The PMT type used in ANTARES is the 10 inch Hamamatsu R7081-20 [64]. It is sensitive to single photons and its sensitive area corresponds to about 500 cm^2. The timing resolution, essential for the determination of the direction of a muon, is expressed in terms of the transit time spread (TTS) of the PMT. The TTS of this PMT is about 2.6 ns (FWHM). The PMT is sensitive in the wavelength range between 300 and 600 nm. Its quantum efficiency is maximal in the wavelength range from 350 to 450 nm, and amounts to about 25%. Each PMT is accompanied by electronics that provide the required high voltage. The PMT and its associated electronics are housed in pressure resistant glass spheres, called optical modules (OM). Three OMs are attached to a titanium frame as shown in figure 2.10. This frame also holds a titanium cylinder containing readout electronics which is called a Local Control Module (LCM). The readout system in the LCM consists of several custom designed Analogue Ring Sampler (ARS) chips [65] (two for each OM), a Field Programmable Gate Array (FPGA), and a processor. The ARS chip digitises the analogue signals of the PMTs, the FPGA buffers these data, and the processor sends the buffered data to shore. The data taking and data handling is described in detail in section 4.1. Each string has at the bottom an extra titanium cylinder, called the String Control Module (SCM), containing electronics for the slow control and position calibration instruments (see section 2.6).

The detector will in principle be taking data 24 hours a day, every day. The data transmission from the LCMs to shore is done with fibre optics. Each string is connected with a cable to the junction box which is connected to the shore with a

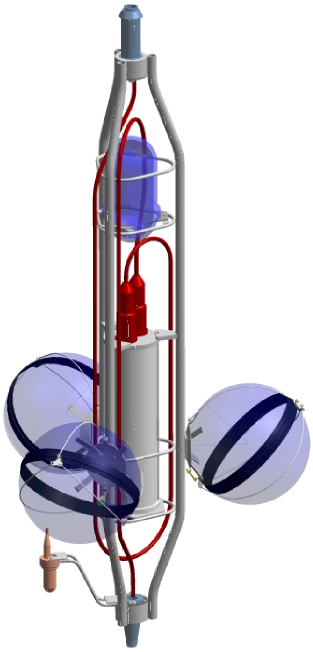

Figure 2.10: *Three optical modules are attached to a titanium frame. The optical modules are pointed downward with an inclination of* 45° *with respect to the horizon. The frame also holds a titanium cylinder housing electronics which handle the readout of the three optical modules.*

single 40 km long main electro-optical cable (MEOC). The MEOC is used for all data transport between the shore and the detector. The junction box also distributes the electrical power to each line. On shore a link with optical fibres connects the MEOC to the shore station where the detector is operated, and the data are saved to disk. The data acquisition system and operation of the detector is described in detail in chapter 3.

2.6 Detector position calibration

The relative positions of the PMTs need to be known with an accuracy of 10–20 cm to be able to accurately determine the path of a muon traversing the detector from the Cherenkov light it emits. This is compatible with the time resolution imposed by light scattering and dispersion. The bottom of the strings will be attached to the seabed, but as a result of the water flow the shape and orientation of the strings will change with time. The positions of the PMTs need to be determined regularly during operation of the detector. This is done by an acoustic position calibration system which consists of an acoustic emitter in the SCM at the bottom of each string, and five hydrophones per string, distributed in such a way that one hydrophone is placed on each fifth storey of a string. The emission of an acoustic signal is regulated from shore and generates a 40–60 kHz acoustic pulse. The travel time of this pulse is measured between the emitters and receivers. The three-dimensional position of each hydrophone is obtained by triangulation of the travel times using the measured sound velocity. The hydrophones are connected to the LCM of the frame they are attached to. The data they collect are handled by electronics in the LCM and sent to shore in the same way as the PMT data. On shore the data are stored in a database. The shape of a string can more accurately be determined by also measuring the orientation of each LCM. For this, a tiltmeter-compass sensor is placed in the LCM of every second storey, which measures (during the acoustic position calibration cycle) the tilt angle of the LCM with respect to the horizon, and the orientation around the vertical axis. The combined results from this method and the acoustic position calibration method are used to reconstruct the shape of each string. The expected accuracy on the positions of the PMTs obtained with this method is 5–10 cm. This cycle is done repeatedly during data taking to account for the water flow, and takes about 10 s for the complete detector.

The orientation of the detector with respect to the stars is needed to tell, once a neutrino is detected, where it came from. In the case of detection of neutrinos from GRBs as it is done in ANTARES this knowledge is even needed beforehand, as the absolute position of the GRB will be used in the analysis methods. The three geographic position coordinates (longitude, latitude, and depth) are measured during the string deployments using GPS measurements of the ship, pressure sensors, and the length of the deployment cable. The obtained position has an accuracy of a few meters. The absolute orientation of the detector needs to be determined with an accuracy of 0.1°. For measuring the three orientation angles a method is used similar to the relative acoustic position calibration system. Four transponders are placed on the seabed around the detector, on the north, south, west, and east side, a few hundreds of meters apart from each other. The depth of these transponders is known from the pressure sensors. By applying the acoustic triangulation method to those four transponders with known depths, the tilt of the detector with respect to the horizontal plane in north-south direction and east-west direction can be determined. The third orientation angle is determined with two extra transponders and a surface ship with GPS equipment. The two extra acoustic beacons are placed a few kilometers away from the detector. With the GPS system and acoustic signaling the absolute positions of the two beacons can be measured. By using also the four other transponders around the detector in the acoustic system the rotation of the detector around the zenith can be determined.

2.7 Physics simulation

To examine the physics signal in the detector caused by a neutrino interaction a set of software tools is used to simulate the underlying processes. The simulation packages used in ANTARES are described in detail in [66]. With these tools a neutrino interaction can be simulated in the energy range from 10 to 10^7 GeV, including the production and propagation of the resulting charged particles, and the production and propagation of the Cherenkov light they emit.

The interaction vertices of neutrinos are generated in a large volume centered around the detector. The size of this volume depends on the upper limit of the considered energy range. It is such that the particle with the highest energy that is produced anywhere in this volume can approach the detector to a distance where the light it emits can still be detected. For an upper limit of 10^7 GeV the generation volume is about 2×10^4 km^3. Considering the energy of the neutrinos studied in this work only the deep inelastic scattering (DIS) cross section is taken into account. DIS interactions are generated using the LEPTO package [67]. It calculates the cross section values shown in figure 2.2, and the kinematics of the produced particles. The hadronisation of the nucleon fragmentation is done using PYTHIA 5.7 and JETSET 7.4 [68]. For the parametrisations of the quark distributions the CTEQ3D Parton Distribution Functions [69] are used. The rock below the detector is also taken as a possible interaction medium. The difference in the total cross section compared to that of water is taken into account and amounts to about 4%.

The probability of transmission of a neutrino through the Earth depends on the column density of the Earth [70] and the neutrino energy. In figure 2.11 this probability is shown as a function of the neutrino energy for different neutrino directions. The amount of matter the neutrino traverses when propagating through the Earth

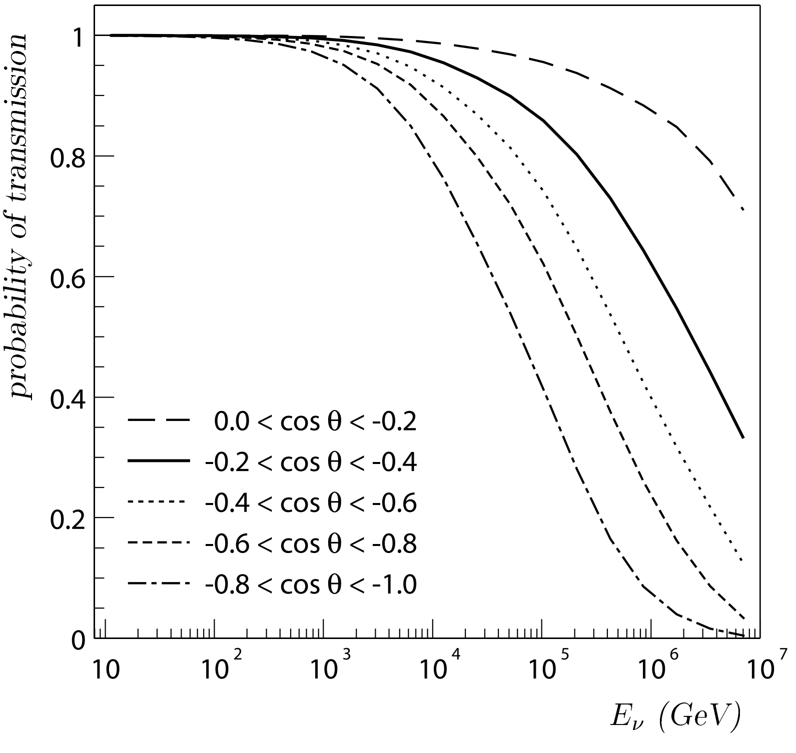

Figure 2.11: *The probability of transmission of a ν_μ through the Earth as a function of its energy and the zenith angle $\cos\theta$ of its direction ($\cos\theta = -1$ corresponds to vertically upwards).*

depends on the zenith angle of its direction. Due to the rotational symmetry, the dependence on the azimuthal angle has been neglected. When the direction of the neutrino is vertically upwards (the column density is maximal when the cosine of its zenith angle equals -1), it is more likely that it will interact in the Earth before it reaches the generation volume. This effect is enhanced when the neutrino energy increases. The probability of transmission is taken into account in the simulation.

The propagation of the muon from the vertex until it arrives at a detectable distance from the PMTs is also simulated. For this the MUM package [71] is used. The muon loses energy on its way to the detector. At low energies (less than about 500 GeV) the energy loss is dominated by ionisation of atoms in the medium by the passing muon. In this process a small fraction of the energy of the muon is transferred to the electrons in the atoms. The energy loss due to this process is about 0.2 GeV/m. At higher energies the energy loss is mainly due to two different processes. In the vicinity of an atomic nucleus the muon can emit a photon that directly forms an e^+e^- pair with a photon radiated by the nucleus. This process is known as pair production. The other process, bremsstrahlung, has been mentioned in section 2.2.3. The effect of the additional energy losses of a muon becomes apparent by the nonlinearity of its range as shown in figure 2.6. These and other minor energy loss processes are all simulated by the MUM package for both the media rock and water. The change in the direction of the muon path by multiple scattering on atomic nuclei is not simulated, nor is the deflection of the muon as a result of the above mentioned processes. These effects are negligible. Therefore, the direction of the muon in the detector is presumed to be the same as that at the interaction vertex.

For the simulation of the production and propagation of the Cherenkov light a second but smaller volume is defined around the instrumented volume. The instrumented volume is extended with a few absorption lengths beyond the outer PMTs. This volume is known as the “can”, and its size is about 0.1 km^3 (about five times the instrumented volume). When the produced particles reach the can, the Cherenkov light they emit could reach the PMTs. The light production and propagation is only simulated for the particles that reach the can. This simulation is generally done with the KM3 package [72] where the properties of the seawater and the features of Cherenkov light mentioned in section 2.2 are used. The scattering of the Cherenkov photons on particles in the water and the dispersion of the light are also simulated. For the velocity of the light the group velocity of light in water is taken [60, 73]. The propagation of particles through the can, other than the muon, is done with a custom made tool based on GEANT3 [74]. This is important when the interaction vertex is in or near the instrumented volume. The propagation of the muon through the can is done in KM3 using a modified version of MUSIC [75].

2.8 Detector simulation

The response of the detector to the Cherenkov light depends on the properties of the PMTs described in section 2.5. In the simulation of the detection of the light the quantum efficiency of the PMTs, the effective area of the photocathode, the transit time spread (taken as 1.3 ns), and the optical properties of the different materials used in the OM are included. Also taken into account is the dependence of the efficiency of the light detection on the angle of incidence of the photon on the OM. The gain spread and charge determination are also simulated. The typical overall amplitude resolution is found to be 40% [64]. The distribution of arrival times of photons from a muon on a PMT is shown in figure 2.12. The contribution from the Cherenkov wave front can be seen clearly at zero time residuals. A significant tail to later arrival times is also visible. Especially scattered photons and photons not directly from the muon show large (positive) time residuals. The number of detected photons directly from the muon is in general small as was already concluded from figure 2.7.

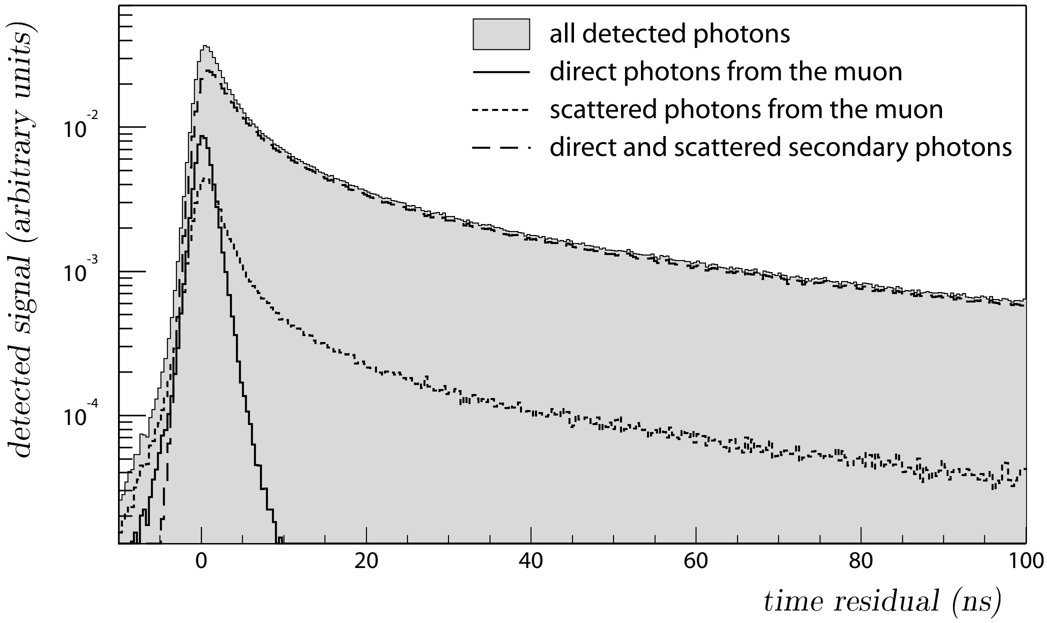

Figure 2.12: *Distributions of arrival times with respect to the expected arrival time of direct Cherenkov photons. Indicated are photons directly from the muon, photons directly from the muon that scattered, and photons from secondary processes, direct and scattered. Especially scattered secondary photons can have large time residuals. Only the photons are included that were detected by PMTs and that are within a distance of 180 m from the muon.*

The effect of the electronics that digitise the data and send it to shore is also simulated. The signals detected by the PMTs are digitised by the ARS chips in the LCM. Each PMT is connected to two ARS chips. An ARS integrates the PMT signal over a period of typically 30 ns. Two or more photons that are detected within this time are combined. After a signal is detected, the ARS has a dead-time of 250 ns. The second ARS takes over after the integration time. This simulation is done before the data are filtered. The filtering of the data is described in chapter 4.

2.9 Background

As described in section 2.3, atmospheric muons and atmospheric neutrinos can cause a muon signal in the detector that should be rejected. The simulation of energetic air showers that produce atmospheric muons is done with the CORSIKA package [76] which uses the QGSJET model [77] for the simulation of the high-energy hadronic interactions. Many muons can be produced in a single air shower. These muons are first extrapolated to the surface of the sea. From there, their propagation through the seawater to the detector is simulated with MUSIC [75]. This simulation was done for five different primary particles (H, He, N, Mg, and Fe) that produce most of the atmospheric muons. Their fluxes are taken from [78]. Although the number of atmospheric muons produced in this way that reach the detector decreases exponentially with the depth of the detector [79], still many atmospheric muons produce a signal in the detector. The atmospheric muon flux at a depth of the ANTARES detector is shown in figure 2.13.

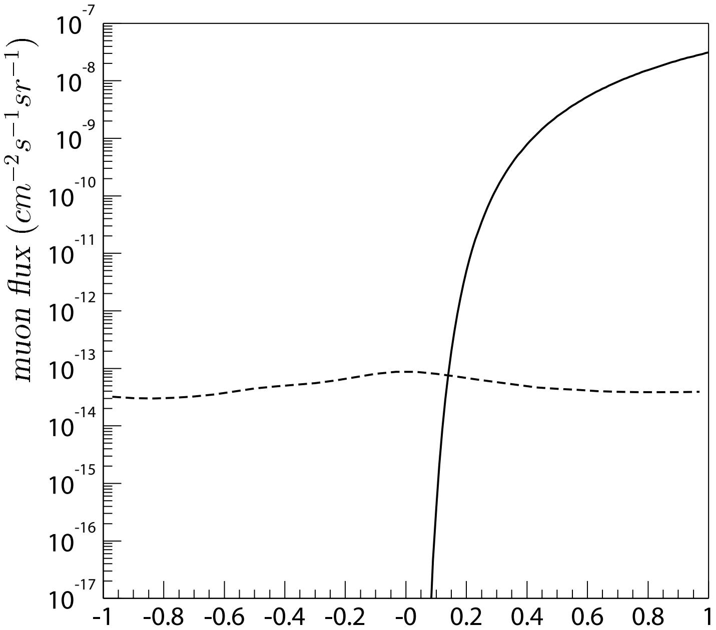

Figure 2.13: *The muon flux in water at a depth of 2.1 km as a function of the zenith angle. The muon flux due to atmospheric muons is shown (solid line) as well as the muon flux induced by atmospheric neutrinos (dashed line). Only muons with an energy higher than 100 GeV are included.*

Atmospheric neutrinos, and the signal their resulting muons produce in the detector, are simulated the same way as described in sections 2.7 and 2.8. For the fluxes of these neutrinos two different models are used, depending on the energy. For neutrino energies below 10^5 GeV the flux is dominated by the neutrinos produced by pion and kaon decay, above that energy by the decay of charmed mesons. The fluxes used are given in [80] and [81] respectively. The muon signal in the detector caused by atmospheric neutrinos produced above the detector is largely exceeded by the atmospheric muon flux as shown in figure 2.13. In the search for neutrinos from GRBs only upward moving muons will be considered. The rejection of atmospheric muons and muons from atmospheric neutrinos will be described in the chapters 5 and 6.

Apart from background from atmospheric muons and atmospheric neutrinos the detector is also subjected to random background and bioluminescence. The random background is due to radioactive decay of elements, mainly ^{40}K, in the seawater. The light produced by this process results in a singles rate of about 27 kHz on each PMT [82]. There is also a contribution of about 2 kHz from the dark current in the PMTs which passes the ARS threshold. The amount of light caused by bioluminescence depends on different aspects like the time of year and the water flow. Unlike the radioactive decay it is not constant, but it shows strong fluctuations in time. Measurements done with a prototype detector show that the baseline rate from random background can change between 50 and 300 kHz within a period of three months, and that the contribution from bioluminescence shows peaks of sometimes several MHz during short periods (a few seconds at most) [83]. For the combined signal from bioluminescence and radioactive decay a constant singles rate of 70 kHz is assumed in this work. This corresponds to the average rate from the measurements done at the detector site. This background is included in the simulations by generating random signals at this rate with a charge corresponding to a single photon, and taking into account the characteristics of the PMTs and ARSs. The peaks from bioluminescence are not simulated. The rejection of the random background is described in the chapters 4 and 5.

Chapter 3

The data acquisition system

The preparation of the detector for data taking, the data transport from the Local Control Modules (LCMs) to shore, the data processing, the data storage on disk, and the switching on and off of the detector is done by the Data AcQuisition (DAQ) system. The DAQ system of ANTARES has some characteristic features, differentiating the detector from other similar neutrino experiments, like AMANDA [7] and Baikal [8]. These features are mainly a consequence of the all-data-to-shore concept, and include the very short dead-time, and the possibility to buffer raw data.

In the all-data-to-shore concept, all raw data are sent to shore and processed there. In contrast to what is done in the AMANDA and Baikal detectors, the off-shore front-end electronics in ANTARES do not filter the data. Instead, every detected photon signal is digitised inside the LCM. The analogue ring sampler (ARS) chips operate in pairs to compensate for the dead-time after the integration of the analogue signal from the photomultiplier tube (PMT) (see section 2.8). Only when the second ARS is mobilised for the digitisation of subsequent detected photons, the dead-time of 250 ns plays a role. This is very short compared to the expected singles rate of 70 kHz. All digital signals are transported to shore where they are processed. Apart from the dead-time in the data taking, a very small data loss is introduced by the data processing (see section 4.1). The combination of the all-data-to-shore concept and the number of data processing PCs in the shore station enable the DAQ system to buffer all raw data that were taken during a few minutes before they are processed. As explained in chapter 4, these features are important for the detection of neutrinos from GRBs. The techniques used in the DAQ system make the detector specifically suitable for this goal compared to the other experiments that also have the aim, among other things, to detect neutrinos from GRBs.

The DAQ system is operated with the RunControl program. Apart from preparing the system for data taking, it also takes care of the bookkeeping of the detector settings and the data taking history by using a relational database.

3.1 Overview

A schematic overview of the main hardware components and software processes in the DAQ system is shown in figure 3.1. Part of the DAQ system is situated off-shore, and consists of 300 LCMs and 12 String Control Modules (SCMs). The main components of an LCM are 6 ARS chips (2 for each PMT), a local clock, and a processor. During data taking the analogue signals from the PMTs are digitised by the ARS chips. For the arrival time of a detected photon the local clock of the LCM is used. All LCM clocks are synchronised to the on-shore master clock which provides the GPS time. The SCM is mainly used for the slow control of the electrical power system of the string and the position calibration system. It also has a processor. Each LCM and SCM processor has an Ethernet port for the connection to shore, and can be considered as a node in the DAQ network, having its own IP address. These processors run two software programs: DaqHarness and ScHarness. The **DaqHarness** process handles all data that were produced by the

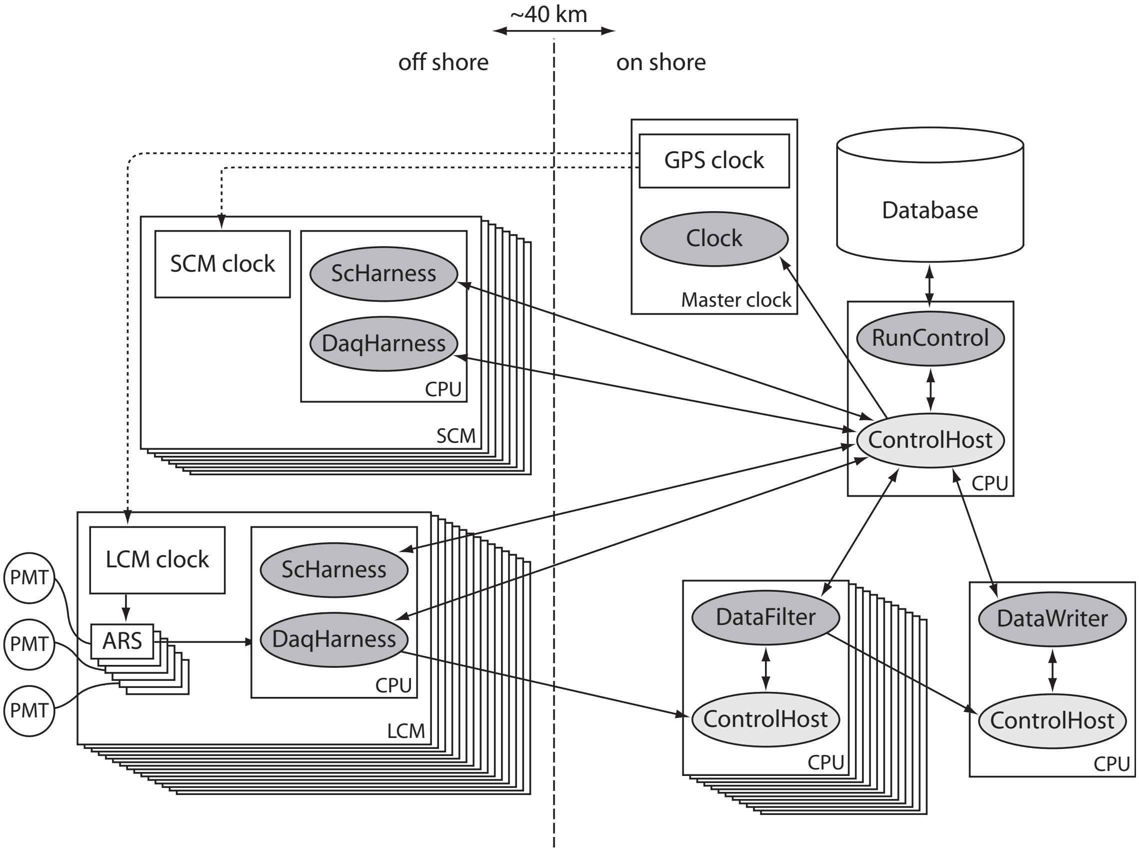

Figure 3.1: *Schematic overview of the main hardware and software components in the DAQ system. The rectangles represent hardware devices, and the ellipses software programs. The lines between the objects symbolise the data and message traffic.*

ARS chips in that LCM. All data that were produced during a time frame of 13 ms by the ARS chips in one LCM are buffered in a so-called frame. The DaqHarness sends each frame as a single packet to shore using the Internet protocol. The **ScHarness** process controls the high voltage applied to the PMTs. It is also used for the readout of various instruments. This information is also sent to shore (in a different format than the ARS data frames) and is used to monitor the detector and its environment.

The on-shore part of the DAQ system consists of a farm of standard PCs, the database, and the clock system, situated in the shore station. Most of these PCs are devoted to the processing and storage of the data. One of the PCs runs the **RunControl** program which is used to operate the detector. The database system consists of several large disks and a PC that runs the interface to the database. Both the RunControl and the database are discussed later in this chapter.

Communication between processes is done with the **ControlHost** package [84]. ControlHost handles all the communication using TCP sockets. It implements the tagged data concept, which means that any program in the system can send data accompanied by a tag to a server. The server will distribute the data to all processes that subscribed to the specific tag. There is a central ControlHost server used for the communication between the RunControl and all other processes in the system. The implementation of ControlHost enables the exchange of information between processes written in different programming languages (C, C^{++}, and Java are the languages used in the DAQ system).

Processing of the data is done with the **DataFilter** program that runs on each of the data processing PCs. The frames from all DaqHarness processes that contain the data that were taken during the same 13 ms, are sent to one specific PC that runs the ControlHost and DataFilter programs. This PC is identified by its IP address. The list of IP addresses as possible destinations for the raw data will be provided to the DaqHarness processes by the RunControl program. The DataFilter program merges all the frames into a so-called TimeSlice. It then filters the physics signal from the background. In this way, the data output of the detector is reduced such that it can be written to disk for offline data analysis. Each data sample that could be considered as a signal produced by a muon traversing the detector is called an event. Events are passed via ControlHost to the **DataWriter** program which formats the events and writes them to disk. The data taken during one run are stored in a separate file. The way the data are processed is described in more detail in section 4.1.

The data that are eventually stored on disk are copied regularly from the shore station to a computer centre elsewhere. These are the events that are used for the offline data analyses. All data output that is stored on disk is written in ROOT format [85].

Each processor in the DAQ system uses Ethernet for the communication, and has a 100 Mb/s or 1 Gb/s Ethernet link. The links of every five consecutive LCMs (100 Mb/s) on one detector string, called a sector, are merged off-shore into a single Ethernet link (1 Gb/s) to shore. These links are connected to a large Ethernet switch in the shore station. The large bandwidths are needed to handle the high data output rate of the detector, which is, on average, expected to be about 0.4 GB/s (see for data rates chapter 4). The DataFilter processors on shore are connected to the same Ethernet switch. All other processors that contribute in the DAQ system are also connected to the same Ethernet switch. Together they form an Ethernet network. This makes the distribution of the data from the LCMs to the on-shore processes transparent, and it enables the RunControl to communicate with all processes in the system.

3.2 State machine

Preparing the DAQ system for taking data involves a number of steps. For example, the high voltage has to be applied to the PMTs gradually, the ARS chips have to be configured depending on the type of data that will be taken, and also the data processing programs have to be configured. Stopping the data taking (and switching off the detector) is done again in several steps. The high voltage on the PMTs has to be lowered gradually, the data that are still being processed have to be handled, the data files have to be closed, and the run information has to be stored in the database. The actions that have to be taken before the data taking can start and after the data taking has stopped have to be done in a specific order. For this a finite state machine is designed with a predefined set of states. Each of the processes that participates in the DAQ system, except for the data transfer package ControlHost, has this state machine implemented. The CHSM [86] language system is used for the implementation of the finite state machine. The finite state machine implemented in the DAQ system can be represented by the state diagram shown in figure 3.2. It consists of a fixed number of states and transitions. A state reflects the condition of the finite state machine. It is associated with the changes that took place in the system so that it came from the start state to the present situation. Each state has one or more transitions to other states. A transition indicates a state change and is

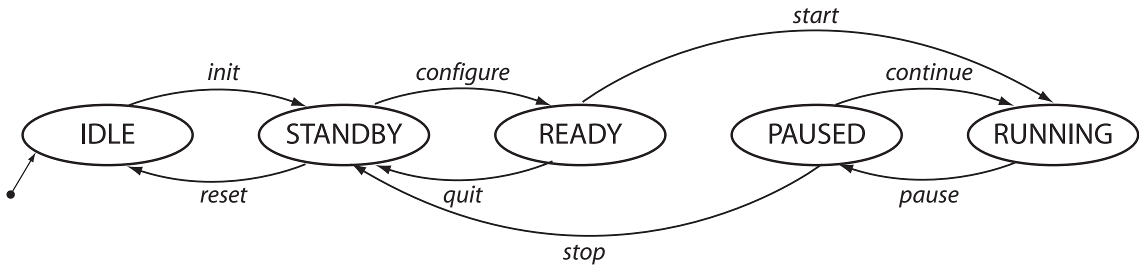

Figure 3.2: *The state machine of the DAQ system. The ellipses indicate the different states in the state machine, and the arrows the state transitions. When the state machine is entered it starts in the* IDLE *state, indicated by the symbol* •⟶.

accompanied by a condition that has to be fulfilled to enable the transition. There are also actions in the system that have to be performed at certain moments. This can be when a state is entered or exited, or when a state transition is performed. The various states and transitions are described in more detail in section 3.3.3.

3.3 RunControl

The RunControl program is the main interface of the DAQ system. It starts the processes participating in the DAQ system, controls the state transitions, and prepares the DAQ system for data taking. It keeps track of the status of all processes in the system at all times. When the data taking is started and stopped, it updates the database with the necessary information about the run and the detector settings. As the state transitions are initiated by the RunControl, the RunControl can be considered as the master in the system, and all other processes in the DAQ system as its clients. Depending on which processes should participate in the DAQ system, and the type of data that should be taken, the DAQ system has to be configured in a certain way. This, and the generation of the state transitions, is done by the operator via the graphical user interface of the RunControl.

3.3.1 The RunControl interface

Apart from controlling the state machine of the DAQ system, the RunControl also has a monitoring task. The graphical user interface of the RunControl, shown in figure 3.3, displays all relevant information, namely the list of the participating clients in the system, the status of each client, the chosen settings and configuration, the run information during data taking, and the overall state of the DAQ system. The RunControl is described in detail in [87]. Here only the mechanism of the communication between the RunControl and the clients is described, as well as the exchange of information between the RunControl and the database.

Each coloured square box in the interface panel represents a client process. The different rows of processes indicate the different types of client processes that were described in section 3.1: DaqHarness, ScHarness, DataFilter, or DataWriter. The client setup of the system is associated with the different types of client processes involved in the system, and the number of client processes of each type. From the client setup shown in the figure it is clear that this was used for the operation of the so-called prototype sector line [88]. This prototype detector was operational during a few months in 2003 and consisted of a part of one detector line, made up of one sector (5 LCMs and 1 SCM), for which 6 DaqHarness and 6 ScHarness processes are used as shown by the client setup panel in the figure. For the operation of the full detector there will be 312 DaqHarness processes, 312 ScHarness processes, and tens of DataFilter processes. The same interface will be used to monitor all these client processes. With the buttons (bottom right in the figure), of which the labels of most

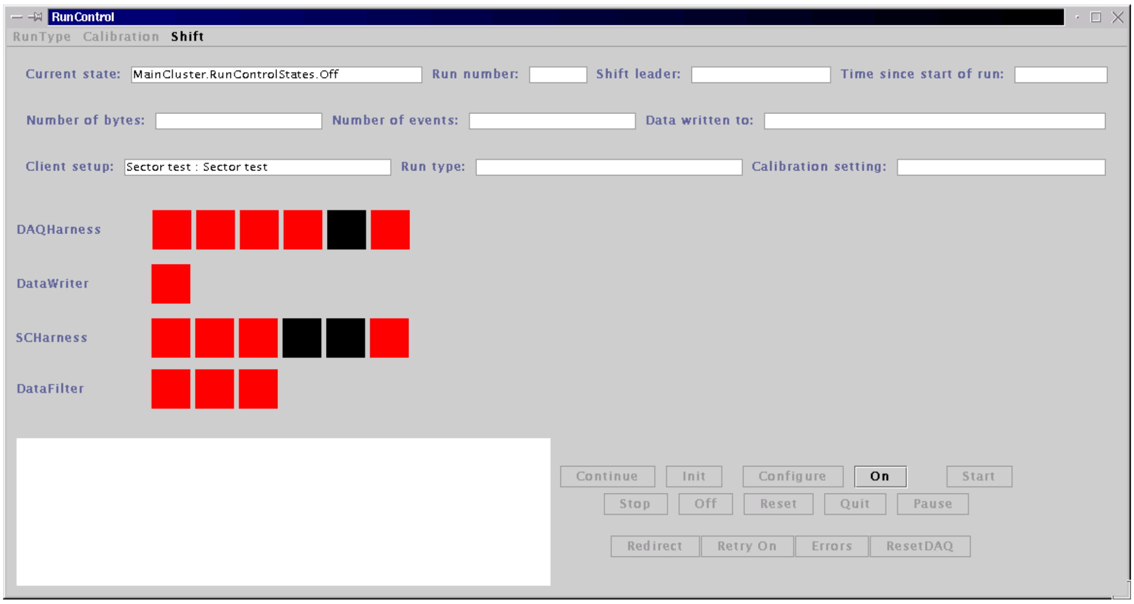

Current state: MainCluster.RunControlStates.Off

Client setup: Sector test : Sector test

Figure 3.3: *The RunControl interface as it was used during operation of the prototype sector line.*

of them correspond to the state transitions given in the state machine diagrams, the state transitions can be initiated.

3.3.2 Database

For the database in the DAQ system Oracle is used, which is a relational database system [89]. In a relational database the data are stored in tables. Each table contains one or more data categories organised in columns. Each row in the table contains an instance of the data for the categories defined by the columns. The tables are related to each other by means of a common key.

There is one central database system in ANTARES that is also used by the DAQ system. The relevant data for the DAQ system that are stored in the database are the detector construction information (the location of each component in the detector), the client setup types, the different configuration types for each client setup, the initialisation and configuration data, and the information about the data taking. All data the DAQ system needs to operate are recovered from the database by the RunControl. It does this by using the relations between the database tables starting from the setup selected by the operator.

All possible client setup configurations, all different detector configurations for each client setup, and all configuration and initialisation data needed to operate the detector are stored in the database beforehand. The RunControl will at startup connect to the database and list the possible client setup types. From this list, a client setup has to be selected interactively. The RunControl can then find in the database the involved processes, which will be visualised in the interface panel. At the same time it retrieves the possible configuration types for the specific client setup, for which a list is accessible from the interface. This is the situation shown in figure 3.3. The prototype sector line has been operated in this way. Client setup types can be extended just by adding another entry to the corresponding database table with a reference to the desired client setup type. This will happen during the construction of the detector, where the strings are deployed one by one. In the end, the client setup for the complete detector will consist of hundreds of processes.

From the information stored in the database, and the selection of the operator, the RunControl will set up the interface. Client setup types consisting of different numbers of clients can be created for operating parts of the detector. LCMs, sectors, or strings can in this way be left out from the operation if necessary. Depending on the type of data that have to be taken, the configuration type is also chosen interactively. Using the constraints on the client setup and the configuration setup, the RunControl will retrieve the corresponding initialisation and configuration data from the database and pass them to the clients that require these data for their state transitions.

In two cases, when the data taking is started and stopped, the RunControl updates a certain table in the database. During these state transitions the run information and the reference to the detector settings are stored to be able to couple the detector settings to the data when they are eventually analysed.

3.3.3 The RunControl state machine

The state machine that is implemented in the RunControl is more extensive than the general state machine implemented in all clients that participate in the DAQ system (see figure 3.2). The state machine implemented in the RunControl consists of two clusters, shown in the state diagram in figure 3.4. The states in the RunControlStates cluster correspond to the different stages in the process from entering the state machine to taking data. The transitions between the states from the OFF state to the RUNNING state accomplish the steps involved in preparing the system for data taking. When the system is in the RUNNING state, it is taking data. The transitions that lead back to eventually the OFF state take care of the steps required to stop the data taking and switch off the detector. When the data taking is stopped, the PAUSED state is entered first to allow some time for the data processing programs to handle the data they have in memory and finish processing. The *continue* transition can be used to continue the data taking without reconfiguring the system, in which case the PAUSED state can be considered as a recover period. The data flow is then stopped.

The ErrorStates cluster is entered via the *error* transition when something unexpected happened in the system that requires user interaction to continue. This cluster is only implemented in the RunControl as it reflects the status of the whole system. It provides the means to modify the client setup during operation. The

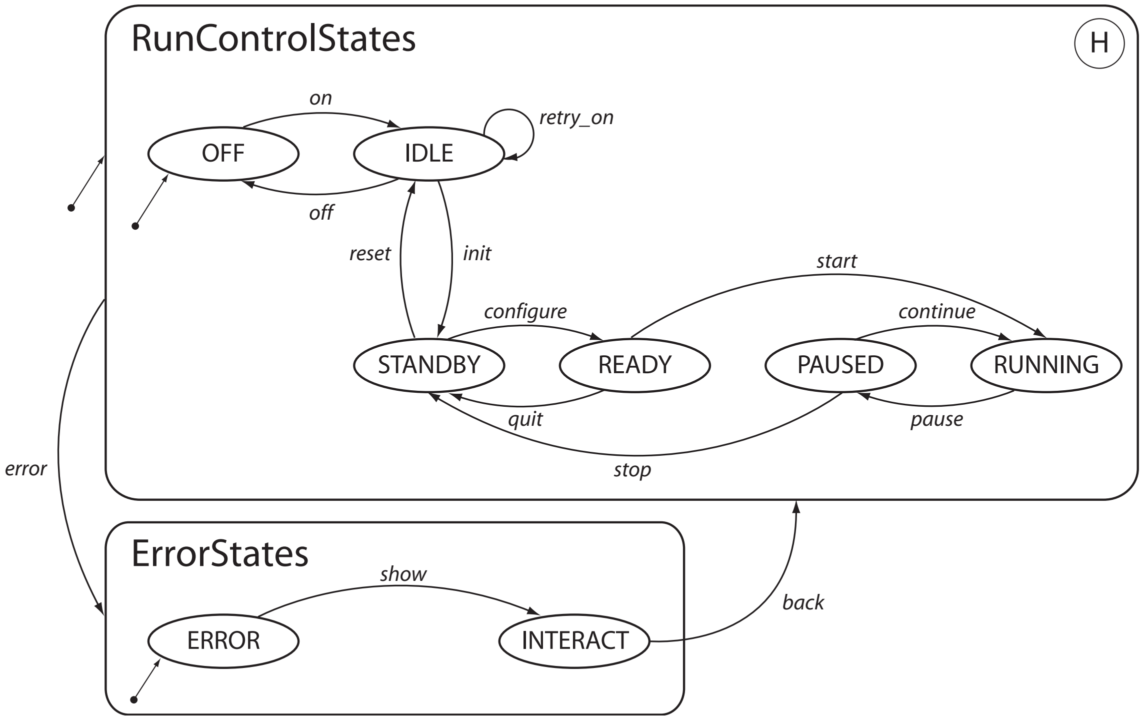

Figure 3.4: *The state machine of the RunControl. It consists of the clusters* RunControlStates *and* ErrorStates*. The* RunControlStates *cluster is entered when the state machine is started, indicated by the symbol* •⟶*. In this cluster the state machine starts in the* OFF *state, indicated by the same symbol. The circled* H *in the upper right corner of this cluster indicates that this cluster has a history. When the cluster is exited and re-entered via the* ErrorStates *cluster, the system will return to the state whichever it was in when the* RunControlStates *cluster was exited. When the* ErrorStates *cluster is entered, it always starts in the* ERROR *state, requesting interaction by the operator.*

ErrorStates cluster can be entered from any state in the RunControlStates cluster when an error occurs, for example a crash of one of the clients. When re-entering the RunControlStates cluster, by triggering the *back* transition by the operator, the system arrives in the state from which the *error* transition was initiated. In the meantime, between exiting a state in the RunControlStates cluster and re-entering it via the ErrorStates cluster, all client processes will remain in the same state, as they do not have this cluster implemented.

Part of the states and transitions in the RunControlStates cluster form the same state machine that is implemented in the clients. In addition, the RunControl has the OFF state that does not appear in the general state machine. The RunControl enters this state when it is started. When the client setup is chosen, the RunControl retrieves all necessary information about the clients from the database, including their start commands and the IP address of their hosts. By initiating the *on* transition, the RunControl launches each client process by executing its start command on the host with its associated IP address. When the client processes are started they will enter the general state machine in the IDLE state. The first action each client undertakes when entering the IDLE state, is broadcasting a message with a unique code to ControlHost. This code consists of the IP address of its host and the nickname of the process. The nickname corresponds to the type of the client, e.g. DaqHarness. As any host can run only one RunControl client of each client type, this code is by construction unique. This message will notify the RunControl, which uses the same unique coding for each client process, that the client process is running. When such a message has not returned after some time, the action can be executed again for specific processes with the *retry_on* transition. This notification method based on the unique code (ID) of each process is the general mechanism that is used for the communication between the RunControl and its clients. This is described in more detail in the following section. At each *start* transition, the run number is incremented by the RunControl. This run number is added to the raw data by the DaqHarness and ScHarness processes. At the same time, the DataWriter creates a new output file (with the run number in the file name) for storing the data on disk. This allows efficient registration of the data.

3.3.4 Communication mechanism

The communication between the processes in the DAQ system is done, like the data transfer, via the ControlHost package. Communication is needed to realise the same state transitions by all clients that were initiated by the RunControl, and to notify the RunControl about the status of each client. In the concurrent state machine model, all processes have to be in the same state to be able to take the next step. As all clients should be in the same state at the same time, the RunControl tracks the state transitions of each client to be able to know the up-to-date state, and to undertake the appropriate action when a crucial error occurred.

A state transition is initiated by the RunControl by sending a specific message to ControlHost that is received and recognised by all client processes as the request to make the same state transition. In general, all clients will undergo the same state transition, and send a reply message to ControlHost accompanied by their unique ID. With each reply message the RunControl can update the client status using the same unique ID. During the period that the RunControl is waiting for the responses from the clients, no interaction with the system is possible. To give the client processes some time to respond, without the possibility of a deadlock, a time-out period is set. When not all clients have responded within this time, the RunControl will decide, depending on the client type, whether this client can be ignored, or a user interaction is needed before continuing.

ControlHost is designed in such a way, that when a process is started, a “Born” message is broadcasted. Similarly, a “Died” message is broadcasted when the process stops. These messages will also be picked up by the RunControl. This mechanism is used to verify the start of the running of a client process when the RunControl launches its start command as described in the previous section. The RunControl is also responsible for terminating the client processes when the system is turned off.

For some state transitions, like the *init* and *configure* transitions, when the system is initialised or configured, some client processes require data to realise the state transition. In these cases the necessary data, specific for each client process, will be added to the state transition message that is sent to the client via ControlHost. The *start*, *pause*, and *stop* transitions are accompanied by messages to the master clock on shore, which in its turn will send a hardware signal to the off-shore LCM clocks for the synchronisation of the ARS chips.

Chapter 4

Data taking and processing

During data taking all data are sent from the detector to the shore station, in accordance with the all-data-to-shore concept (see section 3.1). The readout of the detector and the processing of the data are realised by the Data AcQuisition (DAQ) system. As can be seen from the counting rates taken with the prototype detector, the singles rate varies in time (see section 2.9). With an average singles rate of 70 kHz the data output rate of the detector is about 0.4 GB/s. As the detector will in principle continuously take data, during night and day, this amounts to a data output rate of 34 TB per day, and 13 PB per year.

Most of the data is background, mainly caused by bioluminescence and the decay of ^{40}K. There is also a contribution from atmospheric muons. Only a small fraction of the data is produced by muon tracks originating from neutrino interactions.

Because of the high data output rate of the detector, the data have to be filtered. This is done by processing the data with standard computers running a designated software program. The processing involves the separation of the background from the signal and as a result the reduction of the data output for storage. The data that are stored after processing are used for physics analysis.

This chapter describes two methods of data taking and processing. One of these methods is applied when a GRB is detected by a satellite.

4.1 Data taking

Every Local Control Module (LCM) in the detector has a readout system. This system consists of several custom designed Analogue Ring Sampler (ARS) chips, a Field Programmable Gate Array (FPGA), and a processor. The ARS chip digitises the analogue signals of the photomultiplier tubes (PMTs), the FPGA buffers these data, and the processor sends the buffered data to shore.

The digitisation in the ARS includes timing of each PMT signal and the determination of the total charge of the pulse. The settings of each ARS chip can be adjusted, including the two main parameters: threshold and integration gate. The voltage threshold is set to eliminate small pulses due to the dark current in the PMT. Its typical value corresponds to 0.3 photo-electrons. The gate is set to integrate most of the PMT signal, but limiting the contribution of electronic noise. The typical value of the integration gate is 30 ns.

A master clock with a frequency of 20 MHz is located on shore. The common clock signal is distributed to all LCMs in the detector and is used by the ARSs to timestamp each PMT signal above threshold. By interpolating between two consecutive clock pulses the obtainable timing resolution of the ARS is about 0.2 ns.

The combined time and charge information is referred to as a Single Photon Electron (SPE) hit, or hit for short. Its size amounts to 6 bytes. To compensate for the dead-time in the ARS due to the digitisation process, two ARSs are connected to each PMT, which operate in turn.

The data of each ARS are transferred inside the FPGA into separate frames of about 13 ms using the same clock signal as for the timestamping of the PMT signals by the ARS. The data frames are sent separately to shore by the LCM processor using TCP/IP. The on-shore data processing system consists of a farm of PCs. A single frame contains all data of one ARS in a particular time window. All frames belonging to the same time window are sent to the same processor in the on-shore data processing system using its IP address, as shown in figure 4.1. The collection of frames belonging to the same time window is called a TimeSlice. As a result, a TimeSlice contains the data from all ARS chips in the detector that were registered during the same 13 ms. This period is chosen such that its duration is long compared to the duration of a physics event to minimise the chance of having an event crossing the boundaries of a TimeSlice. As it takes a muon 2 μs at most to traverse the detector, the signal loss due to the finite duration of a TimeSlice can be safely neglected.

4.2 Data processing

All frames belonging to the same time window are sent to one of the PCs in the on-shore data processing system. Each of these PCs is running the DataFilter program that filters the physics events from the data in real time. For a farm consisting of 100 PCs, the time available to process a TimeSlice is 100 times its duration. For a singles rate of 70 kHz it takes the DataFilter program on a PC with a 2.8 GHz CPU about 130 ms to filter a single TimeSlice. So with this number of PCs in the processing farm, the DataFilter will be finished processing a TimeSlice when it receives the frames of the next TimeSlice.

The DataFilter program has an algorithm implemented that looks for space-time correlations in the data, as explained in section 4.4. When a sufficient number of correlated hits is found that resembles the data produced by a muon traversing part of the detector, the data are considered as a physics event and are stored on disk. Despite the fact that most of the data consist of background, many such correlations will be found. Most of these will be accidental correlations that will be found more

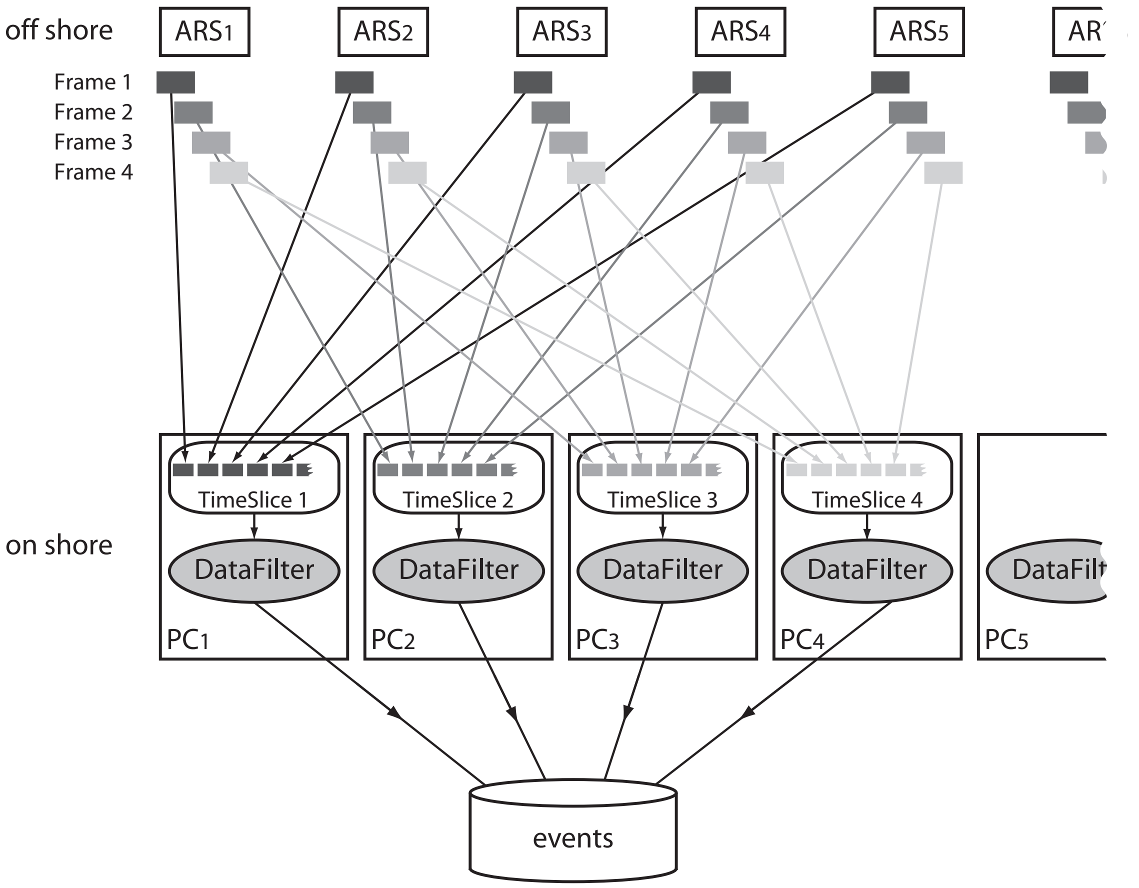

Figure 4.1: *The processing of the data based on TimeSlices. All frames belonging to the same time window are sent to a single PC. The DataFilter program running on each PC will process the data. With 100 PCs, each PC has to be finished with processing the* n^{th} *TimeSlice when it receives the frames of the* $(n+100)^{th}$ *TimeSlice. All physics events are stored on disk.*

often when the random background rate increases. The event rate after processing of the data is about 3 Hz. The data rate is then reduced by a factor of 5×10^4 to about 7.5 kB/s, as the typical size of an event that is found in the random background is about 2.5 kB.

To handle the high background rates, and to be able to process the data in real time, severe cuts have to be applied during the processing of the data, which will result in loss of signal. Considering the relatively short time it takes a standard PC to filter a TimeSlice, only a fraction of the data processing PCs will be needed to filter the data in real time. The other PCs will be used in special cases, as is explained in the following section.

4.3 Special data taking

In some cases it is desirable to buffer as much data as possible before filtering it. Such cases are special astrophysical events which are believed to produce neutrinos, and that are announced at the moment they are detected, such as gamma-ray bursts (GRBs). The PCs in the data processing system can contribute to this buffering task. The spare CPU time is especially advantageous when applying special data taking and processing for these events.

The software program grb_trigger is part of the DAQ system. Like all other programs in the system it communicates via the central data distribution package ControlHost (see section 3.1). The grb_trigger program has a socket connection with IBAS and GCN (see section 1.4). When it receives a message from either of these systems it analyses the contents and subsequently notifies other programs in the system via ControlHost to operate accordingly.

The different message types are described in section 1.4. In case of a GRB alert, the grb_trigger program will notify all DataFilter programs immediately. They will stop filtering the data and instead write all raw data to their local disks, as shown in figure 4.2. This will continue for a few minutes, since a GRB lasts for a relatively short time. As a result, all raw data that could contain a time correlated neutrino signal are on disk. After this period the system will go back to normal data taking, where the data are filtered directly.

Subsequent to the initial alert message, up to about 24 hours, messages with updated information about the GRB can follow, even when afterwards it appeared to be a false alarm. The information of importance in these messages is the refined position of the GRB on the sky, and whether it is excluded or confirmed that it concerns a real GRB. Each of these messages will be received by the grb_trigger program, and registered in the database, including the alert messages.

When a real GRB is not excluded, the grb_trigger program will use the most refined position it received as the definite position of the GRB. With this position the program FlashBack will be initialised. This is a data processing program that has an algorithm implemented that does not, like the DataFilter program, look in all directions for space-time correlations in the data, but looks only in the specified direction. The raw data that were stored on disk during the GRB will be filtered by FlashBack using the definite position of the GRB as the muon direction, and hence the neutrino direction. The events found are stored on disk.

Considering the frequency at which the alert messages are received (see figure 1.6) it is preferred to process the unfiltered data taken after an alert within a few hours. This can be realised as for 70% of the valid alert messages the final position of the GRB is sent within 6 hours after the GRB detection (see figure 1.8).

The different processes related to the burst that are assumed to produce neutrinos take place within a few burst durations around the burst (see section 1.3). Taking this into account, and the average duration of a long GRB (see section 1.1), the special data taking at the time an alert message is received will last for a few

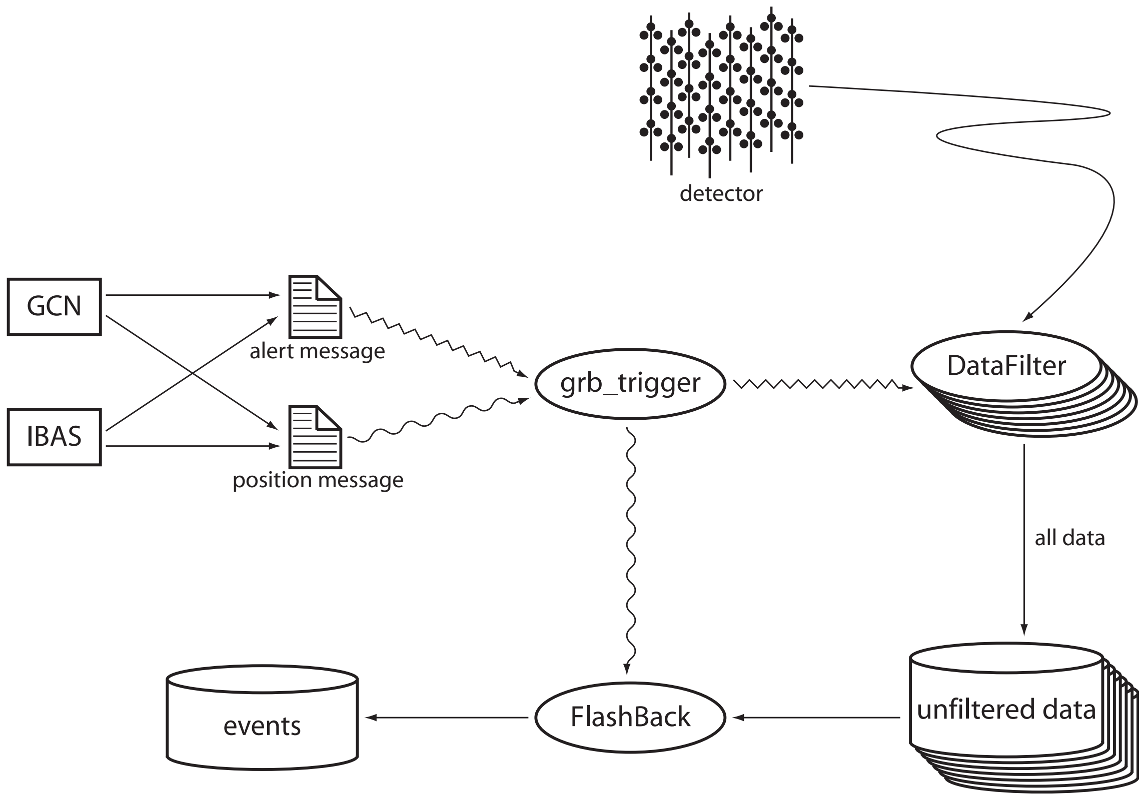

Figure 4.2: *Special data taking when a GRB is detected by using the GCN and IBAS systems as external triggers. When the grb_trigger program receives an alert message, indicated by the zig-zag arrows, the DataFilter programs are instructed to stop filtering the data. Instead all data are written to disk for a few minutes. Later, when the final position of the GRB is received, indicated by the wavy arrows, the FlashBack program will be initialised with this position. The unfiltered data on disk will be filtered offline, using this information. The events found in this way are stored on disk.*

minutes. In addition to these data some extra raw data will be saved to disk, which were taken before the alert message arrived, and that are in the memory of the data processing PCs, as shown in figure 4.3. Apart from filtering the data, the data processing PCs also serve as a kind of buffering system. When a DataFilter program received the data for a complete TimeSlice, it is not immediately filtered. Instead the filtering is delayed to have the raw data in memory as long as possible. With 100 PCs, and a RAM of 1 GB in each PC, there will constantly be 100 GB of raw data in the memory of the PCs. At the assumed singles rate of 70 kHz this corresponds to about 250 seconds of data. This period depends on the final number of PCs in the system, the size of their RAM, and the singles rate.

So at the time a GRB is detected by a satellite, raw data that were recorded prior to this moment are still in the buffer. These data will include any possible

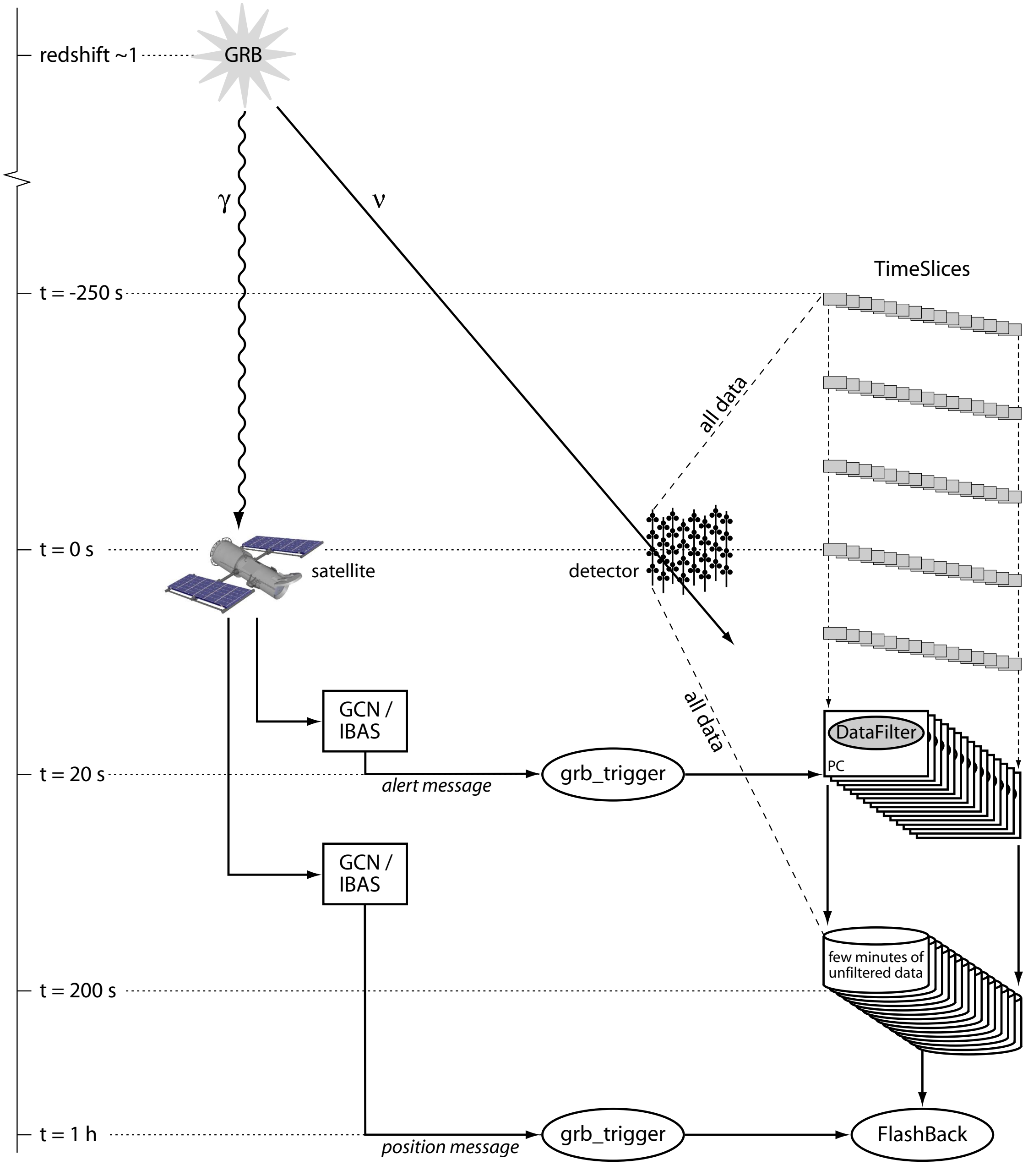

Figure 4.3: *Timeline of the different events during a GRB. The memories of the data processing PCs contain data that were recorded prior to the moment the GRB is detected by the satellite. When the alert message is received by the grb_trigger program, all raw data are saved to disk for a few minutes, including all data in memory. The data in memory contain the data taken before the alert and during the delay of the message from the satellite to the grb_trigger program. When after an hour the definite position of the GRB is known, the data are filtered.*

early neutrino signal that arrived at the detector before the GRB was detected by the satellite. Also the neutrino signal that would otherwise get lost because of the delays in the transmission of the GRB message will be covered by this buffering. As can be seen from figure 1.7, the delay between the detection of a GRB and the arrival time of the corresponding alert message is in 40% (75%) of the cases less than 20 (100) seconds. When an alert message is received by the grb_trigger program, not only all data that are taken during the following few minutes will be saved to disk, but also the data in memory. In this way all raw data within a few burst durations before and after the burst will be available.

The filtering of the stored data will be done offline, after the message with the final position of the GRB is received. The algorithm that is implemented in the FlashBack program to filter these data uses space-time correlations that are more strict than the standard algorithm used by the DataFilter program, as the direction of the neutrinos is known (see section 4.4). As a result, much looser filter conditions can be applied. Consequently the time to filter a TimeSlice in this situation takes longer: a 2.8 GHz CPU needs about 14 seconds to filter a TimeSlice with these conditions, in which case 15 PCs are needed to filter the GRB data within 6 hours. This period is tolerable considering the expected frequency of the alert broadcasts (see figure 1.6). The PCs that are used during normal data taking are also used in the case of a GRB event, in the first place for keeping data in memory, and also for the processing of the data that were taken during the event.

4.4 Cluster algorithms

The algorithms that are implemented in the data processing software have the task to filter physics signal-like data from background. They look for space-time correlations in the data, which imply the presence of a physics signal. From the arrival times of the hits, and the positions of the PMTs, they calculate if hits could originate from Cherenkov light produced by a muon traversing the detector. A number of hits that is correlated in this way form a cluster. If the cluster meets the requirements, it is considered to be a physics event, which is stored on disk. In the physics event the hits that form the cluster are called triggered hits. Apart from the triggered hits, the physics event will also contain all hits within a time window of about 2 μs around the duration of the cluster, which is the maximum time a muon needs to travel through the detector.

From the raw data (called level 0 or L0 hits), the cluster algorithm in the DataFilter program first creates a reduced data set before calculating if hits are correlated. The hits in this data set, called level 1 or L1 hits, meet one of the two following requirements: they are either local coincidences, or they have a large charge. A local coincidence is found when at least two hits occur within 20 ns on two different PMTs on one storey. Two more or less simultaneous hits on one storey are more likely to be caused by a muon than by background. The contribution of bioluminescence to the L0 background is assumed to arise from many uncorrelated processes. Therefore the L1 hits resulting from this background are only caused by accidental coincidences. In the other significant contribution to the background, the decay of ^{40}K, a low-energy electron (1.3 MeV) is produced which also emits Cherenkov light. As the electron undergoes many elastic scatterings, the light is emitted isotropically. The contribution of real coincidences caused by these photons to the L1 rate is estimated to be less than 5% [82]. The alternative requirement for a hit to be selected for the reduced data set is a large charge. The charge of a hit is considered large when it corresponds to at least 2.5 photo-electrons. Like in the case of a local coincidence, such a large charge is unlikely to be produced by background. The reduction of the data from L0 to L1 hits corresponds to a factor of more than 300. This is necessary to be able to filter the data in real time.

Subsequently, the cluster algorithm in the DataFilter program uses the following causality relation to search for correlations in the found L1 hits

$$\mid \Delta t \mid \times \frac{c}{n} \leq D \tag{4.1}$$

where Δt is the time difference between two hits, D is the 3D distance between the corresponding PMTs, c is the speed of light, and n is the refractive index of the water. Due to uncertainties in the positions of the PMTs, timing calibration, and scattering of photons in the water, an additional time difference of 20 ns between hits is taken into account. This cluster algorithm looks if two L1 hits, given their distance and difference in hit times, could have been caused by a muon traveling in any direction. To suppress the random background sufficiently, the requirement for a physics event is that the cluster contains at least 5 L1 hits.

The cluster algorithm in the FlashBack program uses the directional information that it receives from the IBAS or GCN system. This direction indicates the position of a detected GRB on the sky, which corresponds to the direction of the neutrinos it emits. The direction of the muons that originate from these neutrinos is on average comparable to this direction, but the angular spread depends on the neutrino energy. Figure 2.3 shows the angular difference between the initial neutrino direction and the direction of the produced muon.

The neutrino direction will be used in the cluster algorithm of FlashBack as the muon direction. This direction is given in the equatorial coordinates right ascension and declination (J2000 [90]). These will be transformed by the grb_trigger program into rotation angles with respect to the coordinate system used by ANTARES. The z-axis is chosen along the direction of the muon by rotating the coordinate system using the given zenith angle θ and azimuthal angle ϕ. Consequently the coordinates of the PMTs change to the new positions in the rotated coordinate system as shown in figure 4.4.

By using these new coordinates, equation 4.1 can be constrained further. Figure 4.5 shows a muon traversing part of the detector, meanwhile emitting Cherenkov light. The direction of the muon is upwards, as in the rotated coordinate system

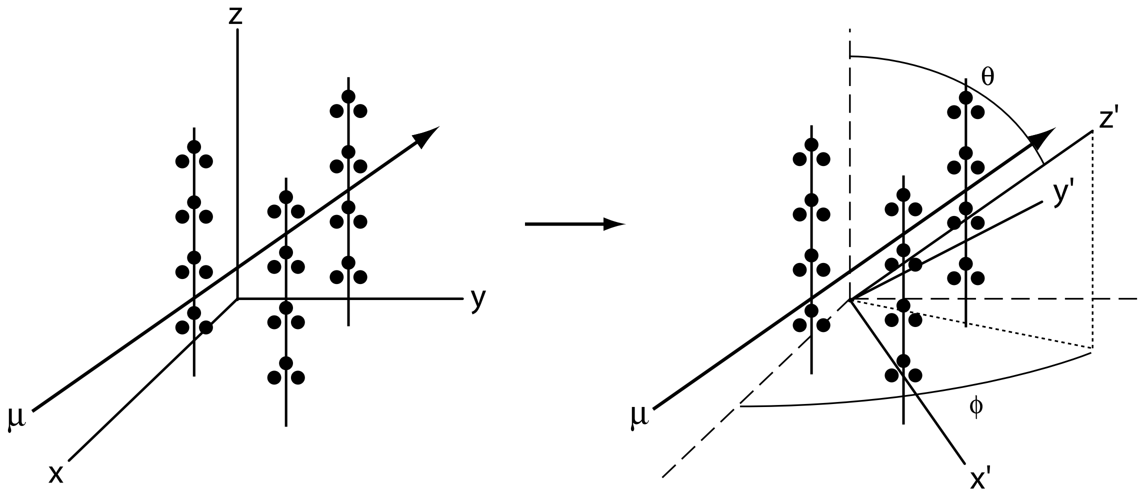

Figure 4.4: *The muon direction, approximately the same as the neutrino direction, is indicated by the zenith angle θ and azimuthal angle ϕ. The coordinate system is rotated so that the z-axis points in the same direction as the neutrino.*

this direction is parallel to the z-axis.

The expected arrival time t_j of a Cherenkov photon on $\mathrm{PMT_j}$ is then given by

$$t_j = t_0 + \frac{1}{c}\left(z_j - \frac{r_j}{\tan\theta_c}\right) + \frac{1}{v_g}\frac{r_j}{\sin\theta_c} \tag{4.2}$$

where t_0 is some reference time, v_g the group velocity of light in water [60], and θ_c the Cherenkov angle. The second term is the time it takes the muon to travel to the point where the detected photons are emitted, and the third term is the time it takes these photons to travel to $\mathrm{PMT_j}$. Equation 4.2 can be simplified by introducing the constant $\kappa = \frac{c}{v_g}\frac{1}{\sin\theta_c} - \frac{1}{\tan\theta_c}$ to

$$t_j = t_0 + \frac{1}{c}(z_j + \kappa r_j) \tag{4.3}$$

For the couple of PMTs 1 and 2 in figure 4.5, the parameters r_1 and r_2 are the distances of closest approach from the PMTs to the muon track. As the position of the muon track is not known, only its direction, the values of r_1 and r_2 are not known. However, the value of the factor $(r_2 - r_1)$, obtained when two hit times are compared, is maximal when the muon crosses one of the PMTs. Its maximum value is then the 2D distance between the positions of the two PMTs projected on a plane perpendicular to the muon track, indicated in figure 4.5 by the symbol R. The difference in hit times of the two hits can then be constrained as follows

$$\frac{1}{c}(z_2 - z_1) - \frac{\kappa}{c}R \;\le\; t_2 - t_1 \;\le\; \frac{1}{c}(z_2 - z_1) + \frac{\kappa}{c}R \tag{4.4}$$

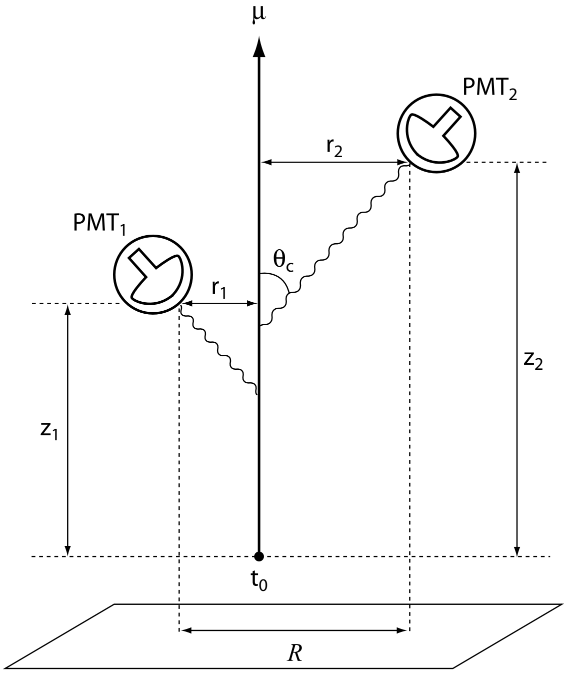

Figure 4.5: *Schematic view of a muon traversing part of the detector. The Cherenkov photons, indicated by the wavy arrows, are emitted under an angle θ_c with respect to the muon track.*

which is the causality relation used by the FlashBack filter to look for correlated hits in the data. This relation is more stringent than equation 4.1 as the two terms with the factor $(z_2 - z_1)$ have the same sign. Like for the DataFilter program, an extra time difference of 20 ns is taken into account considering the calibration uncertainties and light scattering.

Since equation 4.4 is more stringent than equation 4.1, the L0 hits are used to find correlations in the data, instead of L1 hits. Unlike the DataFilter program, the FlashBack program does not filter the data in real time, in which case it is possible to consider all hits. Also, signal hits that do not meet the requirements for L1 hits, and that would otherwise get lost, will be taken into account. A physics event is found when at least 6 L0 hits are correlated according to equation 4.4.

The combination of the strict cluster algorithm and the use of L0 hits results in a high event output rate because of the large number of hits involved. At a background rate of 70 kHz the total rate of L1 hits is about 0.2 MHz, but the total rate of L0 hits is 63 MHz. In random background it is often seen that distant hits are correlated, while there are no intermediate correlated hits. As emitted Cherenkov light from a muon will be detected mainly within a certain roadwidth along its path, an extra constraint is used in equation 4.4 to minimise the number of accidental correlations due to random background: a maximum is set to the transverse distance between two correlated hits. The intensity of the Cherenkov light decreases with the flight length of the photons $\frac{r_j}{\sin\theta_c}$ (see figure 4.5) as

$$I \propto \frac{\sin\theta_c}{r_j} e^{-\frac{r_j}{\sin\theta_c \lambda_{abs}}} \tag{4.5}$$

where the absorption length λ_{abs} is typically 60 m. A reasonable value for the maximum transverse distance is therefore about twice the absorption length.

The transverse distance between two PMTs is indicated in figure 4.5 by the symbol R. Two hits are now correlated when their hit times satisfy the causality relation 4.4, where R does not exceed the maximum transverse distance. The choice of the value of the maximum transverse distance depends on the direction of the muons. The event rate from simulated random background as a function of the zenith angle θ is shown in figure 4.6. The different lines in the figure represent the event rates for different values of the maximum transverse distance. As expected the event rate decreases significantly for smaller values of the maximum transverse distance. In addition, the event rate drops when the direction changes from vertical to horizontal because of the large difference in the spacing between neighbouring storeys (14.5 m) and strings ($\sim$ 60 m). For vertical directions all storeys on a string will be within the maximum transverse distance. At horizontal directions, when the z-axis is perpendicular to the strings, only part of the PMTs on a string will be within the maximum transverse distance. Other PMTs that could meet the requirements of the causality relation belong to a different string which is at least 60 m away. So for vertical directions more PMTs are covered.

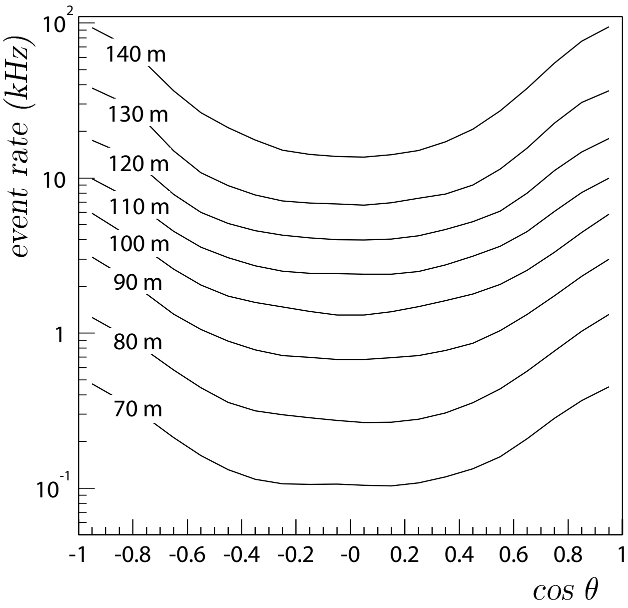

Figure 4.6: *Event rate from simulated random background at 70 kHz for different values of the maximum transverse distance. Because the θ dependence is dominant, the rates shown are averaged over ϕ.*

When the event rate is high, the events start to overlap in time, in which case they are merged into one cluster. The cluster size of the resulting cluster will then increase. Figure 4.7 shows the distribution of cluster sizes of the events found in random background for one particular direction at different event rates. The different event rates are obtained when the maximum transverse distance is varied. Events resulting from random background data have in general small cluster sizes provided that they are not merged. At low event rates only few clusters will be

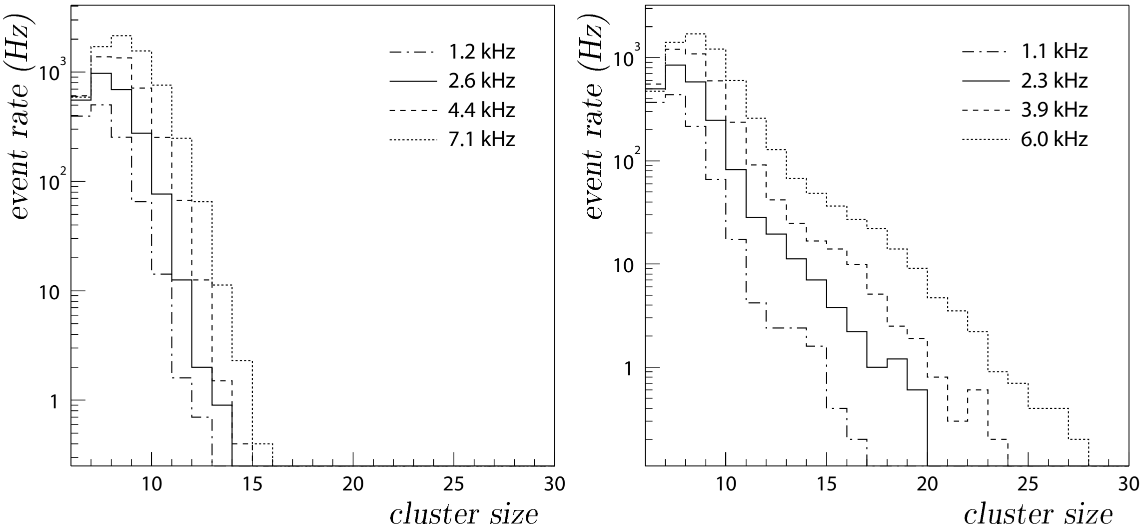

Figure 4.7: *Distribution of cluster sizes of the events found in random background at different event output rates. Left: without merging; events found in background have in general small cluster sizes. Right: after merging; when the event rate increases, more events are merged, and the cluster sizes increase.*

merged. When the number of clusters found gets higher, the chance of having accidentally overlapping clusters increases. Consequently the cluster sizes of the events found will increase. A shallow distribution is more in accordance with signal events than background events. The maximum transverse distance, shown in figure 4.8, is chosen such that the event rate is about 2 kHz for any direction. At this rate the probability that events are merged is about 9%, which is acceptable.

Apart from setting a maximum to the transverse distance, two extra constraints are applied to the clusters found before merging: for small clusters (less than twice the minimum cluster size of 6) a fitting procedure is applied, and each cluster must contain one local coincidence (L1). The fitting procedure that is applied to small clusters, which are probably background, estimates the position of the muon. Initially it does this by taking the weighted average of the PMT positions using the charges of the hits (hits with a large charge are presumed to be closer to the muon track). Subsequently it improves this position using the hit times, where the corrected hit time $t_j - t_0 - z_j/c$ (see equation 4.3) is taken as the inverse weight. This weight corresponds to the transverse distance of the hits to the estimated track. When the probability of the hits for the found track is big enough, the next condition for the found cluster has to be satisfied: only if the cluster contains a local coincidence a physics event is stored on disk.

Table 4.1 shows the decrease in event rate after the successive application of the restrictions where the maximum transverse distance was set for a particular direction according to figure 4.8. As expected, the event rate decreases with each additional

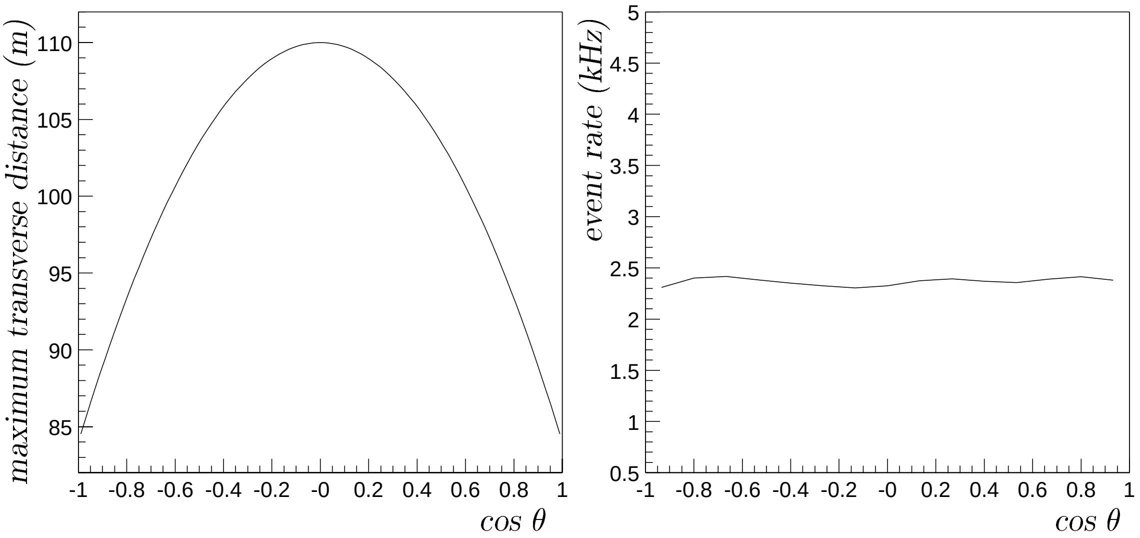

Figure 4.8: *Left: maximum transverse distance as a function of the direction. Right: event rate from random background at a rate of 70 kHz for the maximum transverse distance shown on the left.*

restriction. The linear prefit and local coincidence restrictions were introduced for small clusters, which are most likely background. When neither of these restrictions is used, the event rate is extremely high. This is mainly shown by the event rate before the clusters are merged. Merging of these clusters results in events with huge cluster sizes.

restriction	event rate before merging (kHz)	event rate after merging (kHz)
maximum transverse distance	3543	23.8
linear prefit	18.3	16.1
local coincidence	2.6	2.3

Table 4.1: *The average event rates from random background at a rate of 70 kHz before and after merging, after the successive application of the different restrictions.*

4.5 Background event rates

Most of the events found by the data filter programs consist of accidental correlations caused by the random background. The two other types of background, atmospheric muons and atmospheric neutrinos and antineutrinos, produce correlated data, but also contribute to the overall background. Although atmospheric neutrinos and antineutrinos can produce the desired signal in the detector, they are considered as background because they are not cosmic neutrinos. They are the result of interactions of cosmic rays entering the atmosphere. Table 4.2 contains the event rates using the two different data filter programs for the three different types of background. The contribution due to random background is simulated assuming a singles rate of 70 kHz. The atmospheric muons cover mainly downgoing directions with θ between 0° and 85°, and the atmospheric neutrinos and antineutrinos cover all directions. The atmospheric muons, neutrinos, and antineutrinos were simulated using the models described in section 2.9. For the FlashBack filter four different directions are chosen corresponding to the coordinates of the gamma-ray bursts GRB 030101 ($\cos\theta = -0.07$), GRB 030329 ($\cos\theta = -0.39$), GRB 041006 ($\cos\theta = -0.70$), and GRB 040511 ($\cos\theta = -0.94$).

	GRB	$\cos\theta$	random (Hz)	$\mu_{\rm atm}$ (Hz)	$\nu_{\rm atm} + \bar{\nu}_{\rm atm}$ (Hz)
DataFilter			3	4.5	2.2×10^{-4}
FlashBack	GRB 030101	-0.07	2.2×10^{3}	8.9	6.2×10^{-4}
	GRB 030329	-0.39	2.3×10^{3}	7.1	8.5×10^{-4}
	GRB 041006	-0.70	2.5×10^{3}	3.2	8.3×10^{-4}
	GRB 040511	-0.94	2.5×10^{3}	1.5	7.4×10^{-4}

Table 4.2: *The estimated number of events found per second originating from the different types of background separately for the two filter programs. The events found by the DataFilter program can come from any direction, whereas the FlashBack program looks for events from the directions of the four selected GRBs. The number of atmospheric muons, neutrinos, and antineutrinos per second producing at least one hit in the detector is about 240,* 5×10^{-3}*, and* 2×10^{-3} *respectively.*

The requirement for an event found by the DataFilter program is that it contains at least 5 correlated L1 hits. An event found by the FlashBack program should contain at least 6 correlated L0 hits. In addition, when there are less than 12 hits, the event should meet the requirements of the linear prefit, and it should contain one local coincidence.

In reality an atmospheric muon and an atmospheric neutrino will be accompanied by random background hits. Taking into account the frequency of 70 kHz of the random background hits, an atmospheric muon or atmospheric neutrino event will more often meet the filter requirements. Consequently this will result in a higher event rate for both atmospheric muons and atmospheric neutrinos. For the numbers given in table 4.2 this additional random background is not taken into account. The results indicate the contributions of pure atmospheric muons and atmospheric neutrinos to the total background event rate. In the final analysis the random background will be taken into account when analysing atmospheric muons, neutrinos, and signal, as this will represent the actual situation.

For some directions the event rate from random background is slightly higher than the expected values shown in figure 4.8, where the event rates are averaged over the azimuthal angle ϕ. For certain values of ϕ the event rate can be higher due to the particular geometry of the detector. The combination of the dependence of the atmospheric neutrino and antineutrino flux on the direction (see section 2.9) and the efficiency of the filter for different directions, as is shown in section 4.6, causes the range in the event rates from atmospheric neutrinos and antineutrinos for the different GRBs. The event rate from atmospheric muons decreases as the direction changes from horizontal to more vertical directions. For the GRB with the most upright direction the contribution of the downgoing muons will be smallest as the difference in the two directions is largest.

For the DataFilter program the event rates for all types of background are lower. This is expected because of the more strict requirements for the clusters. These are needed to be able to filter the data online, and to reduce the detector output to a manageable amount of data for the physics analysis. As the DataFilter program looks in all directions for correlations, the found events can come from any direction. The clusters found by the FlashBack program are subjected to looser requirements. This results in a higher event rate, but an increase in the efficiency for physics signal. Although the data output rate of FlashBack is higher than for DataFilter, the found events are all within a time window of a few minutes. Only the data corresponding to a few minutes that were saved to disk after a GRB alert will be filtered by FlashBack, in contrast to the DataFilter program. As the cluster algorithm is initialised with one specific direction, all found clusters will contain hits that satisfy the causality relation for that direction.

As can be seen from table 4.2, the main background to the considered GRBs is due to random background from bioluminescence and the decay of ^{40}K. This background will be eliminated by the analysis of the events (see chapter 5).

4.6 Signal efficiency

The two data filter programs are capable of reducing the random background to an acceptable level. Different constraints are used in the two filter programs to accomplish this reduction. These will unavoidably have an effect on the efficiency to detect neutrinos. Even when such signal events produce enough hits in the detector, some of them will not be considered as an event in the filter process when using either DataFilter or FlashBack. A comparison of their efficiencies as a function of the neutrino energy is shown in figure 4.9. For this, events were simulated coming from directions with fixed zenith angles of 180°, 135°, and 90°, and azimuthal angles integrated from 0 to 2π. The curves in the figure correspond to the fraction of the events that caused at least six hits in the detector found by the data filter programs. The efficiency of the DataFilter program shows an energy threshold at about 200 GeV. Above this threshold its efficiency is about 50%. The efficiency

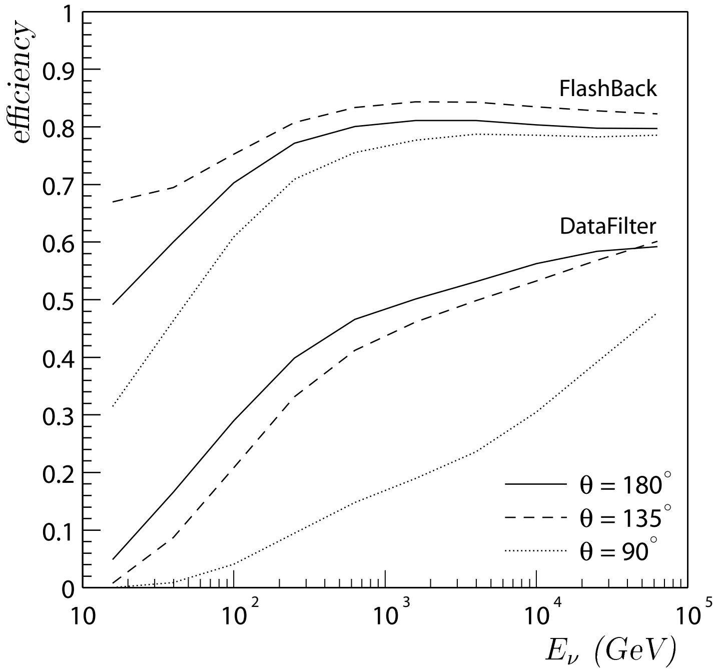

Figure 4.9: *The efficiency of the two cluster algorithms as a function of the neutrino energy. The top three lines are the result of FlashBack, the bottom three lines are the result of DataFilter. The three different line styles show the results for neutrinos coming from directions with zenith angles of* 180°, 135°, *and* 90°.

of the FlashBack program is higher, in particular at low energies. Its efficiency is mainly higher because of the use of L0 hits.

At energies below 200 GeV the efficiencies are in general lower. At these energies muons produce only a few hits in the detector. For several reasons, like late arrival of a Cherenkov photon due to scattering, one or more of these hits might not be considered to be correlated to the other hits by either filter program. Especially for these events the number of correlated hits found by the filter program will more often be below the threshold of the minimum cluster size. The event will then not be found. This effect can also occur at higher energies, when the muon is far outside the instrumented volume, and produces only a few hits on the outer strings of the detector. In general, events at higher energies produce more light. For these events it is irrelevant if a single hit does not satisfy the applied causality relation as there are enough hits left to form a cluster that meets the requirements.

Another origin of inefficiency, apart from the constraints used in the filter programs, is the late arrival times of scattered photons, or photons from secondary electrons or bremsstrahlung. These hits contribute to the normalisation of the efficiency, but can arrive much later than the unscattered Cherenkov photons from the muon, in which case they will not satisfy the causality relation. This effect becomes more visible for higher energies (above 5 TeV) where the efficiency does not increase further, especially for the FlashBack program where the cluster algorithm is more strict. At these energies the muons can be very far from the detector. The spread in the arrival times of the scattered photons that still reach the detector can be too large to be considered correlated by the filter programs.

The DataFilter program shows a remarkably low efficiency for horizontal directions. This is caused by the small number of local coincidences produced by muons from this direction compared to muons from more inclined or vertical directions due to the orientation of the PMTs within a storey.

The FlashBack program uses a maximum value for the transverse distance between PMTs to reduce the background. The differences in efficiencies of this program for different directions can be explained by this constraint as it depends on the direction. For example, for vertical directions distant strings could be excluded completely. The effect of the choice of this value on the efficiency as a function of the neutrino energy is shown in figure 4.10. Simulated events from all directions were

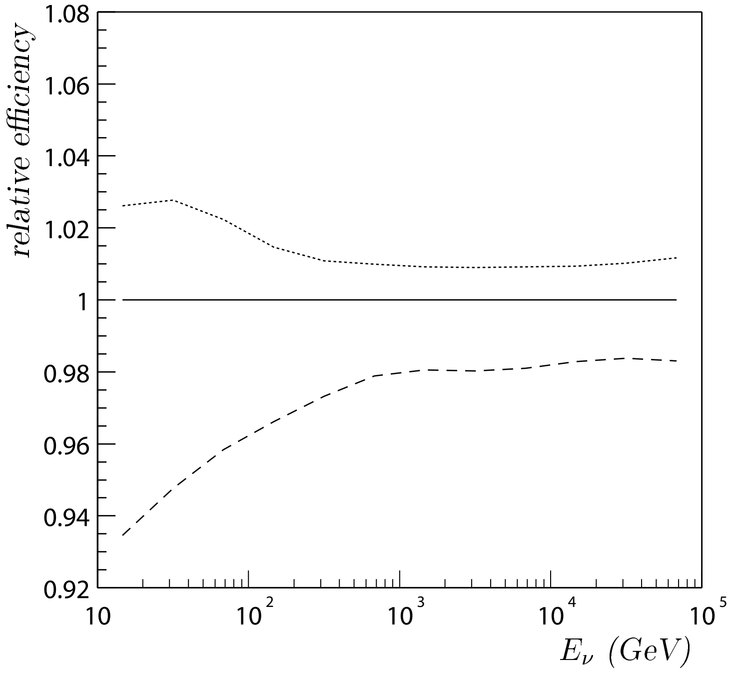

Figure 4.10: *The efficiencies relative to the efficiency with the prescribed maximum transverse distance. The dotted line is obtained when the maximum transverse distance is 1.2 times the prescribed maximum transverse distance, and the dashed line when it is 0.8 times the prescribed maximum transverse distance.*

filtered with the maximum transverse distance chosen 20% larger and 20% smaller than the prescribed value. The curves in the figure show the efficiencies relative to the efficiency with the maximum transverse distance according to figure 4.8. As expected the efficiency is higher when the maximum transverse distance is larger, and lower when it is smaller than normally. At energies above 200 GeV the differences are small, 1–2%. The differences at lower energies are due to the small number of hits that are produced in the detector where the rejection of one hit results more often in the loss of the event. Both the constraints of the linear prefit and one local coincidence have a negligible effect on the signal efficiency of the FlashBack program.

Chapter 5

Analysis of GRB data

The few minutes of raw data that are saved to disk when a GRB alert is received cover a few burst durations before and after this moment. These data are filtered using the specialised filter FlashBack that looks for events from the direction of the GRB and stores them on disk.

As was shown in the preceding chapter, FlashBack is more efficient for signal events than the standard filter DataFilter that is normally used. This difference is mainly obtained by taking all hits into account in the cluster algorithm, not just the hits that are part of a local coincidence and hits with a large charge, as in the case of DataFilter. Also, because of the more strict cluster algorithm used in FlashBack, the filter conditions can be more relaxed than in the case of DataFilter, for example the minimum number of required photons can be reduced. However, as a result of both these features the number of fake events found by FlashBack due to the different types of background is much higher compared to that found by DataFilter.

One way to maximise the discovery potential for the detection of neutrinos from GRBs is to reduce all background to less than one event for a given burst while keeping as much signal as possible. To be able to distinguish the background from the signal all events found are analysed. For this, a software program is used to reconstruct from the data the time and position of the muon where it traversed the sensitive area of the detector. With the reconstruction of the event a likelihood function is maximised. In the GRB analysis, the likelihood values are calculated for different hypotheses to test if the event found is compatible with a neutrino from the GRB.

5.1 Standard reconstruction

The data selected by the filter process cannot simply be regarded as neutrino events without further consideration. Although the specialised data filter finds events from a certain direction, many of these events are caused by background as shown in table 4.2. The random background does not consist of muon-like events at all and should not be considered as signal. The atmospheric muon background produces correlated data, but these are caused by downgoing muons. These events have to be discarded as well. The atmospheric neutrino background shows a signal that resembles the signal of the cosmic neutrinos that are searched for. The small fraction of atmospheric neutrinos that come from the same direction as the neutrinos from the GRB will unavoidably be identified as signal. Atmospheric neutrinos that do not have the same direction as those from the GRB will have to be classified as background. To distinguish the various backgrounds from the signal a detailed analysis is applied to all events found. The filtering was primarily done to get rid of the continuous random background and most of the atmospheric muons. The events from the preferred direction are kept and the rest of the data are left out. To reduce the processing time only the stored events are used for the final analysis.

The analysis of the events is performed by a software program that reconstructs a muon track from the data. The standard reconstruction software in ANTARES, thoroughly described in [83], is used to reconstruct the events that were found by DataFilter, where the direction of the neutrinos is not known. When this reconstruction program is used on events found by FlashBack its performance on data taken during a GRB can be quantified. Figure 5.1 shows the distribution of cluster sizes of the events found by FlashBack and the reconstructed events. The cluster size is the number of correlated hits in the event found by the filter (see section 4.4). About 10% of the events are not reconstructed, most of them have a cluster size of less than 20 hits. One of the features of the FlashBack filter is that its filter conditions are such that it also finds events with low energies that in general produce only a few hits in the detector, and consequently have small cluster sizes. Exactly these events are not reconstructed by the standard reconstruction program. The FlashBack filter efficiency is 60–80% at energies of about 100 GeV compared to

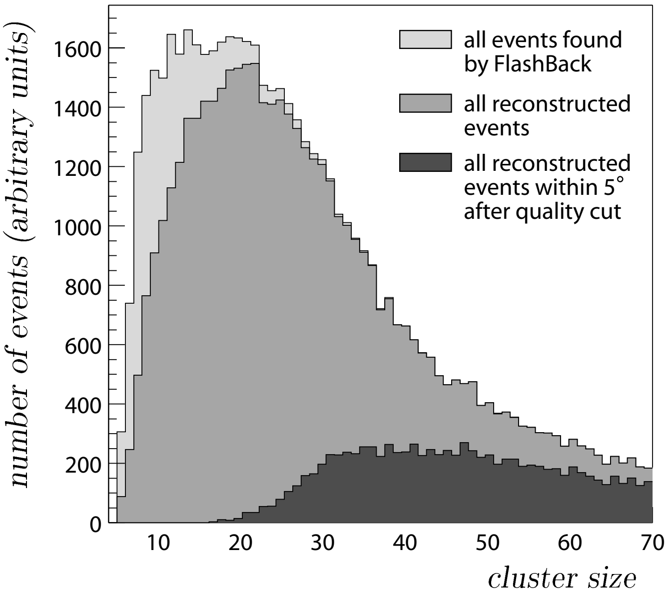

Figure 5.1: *Distribution of cluster sizes of the events found by FlashBack, all reconstructed events, and the events reconstructed within* 5° *from the incident neutrino after the final quality cut was applied. The events were simulated assuming a specific GRB.*

5–30% efficiency of DataFilter (see figure 4.9). This improvement gained in the filter process should not be lost in the reconstruction process. Figure 5.1 also shows the distribution of reconstructed events after the final quality cut, and where the direction of the found track differs less than 5° from the incident neutrino direction. The quality cut in the standard reconstruction is applied to all reconstructed events to minimise the contribution of background, and is based on the likelihood value of the fit used to reconstruct the event. To take the angle between the incident neutrino direction and the muon direction into account, all reconstructed muon tracks that differ less than 5° from the GRB direction are accepted. For neutrinos at a few tens of GeV this angle can be larger (see figure 2.3), but neutrinos with these energies are unlikely to be detected by ANTARES. About 20% of the events are reconstructed within the angular acceptance of 5° using the standard reconstruction program with the final quality cut. To prevent the loss of events in the reconstruction process, a new reconstruction program was developed that is used to analyse GRB data. In this analysis each event is reconstructed several times assuming different directions for the incident neutrino. These results are compared to test the compatibility of each event with the assumption of a neutrino from the given GRB.

5.2 Fitting procedures

Like the standard reconstruction, the reconstruction that is used to analyse the data taken during a GRB consists of a number of fitting procedures: the linear prefit, the M-estimator fit, and the maximum likelihood fit. All fitting procedures are applied to each of the events. The results of the fitting procedures shown do not include a quality cut on the reconstructed events. The final event selection is discussed in the next chapter.

5.2.1 Linear prefit

The linear prefit provides the initial position and time where the muon traversed the detector. Combined with the assumed direction of the neutrinos, this defines a track that is used as starting value for the next fit. The linear prefit is the same as the prefit used by the cluster algorithm, where it was only applied to small clusters. Here it is applied to all events.

Just like when the data are filtered by FlashBack, the coordinate system is rotated so that the z-axis is pointed along the neutrino direction (see section 4.4). The position and time of the muon are estimated using the hits that form the cluster in the event. These are the correlated hits found by the cluster algorithm in FlashBack looking in that same direction. They are presumed to originate from a muon moving in that direction. The average of the hit positions in the rotated coordinate system, weighted with their charge (hits with a large charge are likely to be close to the muon track), is at first taken as the position (x_0, y_0, z_0) of the muon.

The measured hit times corrected for the muon propagation time, i.e. $t_j - \frac{z_j - z_0}{c}$, are averaged to yield the time t_0 of the muon at this position. The transverse positions are then averaged again using the corrected hit times as the inverse weight. The corrected hit time $t_j - t_0 - \frac{z_j - z_0}{c}$ is proportional to the transverse distance of the hits to the estimated track (see equation 4.3).

To demonstrate the accuracy of the track found by the prefit, the distribution of the residuals of the position and time of the fitted track and the muon are shown in figure 5.2 for simulated events. The distributions are well centered at zero. The RMSs of the position and time residuals are about 10 m and 80 ns respectively. About 40% of the tracks found have a position residual of less than 20 m and a time residual of less than 20 ns compared to the muon track.

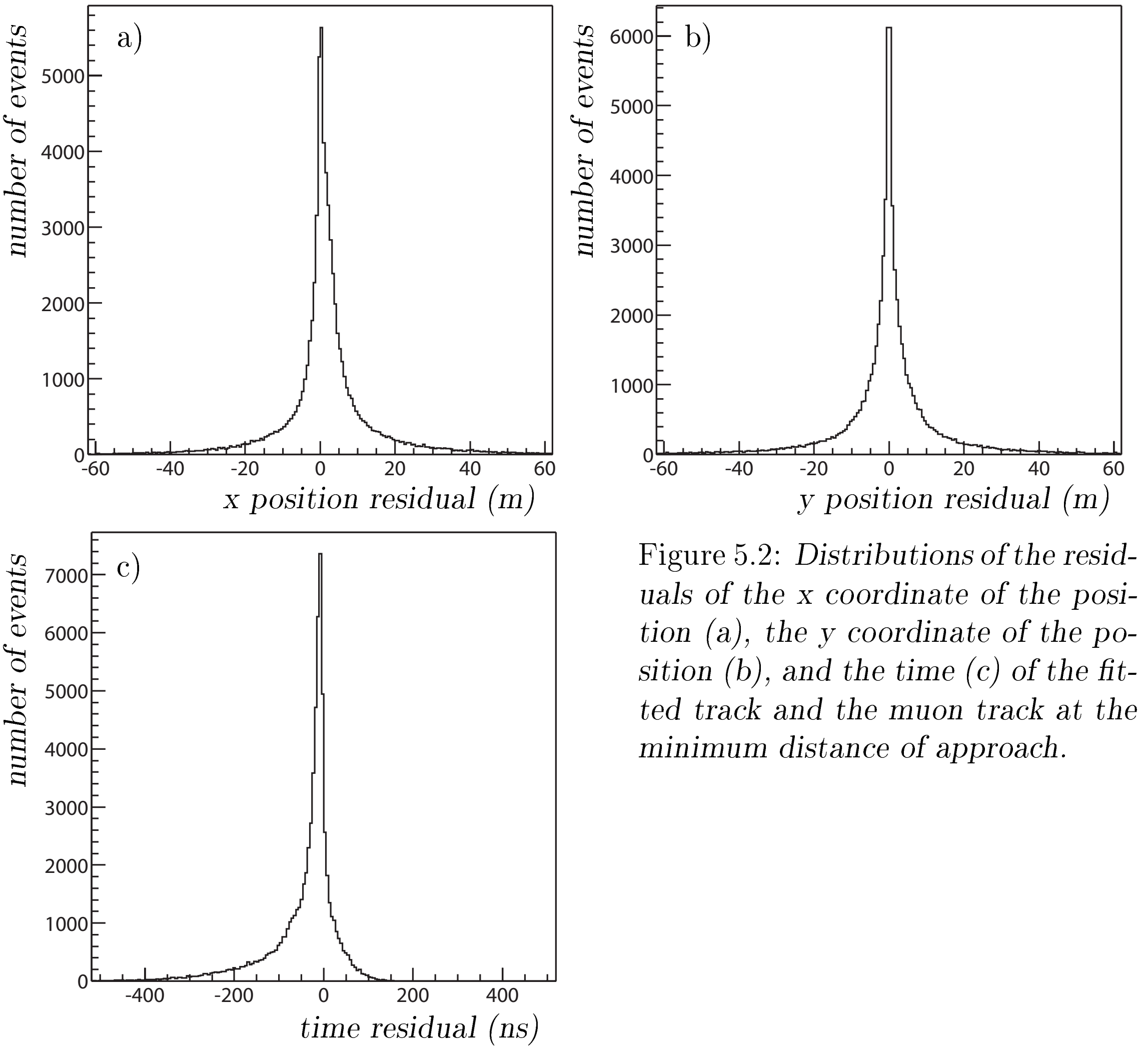

Figure 5.2: *Distributions of the residuals of the x coordinate of the position (a), the y coordinate of the position (b), and the time (c) of the fitted track and the muon track at the minimum distance of approach.*

5.2.2 M-estimator fit

As the maximum likelihood fit requires accurate starting values for the track parameters [83], a so-called M-estimator fit [91] is applied to the data after the prefit. In the maximum likelihood fit the data are fitted using Probability Density Functions (PDF) that describe the expected distribution of the hit time residuals (this is the time difference between the measured and predicted hit times). At large time residuals these functions do not depend on the track parameters. The M-estimator fit can deal with hits with large time residuals and provides track parameters that match these PDFs.

In the M-estimator fit the expression

$$M = \sum_i \rho\left(\frac{\Delta t_i}{\sigma_i}\right) \tag{5.1}$$

is minimised, where Δt_i is the time residual, σ_i is the error on the measured hit time, and $\rho(z)$ is the function

$$2\sqrt{1 + z^2/2} - 2 \tag{5.2}$$

The assumed error on the hit time depends on the charge of the hit and is typically 5 ns.

The track found by the prefit is used as starting value for the M-estimator fit. The M-estimator fit uses an iterative procedure to find improved track parameters. The position, zenith angle, azimuthal angle, and t_0 of the track are the free parameters in the fit. The summation in equation 5.1 includes the hits in the hit selection that is done first. Only the hits in the cluster that lie within a time window of ±150 ns around the predicted hit time assuming the track found by the prefit, and that are less than 100 m away from this track, are used for the M-estimator fit. To remove the directional bias, the initial track is rotated several times and the M-estimator fit is repeated. By using different starting values, a track with a better likelihood could be found. The track found by the M-estimator fit with the best likelihood is taken as input for the final fit.

The results of the M-estimator fit are shown in figure 5.3. The RMSs of the position and time residuals are about 1 m and 5 ns respectively. About 80% of the tracks found have a position residual of less than 20 m and a time residual of less than 20 ns compared to the muon track. Compared to the results of the prefit, the M-estimator fit provides more accurate track parameters. This is necessary and sufficient for the final fit.

The distribution of the angle between the direction of the track found by the M-estimator fit and the neutrino is shown in figure 5.4. In general, the reconstruction procedure finds track parameters compatible with the measured hit times and hit positions. This will correspond to a muon track originating from a neutrino

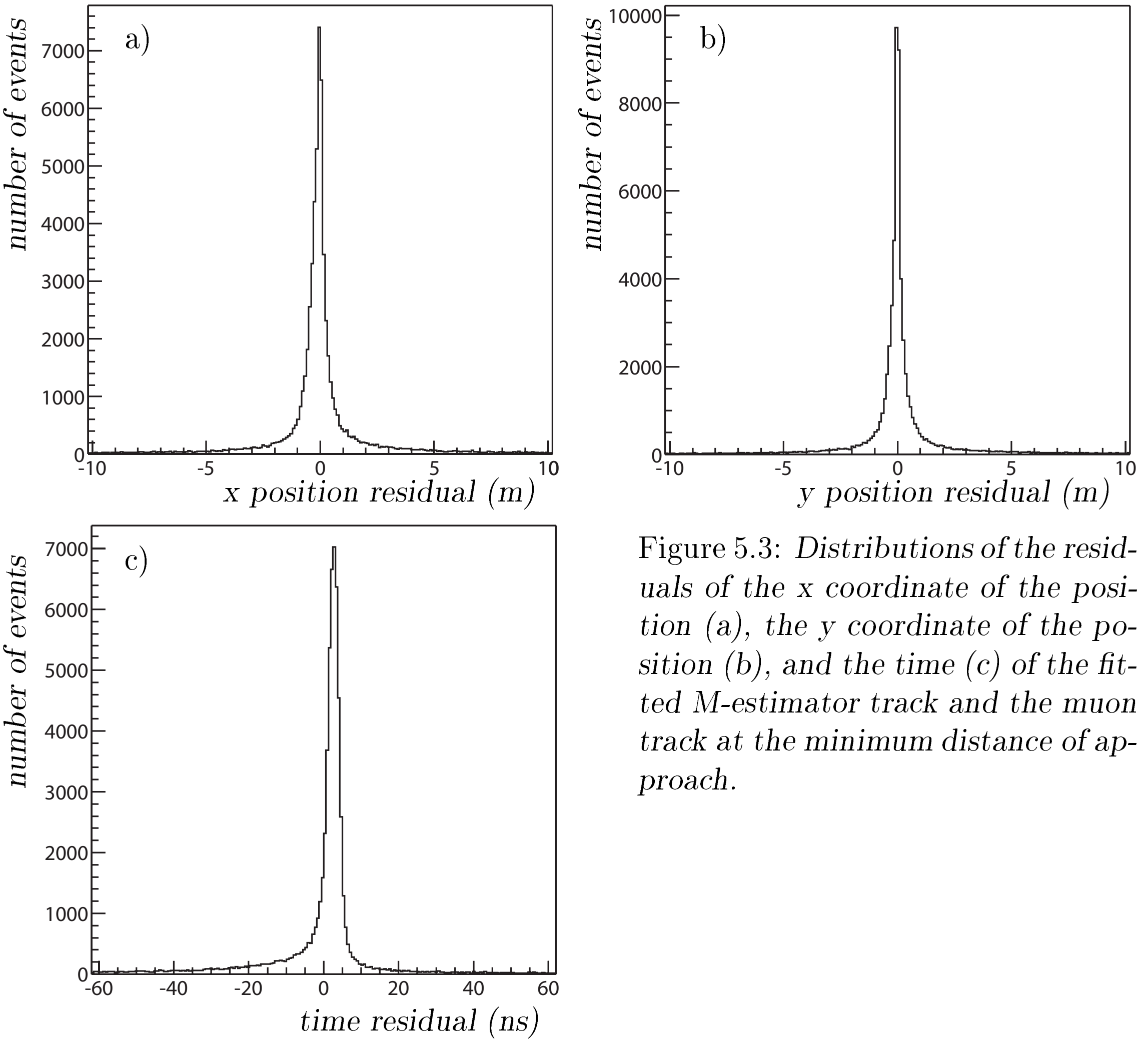

Figure 5.3: *Distributions of the residuals of the x coordinate of the position (a), the y coordinate of the position (b), and the time (c) of the fitted M-estimator track and the muon track at the minimum distance of approach.*

interaction. The quality of the reconstruction process is normally indicated by the angle between the fitted track and the muon. However, as in this case the reconstruction looks for a signal from the GRB direction, the direction of the fitted track is compared here with the neutrino direction. As can be seen from figure 5.4, for about 70% of the events the angle between the track found by the M-estimator fit and the neutrino is smaller than 5°.

5.2.3 Maximum likelihood fit

The best track found by the M-estimator fit is used as starting value for the maximum likelihood fit. In order to use as much data as possible for this fit, a new hit selection is done where all hits that are stored in the event are considered, not just the hits in the cluster (see section 4.4). All hits within a time window of ±250 ns around the predicted hit time considering the track found by the M-estimator fit

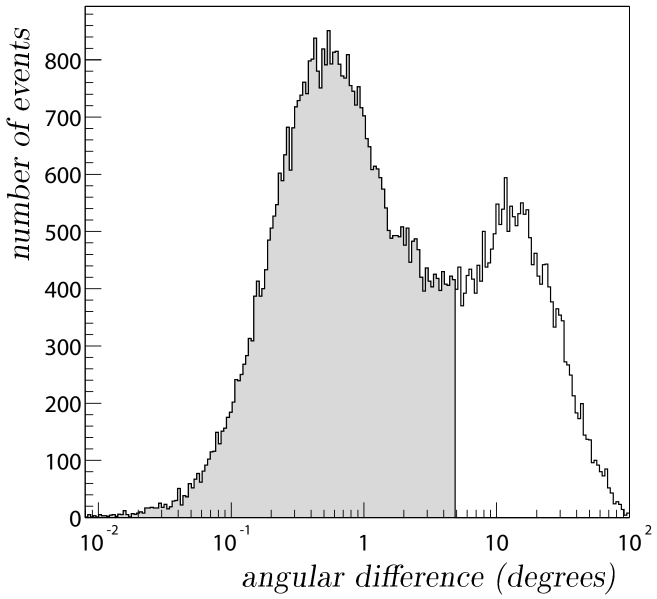

Figure 5.4: *The distribution of the difference between the direction of the track found by the M-estimator fit and the neutrino. The shaded area shows the events for which this difference is less than* 5°*.*

are used.

The PDFs that are used to fit the data are described in [83]. They describe the expected distribution of the time residuals of the hits. Depending on the charge of the hit a certain PDF is used. Figure 5.5 shows the PDFs for different charges for time residuals between -250 ns and $+250$ ns. The PDFs are normalised to unity for this interval. All hits in the hit selection are within this time window. The PDFs show a sharply rising peak at the predicted arrival time of the photons. The peak gradually decreases into a long tail towards bigger positive time residuals due to processes like scattering of the photon in the seawater (see figure 2.12). Apart from the signal peak there is a constant contribution from the random background. As both the random background and the signal are taken into account in the PDF the use of all hits in the event is justified. The contribution of the random background to the PDF is shown by the baseline at negative time residuals. This baseline has a lower probability for larger hit charges. In general, hits with a large charge are assumed to come from the muon. The probability that such a hit is caused by the random background is very small. Hits with a small charge are more likely to be caused by the random background. As a result the baseline for small charges is higher.

In the maximum likelihood fit the logarithm of the function

$$L = \prod_i P(\Delta t_i) \tag{5.3}$$

is maximised [91], where L is the likelihood, P is the PDF shown in figure 5.5, and Δt_i is the time residual. It quantifies the agreement between the data and the PDFs using the track parameters found by the M-estimator fit. The maximisation is done iteratively such that the track parameters are adjusted to obtain a maximum of the function, which corresponds to the best fit parameters. The probability of the data

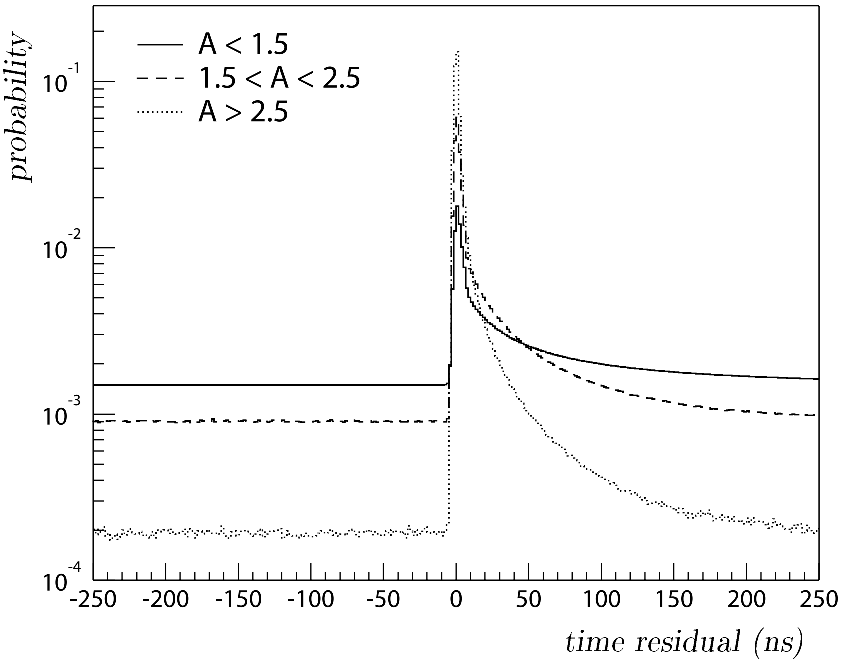

Figure 5.5: *The PDFs as a function of the time residual for different hit charges (A) in number of photo-electrons.*

given the track parameters is defined as the likelihood. The fit procedure finds the values of the track parameters that maximise this likelihood.

The track found by the maximum likelihood fit is the final result of the reconstruction process. The result of this fit is shown in figure 5.6. The RMSs of the position and time residuals are 1 m and 5 ns respectively. About 80% of the tracks found have a position residual of less than 20 m and a time residual of less than 20 ns compared to the muon track.

The angle between the direction of the reconstructed event and the neutrino is shown in figure 5.7. For about 70% of the events the angle between the track found by the final fit and the neutrino is smaller than 5°. The track parameters provided by the M-estimator fit shown in figures 5.3 and 5.4 are not much improved by the maximum likelihood fit. The purpose of the final fit is to obtain the likelihood values that are eventually used to separate the signal from the background.

When this analysis is used to reconstruct the zenith angle and azimuthal angle of the track, like is done in the standard reconstruction, the direction of most of the events is reconstructed well, including events with low energies. In the following, the same reconstruction procedure is used in which the zenith angle and azimuthal angle are not reconstructed, but are fixed to different directions. The quality cut of the standard reconstruction procedure will be replaced by a selection based on these results.

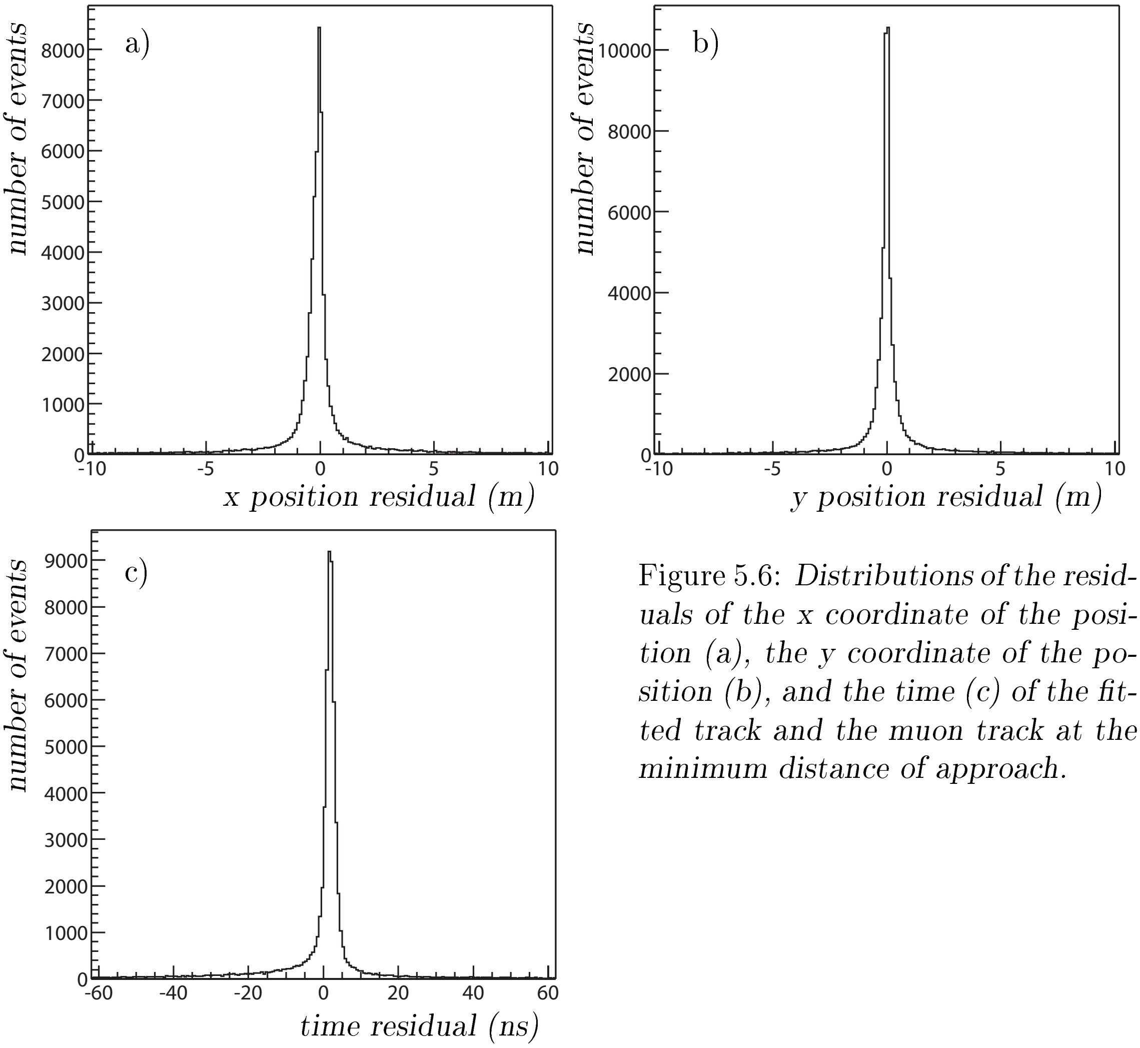

Figure 5.6: *Distributions of the residuals of the x coordinate of the position (a), the y coordinate of the position (b), and the time (c) of the fitted track and the muon track at the minimum distance of approach.*

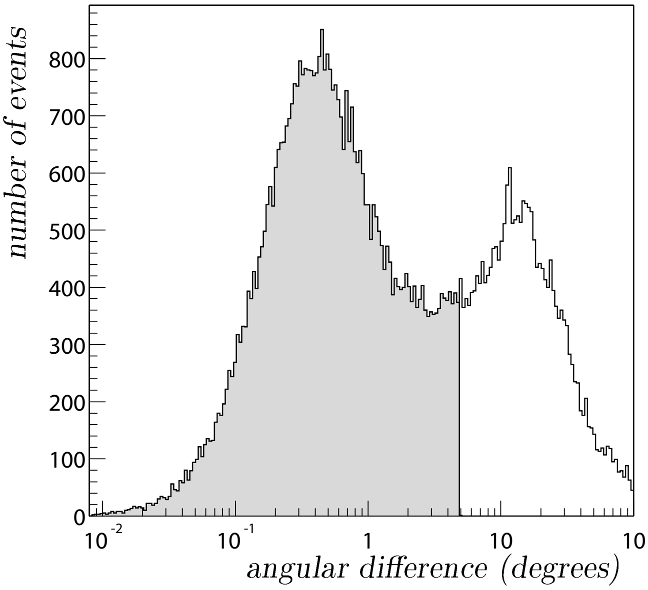

Figure 5.7: *The distribution of the difference between the direction of the fitted track and the neutrino. The shaded area shows the events for which this difference is less than 5°.*

5.3 Likelihood distributions

For the analysis of GRB data a quantity is defined that is a measure for the compatibility of the data in an event with a neutrino from a GRB. For this, the detected muon is assumed to come from the same direction as the neutrino. Each event is reconstructed with the described fitting procedures, where the zenith angle and azimuthal angle are not reconstructed, but are fixed to an assumed direction. The ratio of the logarithm of the likelihood values for the hypothesis that the event consists of random background hits and signal hits from a muon in the direction of the GRB (H_1), and the hypothesis that the event consists of only random background hits (H_0) is calculated. For the H_1 hypothesis the likelihood value (L in equation 5.3) is calculated using the PDFs described in the previous section. For the H_0 hypothesis it is calculated using only the baselines of these PDFs. The logarithm of the likelihood ratio $\Lambda_1 - \Lambda_0$[†] indicates the compatibility of the event with a muon signal in addition to random background for the assumed direction.

Subsequently, each of these events is reconstructed in the same way assuming 170 other directions than the GRB direction, where all these directions are either opposite to the assumed direction, or downgoing directions. The number of trials is a compromise between execution speed and the coverage of the corresponding solid angle. The likelihood value for each of these directions is calculated in the same way, where the quantity $\Lambda_1 - \Lambda_0$ indicates the compatibility of the event with a neutrino from that direction. The result found with the direction that has the largest likelihood is compared with the result found with the preferred direction. The final result is defined as the difference between the value of $\Lambda_1 - \Lambda_0$ for the preferred direction and the largest value of $\Lambda_1 - \Lambda_0$ for the other directions. The difference of these two values, $(\Lambda_1 - \Lambda_0)_{\text{preferred}} - (\Lambda_1 - \Lambda_0)_{\text{other}}$, is a measure for the compatibility of the event with a neutrino from the direction of the GRB. For signal events this difference should have a large positive value. In case of random background it should have a negative value, or a value close to zero.

The distribution of the quantity $(\Lambda_1 - \Lambda_0)_{\text{preferred}} - (\Lambda_1 - \Lambda_0)_{\text{other}}$, hereafter Λ^*, of simulated events found in 4 minutes of data taken during GRB 030329 is shown in figure 5.8. The period of 4 minutes is within the capabilities of the special data taking during a GRB, and is based on the typical GRB durations and the expected arrival time of the neutrinos (see section 4.3). The different distributions in the figure represent the three different types of background and an assumed neutrino signal from this GRB.

The atmospheric muon and neutrino contributions are weighted with their corresponding fluxes given in section 2.9. Although the direction of the downgoing atmospheric muons is very different from the direction of the neutrinos from the GRB, still some of them show positive values of Λ^*. Most of them however show negative values. This is achieved by choosing part of the different directions used in

---

[†] $\log \frac{L_1}{L_0} \equiv \Lambda_1 - \Lambda_0$, where $\Lambda_1 = \log L_1$ and $\Lambda_0 = \log L_0$

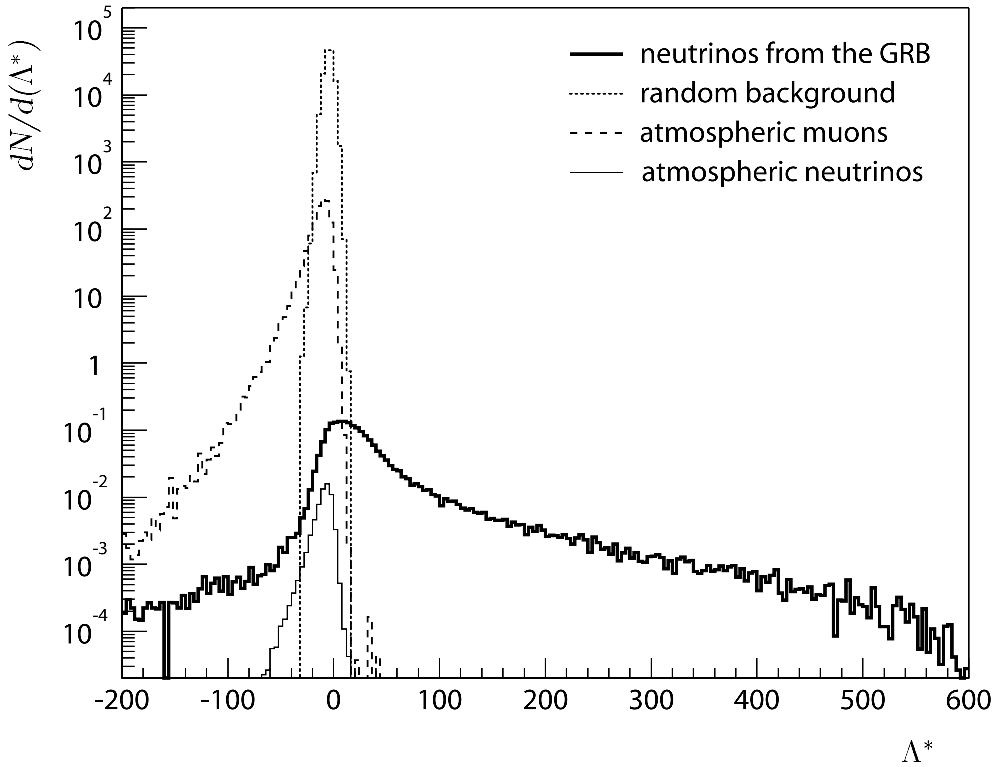

Figure 5.8: *The distribution of the quantity Λ^* of simulated events found in 4 minutes of data taken during GRB 030329.*

the reconstruction as downgoing directions, expecting that atmospheric muon events will be reconstructed better using one of these directions than using the preferred direction. For the same reason, to suppress the contribution from atmospheric neutrinos, the other different directions are chosen opposite to the neutrino direction. The atmospheric neutrinos that come from the same direction as the neutrinos from the GRB have positive values for the Λ^* quantity like they should. As only a few atmospheric neutrinos come from the GRB direction within the 4 minutes of data taking, most atmospheric neutrinos have negative values. The random background events have small values of Λ^*, most of them negative.

The contribution from the neutrinos from the GRB is weighted with the shape of the sum of the fluxes shown in figure 1.5. The assumed neutrino signal from this GRB corresponds to a flux providing 10 neutrino interactions near the detector during the 4 minutes of data taking, of which the resulting muons produce at least 6 hits in the detector. These muons should in principle be found by the FlashBack filter, but in practice the filter efficiency is about 80% (see figure 4.9). The signal shows a significant contribution at large positive values of Λ^*, as most of the neutrino signal is well reconstructed in the direction of the GRB.

The number of reconstructed background events due to atmospheric muons and atmospheric neutrinos in the figure do not correspond exactly with the numbers given in table 4.2. In this analysis the random background hits that were recorded at the same time as the events are taken into account, which is not the case for the numbers given previously. In this way also events will be found that are a combination of random background hits, and hits caused by an atmospheric muon or atmospheric neutrino event. Consequently a few events (less than 10%) that consist of only random background hits are classified as atmospheric background. This is not corrected for.

As can be seen from figure 5.8, the Λ^* quantity clearly differentiates between signal (positive values) and background.

5.4 Reconstruction efficiency

The analysis method described in this chapter improves the results of the reconstruction of GRB data compared to the standard reconstruction (see section 5.1). When the direction of the neutrinos is not fixed, and the zenith angle and azimuthal angle are reconstructed, 70% of the events are found within 5° from the original neutrino direction. For the standard reconstruction this is 20%, including the quality cut. When the direction of the detected muons is not reconstructed, and the information on the location of the GRB from the IBAS or GCN warning systems is used explicitly, an event selection can be introduced in the analysis method such that almost all background is suppressed.

The quantity introduced in section 5.3 is a measure for the quality of the reconstructed events. All events for which this quantity has a negative value can directly be considered as background events. By defining this norm, not just the background is reduced but also a number of signal events is lost. About 80% of the events from the GRB source are accepted. The background is reduced by 90%.

To obtain an almost background free data set, the remaining background at small positive values needs to be reduced further. Just like in the standard reconstruction, an extra cut is applied to the reconstructed events to reject most of the remaining background. This cut is based on the value of the Λ^* quantity, and could in principle depend on the number of hits in the cluster. In figure 5.9 the distribution of the Λ^* quantity is shown as a function of the cluster size of the events. The same data set is used as that for figure 5.8. The three types of background are now taken together. The ranges of the cluster sizes are chosen such that each histogram contains about 1 signal event. At small cluster sizes (less than 20 hits) the background is dominated by the random background. Events found in random data have in general small cluster sizes. Towards bigger cluster sizes the background is dominated by atmospheric muons. The atmospheric neutrino background is very small compared to the atmospheric muon background. All background shows in general negative values for the Λ^* quantity, independent of the cluster size. Apparently the value of the Λ^* quantity for background events never shifts to large positive values. The

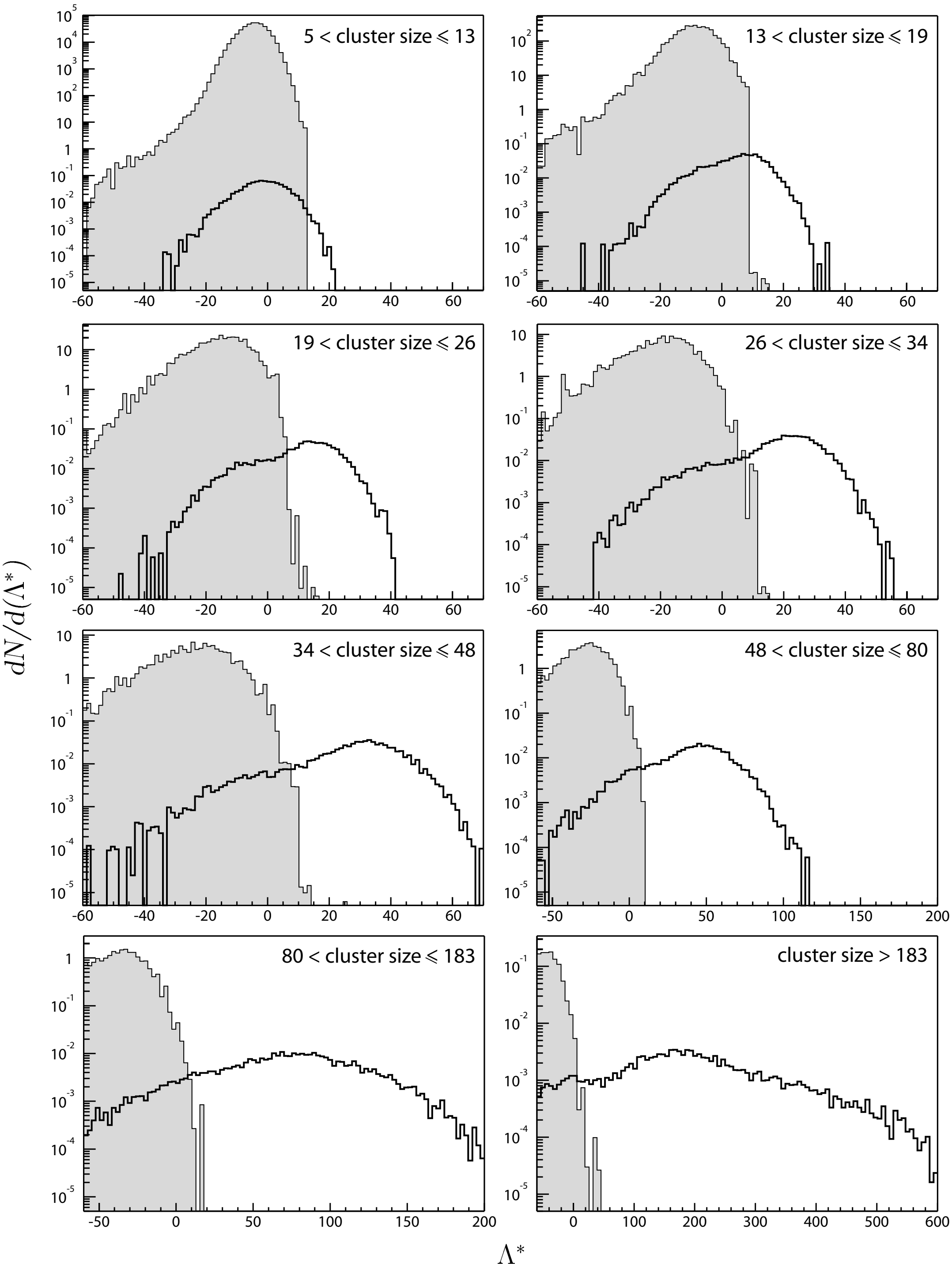

Figure 5.9: *Distribution of the quantity Λ^* for the events shown in figure 5.8 for different cluster sizes. The shaded area shows the total contribution of the background, the solid line corresponds to the signal events. Each histogram contains about 1 signal event.*

atmospheric neutrinos that come from the same direction as the neutrinos from the GRB do show large positive values for the Λ^* quantity, but their contribution is negligible within the 4 minutes of data taking during the GRB. The value of the Λ^* quantity for signal events moves to larger positive values as the cluster size of the events increases. For small cluster sizes only a small part of the signal can be distinguished from the background.

The introduced quantity $\Lambda_1 - \Lambda_0$ is a good way to define the probability of a neutrino event from a specific direction. By first considering the event as random background, and subsequently as a muon event with additional random background, the difference in the likelihood of both these cases includes explicitly the presence of random background. The difference of this quantity for a given direction and that for another direction, Λ^*, shows directly the compatibility of the events found with a neutrino from the given GRB.

Chapter 6

Results

Because of the transient nature of a GRB event, and because each GRB is unique, each burst is analysed separately. The FlashBack filter, used for data taken during a GRB (see chapter 4), and the special GRB reconstruction program (see chapter 5) are tuned according to the situation during the special data taking. Because of the short duration of a GRB, a single timing and position calibration of the detector can be applied to the data taken during the burst. The direction in the ANTARES reference frame of the incident neutrinos does not change significantly within this period, so the direction that is assumed in the filter and reconstruction algorithms can also be kept the same. When the actual duration of the GRB is known, it can be decided to split up the data taken during the GRB (that typically cover 4 minutes) into smaller fragments to obtain a better signal to background ratio.

The main quantity Λ^*, provided by the GRB reconstruction method (see section 5.3), enables the separation of the background from the signal. To completely separate the background from the signal a final cut is introduced. This cut is determined by the Λ^* distribution of the background, and is applied to all events.

The final cut is determined for each burst separately, and depends mainly on the location of the GRB and its duration. To verify that no background event survives the cut, the same procedure is carried out using high statistics obtained with random triggers. The events that remain after the final cut can then be interpreted as a discovery of a neutrino signal from a GRB. Other methods aimed at finding point sources with ANTARES require a minimum number of events after a certain number of years to claim a discovery. With the method developed and described in this work a discovery can be made on the basis of a single GRB. Using published predictions of neutrino fluxes from GRBs, the detection of a neutrino from a GRB is possible within a year of operation as there are hundreds of GRBs detected by satellites each year.

The methods can also be applied to other point sources for which the location is known, and that are permanent, or are active during a long period compared to the typical GRB duration. This can be achieved with minor changes in the data filter procedure. This offers good prospects for studying these sources, although the discovery potential will be lower compared to that for GRBs as the contribution from atmospheric neutrinos will be higher.

6.1 Event selection

For events with large cluster sizes (events that contain many triggered hits) the distribution of the value of the Λ^* quantity shows a clear distinction between background and signal (see figure 5.9). In the distributions for events with small cluster sizes the contribution from the signal is largely dominated by the contribution from random background. The average value of the Λ^* quantity for signal events increases with the cluster size, while the average value for background events stays approximately the same. The value of this quantity tells roughly if an event can be considered as background (negative values) or as signal (positive values). Even when this selection is made, still some background events remain. To reject the remaining background events, a final cut is introduced that is applied to each of the reconstructed events. This cut involves a minimum value of the Λ^* quantity, and depends on the cluster size of the event. The value of this cut is chosen such that the probability that one or more background events remain in a data sample covering 4 minutes is smaller than 2.7×10^{-3} or 5.7×10^{-7}, which correspond to the 3σ and 5σ background levels respectively. In order to keep the probability for one or more background events independent of the cluster size, the value of this cut differs for the different cluster size ranges. With the assumed flux each cluster size bin contains about the same number of signal events. For each of the eight cluster size bins in figure 5.9 the corresponding probability is set to one eighth of that of the 3σ and 5σ levels. Events for which the value of the Λ^* quantity is larger than this minimum value are accepted. As a result of the cut, part of the signal is lost. The fraction of the signal that is accepted as a function of the cut value is shown in figure 6.1 for different cluster size ranges. For small cluster sizes the background is hardly separated from the signal. Therefore the efficiency for small cluster sizes is low (1–5%). The efficiency increases with the cluster size to about 80%. At the 3σ level no random background is left. For small cluster sizes the 3σ and 5σ levels are close together because of the steep drop of the Λ^* distributions of the random background. At the 5σ level only background from atmospheric neutrinos remains. As only very few atmospheric neutrinos come from the same direction as the GRB during the 4 minutes of special data taking around the time of the burst, the contribution of this background is very low.

6.2 Efficiency

In the different stages of the data processing and analysis, from the detection of the Cherenkov light to the final cut after the reconstruction of the physics events, a number of signal events is lost. To quantify this inefficiency, the special data taking

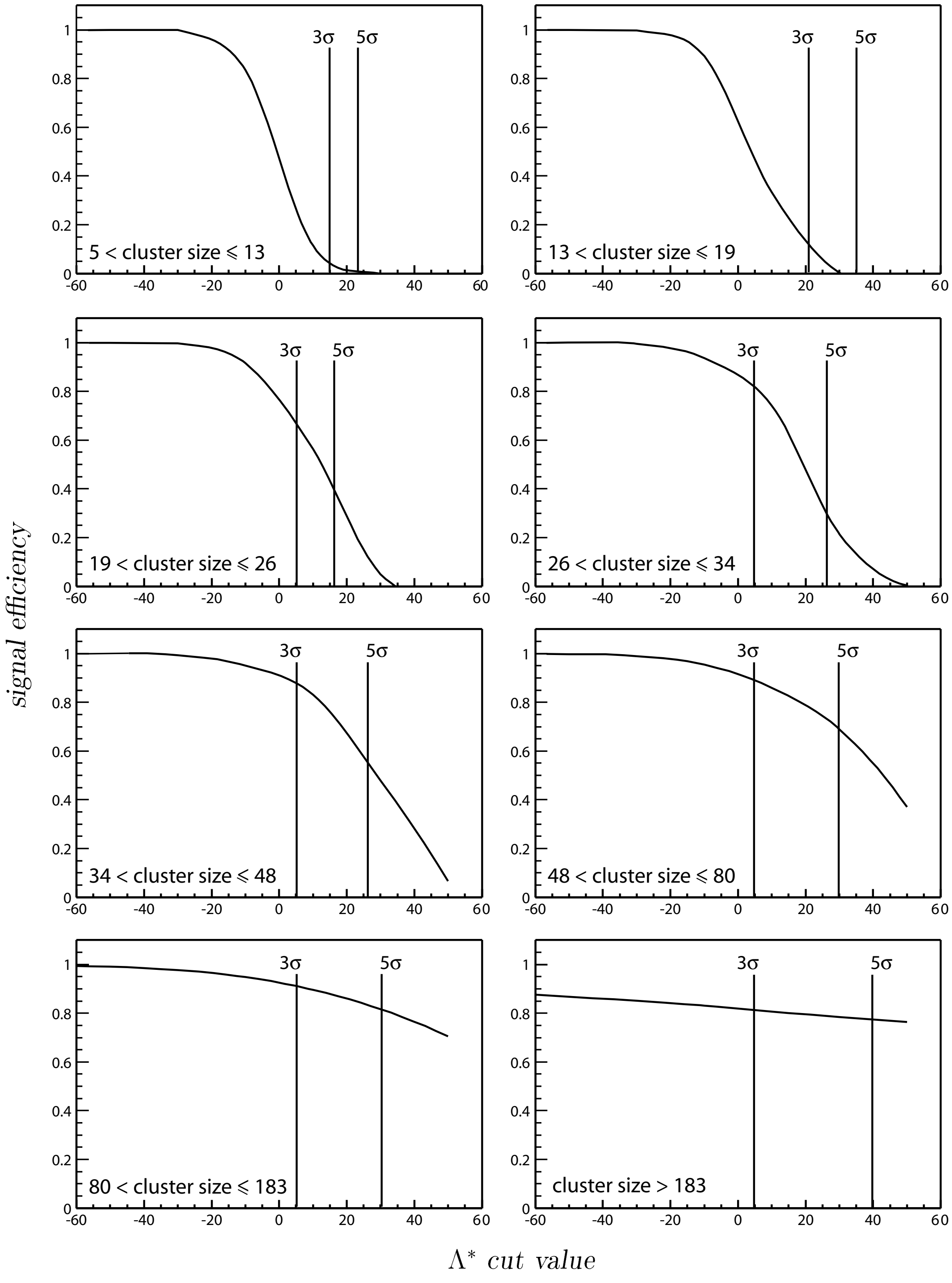

Figure 6.1: *The signal efficiency as a function of the cut value on the* Λ^* *quantity for different cluster size ranges. Also indicated are the values for which the probability that one or more background events remain in the entire data sample covering 4 minutes is smaller than* 2.7×10^{-3} *(*3σ*) and* 5.7×10^{-7} *(*5σ*).*

described in section 4.3, the data filtering with FlashBack described in section 4.4, and the GRB data analysis described in section 5.3 were simulated for GRB 030329. The reduction of the number of signal events in the different stages is shown in figure 6.2 as a function of the neutrino energy. The neutrino signal is weighted with

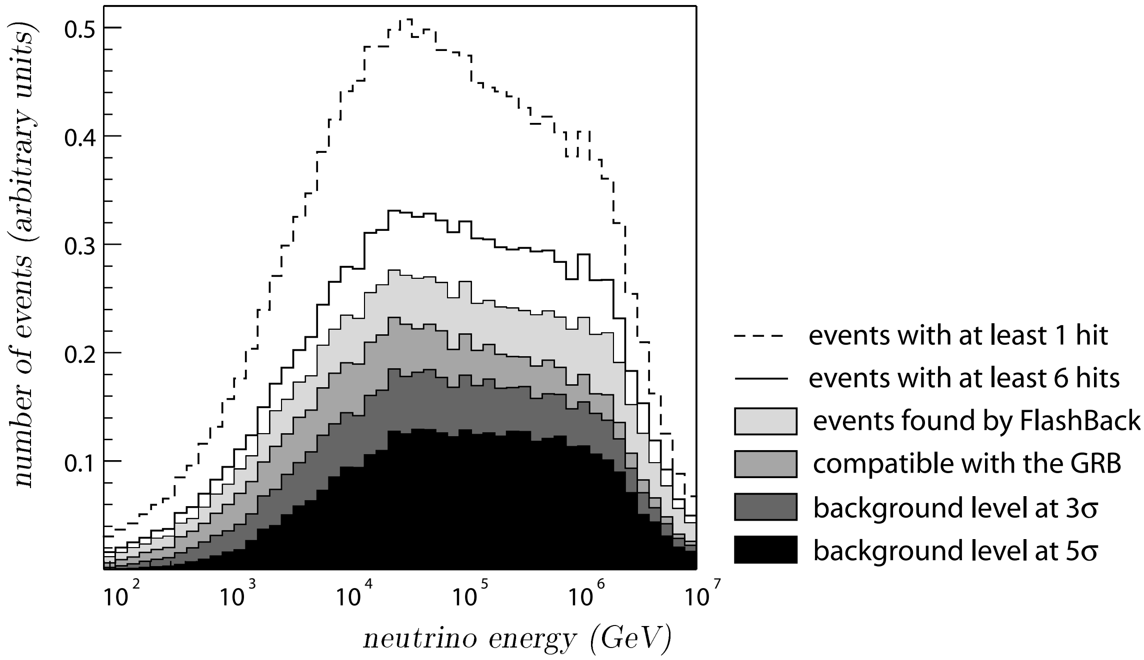

Figure 6.2: *The reduction of the number of signal events from GRB 030329 as a function of the neutrino energy after the different stages of the data filtering and analysis processes, from the detection of the Cherenkov light to an almost background free data sample. The special data taking was used in the simulation, i.e. the data were processed with FlashBack and analysed with the GRB reconstruction.*

the shape of the sum of the neutrino fluxes shown in figure 1.5. Events that cause at least one hit in the detector are in principle detectable. Their distribution is indicated in the figure by the dashed line. Events that cause at least 6 hits in the detector could in principle be found by FlashBack. A minimum of 6 correlated hits is required by the FlashBack filter to find a physics event. Due to the additional requirements in the FlashBack filter (see section 4.4), and effects like scattering of the light (see section 2.8), 82% of the signal events are actually found. The events are reconstructed with the special reconstruction method for GRB data. In this method each event is reconstructed many times, each time assuming a different direction. For each direction the $\Lambda_1 - \Lambda_0$ quantity is calculated, which is a measure for the compatibility of the event with a neutrino from that direction (see section 5.3). For 80% of the reconstructed events this quantity is largest for the direction of the GRB. These events are considered compatible with the GRB. After the final cut that reduces the probability of having one or more events due to background to the

3σ (5σ) level in the entire data sample, 80% (55%) of these events are accepted. This amounts to a total efficiency of 52% (35%) for this specific GRB, from the detection of 6 or more Cherenkov photons to a 3σ (5σ) background free event sample. The efficiency is different for each burst as is described in section 6.4.

The size of a neutrino telescope can be expressed in terms of its effective volume, given in equation 2.5. The effective volume is defined as the volume in which a neutrino interaction produces a detectable muon. In figure 6.3 the effective volumes are shown for the different stages in the data processing and analysis as a function of the neutrino energy. In general the effective volume increases with the neutrino energy as the muon range increases with the energy. Also, the effective volume is much bigger than the instrumented volume of 0.02 km^3 as high energy muons from interactions that took place far from the detector are still detectable. During the data processing and analysis the effective volume decreases as in each step some events are lost. At very high energies the effective volume exceeds one cubic kilometre.

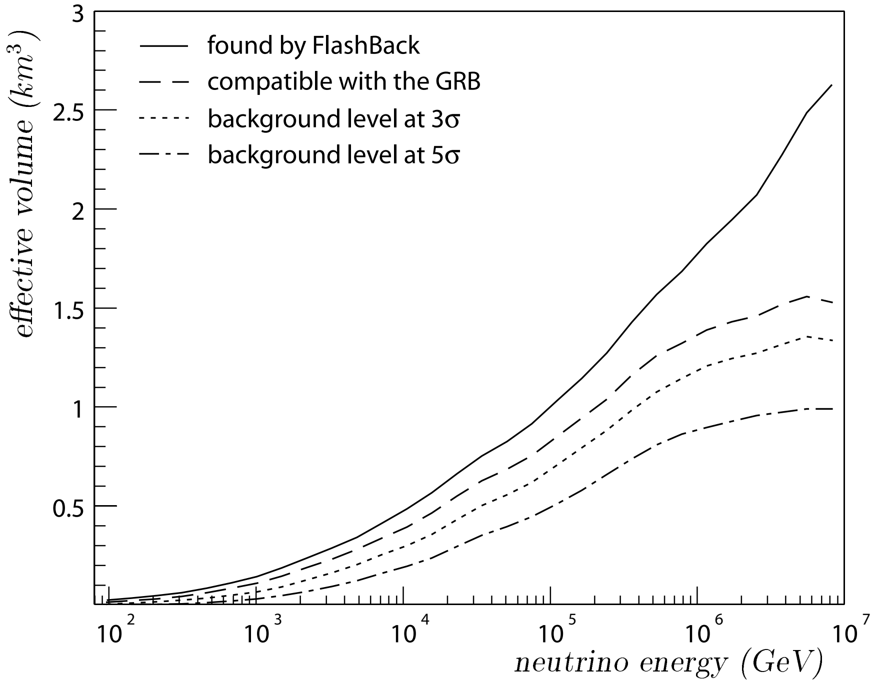

Figure 6.3: *Effective volumes for neutrinos from GRB 030329 for the different stages in the data processing and analysis.*

6.3 Comparison with standard methods

The reduction of the signal after the different stages of the data processing and analysis when the standard methods for data taking, data filtering, and data analysis are applied, is shown in figure 6.4 as a function of the neutrino energy. Again the situation during GRB 030329 was simulated, and the same shape of the neutrino flux was assumed for the signal events. When during a GRB the data taking went

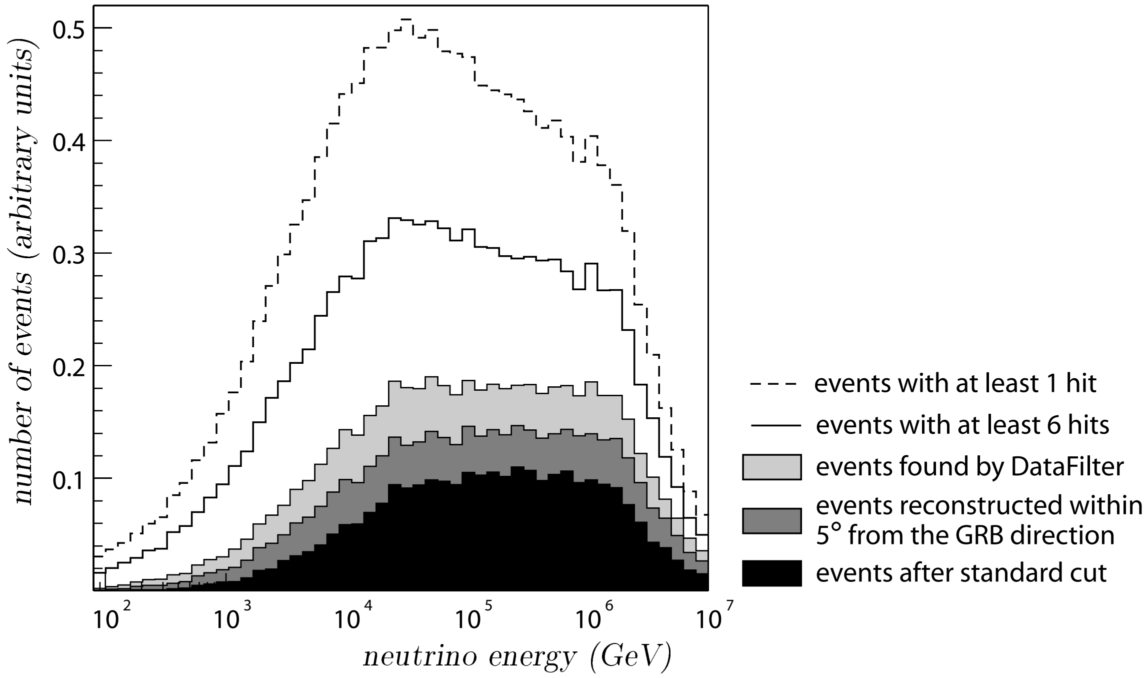

Figure 6.4: *The reduction of the number of signal events from GRB 030329 as a function of the neutrino energy after the different stages in the data processing and analysis when the standard methods are applied.*

the normal way, and the data were filtered online using the DataFilter program, the efficiency is about 55% as was already shown in section 4.6. After analysis with the standard reconstruction, 74% of the events found are reconstructed within 5° from the neutrino direction. This can be compared with the number of events that is considered compatible with a neutrino from the direction of the GRB in the special GRB analysis method. When the cut of the standard reconstruction is applied to these events, 66% of the events remain. After this cut the background that remains in the data sample covering 4 minutes is reduced to about the 3σ level. The total efficiency of the standard methods is then 27%, from the detection of 6 or more Cherenkov photons to a 3σ background free event sample.

Figure 6.5 shows the effective volumes for events from the direction of GRB 030329 as a function of energy when the standard methods are applied. It shows the effective volumes after the different stages in the data processing and analysis procedures.

The efficiencies obtained with the special data taking in case of a satellite trigger, the processing of the data with FlashBack, and the analysis of the found events with the special GRB reconstruction method, are compared with the standard methods. The result, shown in figure 6.6, includes the difference in efficiency between the two filters FlashBack and DataFilter, and the special GRB reconstruction method and the standard reconstruction method, including the effect of applying the correspond-

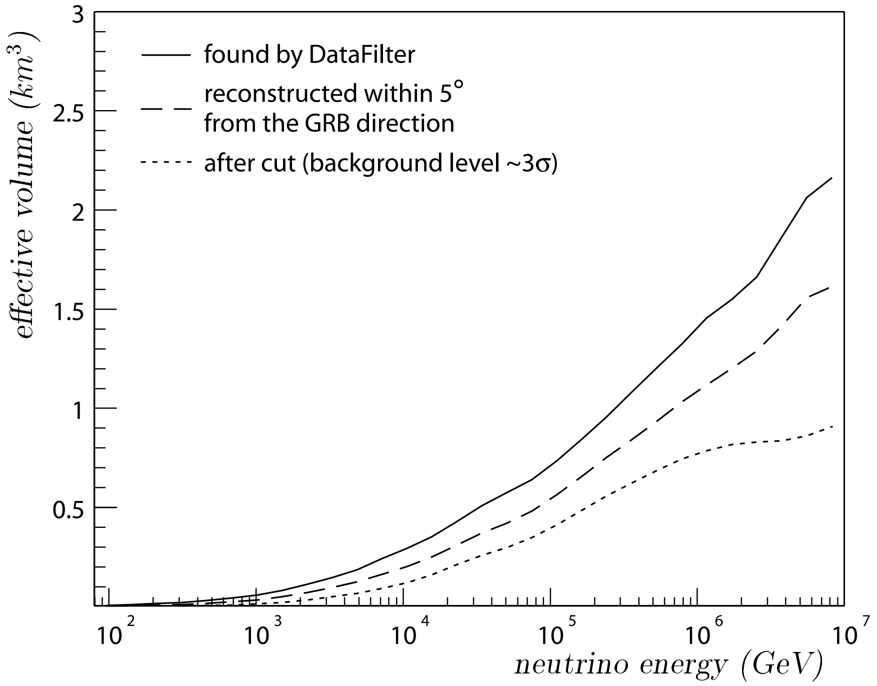

Figure 6.5: *Effective volumes for neutrinos from GRB 030329 for the different stages in the data processing and analysis when the standard methods are used.*

ing cuts. The efficiencies are relative to the number of events that cause at least 6 hits in the detector. The final cuts correspond to a 3σ probability for one or more background events in the data sample covering 4 minutes. The data processing and analysis method introduced in chapters 4 and 5 show a significantly larger efficiency compared to the standard methods, in particular at low neutrino energies. This improvement is due to the higher efficiency of FlashBack compared to DataFilter, and also to the better separation between signal and background of the special GRB analysis method compared to the standard method.

The ratio of the effective volumes of the two methods for neutrinos from GRB 030329 is shown in figure 6.7. The results obtained after special data taking during a GRB, filtering with FlashBack, and reconstruction with the special GRB analysis method, is shown relative to the result obtained with the standard data taking, standard filtering, and standard reconstruction method. From figures 6.6 and 6.7 it can be concluded that the efficiency of detecting neutrinos from GRBs is greatly improved using the satellite trigger.

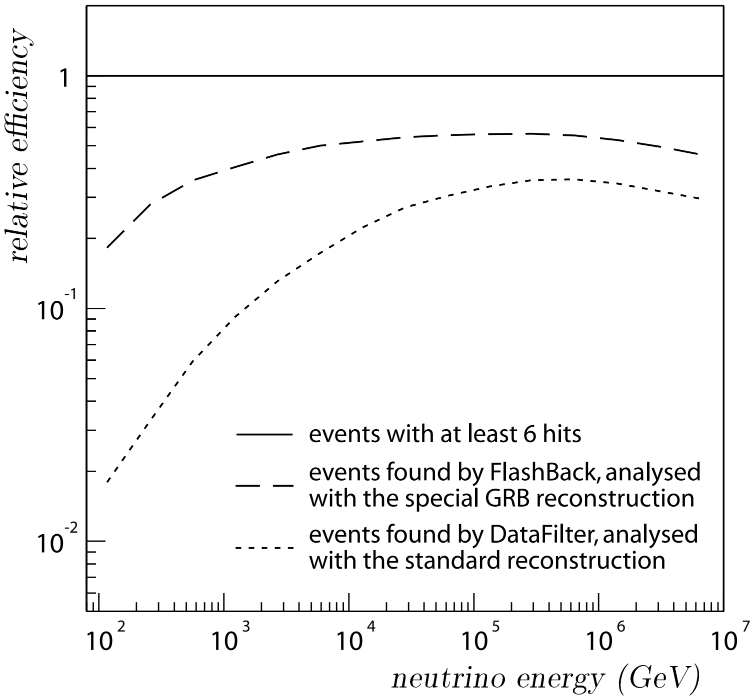

Figure 6.6: *The detection efficiencies of the two different methods for neutrinos from GRB 030329 with respect to the number of events that produce at least six hits in the detector as a function of the neutrino energy.*

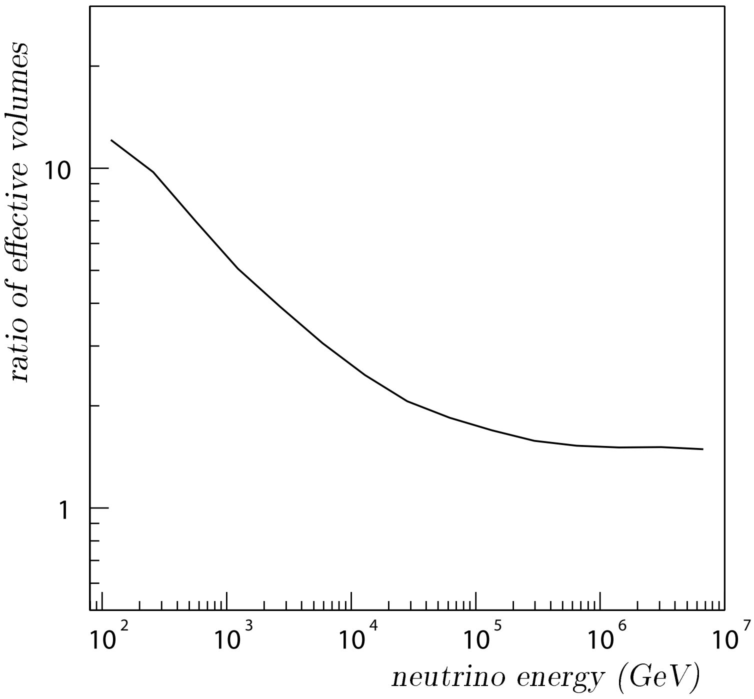

Figure 6.7: *The ratio of the effective volumes obtained with the special GRB reconstruction method relative to the standard reconstruction method.*

6.4 Analysis per GRB

Each GRB is unique, and during each GRB the situation of the detector and the surrounding medium can be different. As the special data taking period is a snapshot of the situation, the filter and reconstruction processes can be adjusted to achieve the highest possible efficiency for each GRB separately.

6.4.1 Optimisation per GRB

The random background rate depends mainly on the activity of bioluminescence in the seawater. Up to now a constant singles rate of 70 kHz was assumed. However, the data that were taken with the prototype detector showed big fluctuations in the singles rate, and varied between 50 and 300 kHz over a period of three months (see section 2.9). According to the measured singles rate during a GRB, the settings in the filter program can be adjusted to obtain the highest efficiency for the signal, and at the same time keep the background event rate to an acceptable level.

Due to the currents in the seawater, the positions of the PMTs and the shape of the detector strings can change. The relative positions of the PMTs are measured regularly with the position calibration system (see section 2.6). These positions are crucial for the cluster algorithm to find correlations in the data, and for the reconstruction algorithm to obtain the desired angular resolution. During standard, continuous, data taking the changes in the measured positions have to be taken into account online in the filter algorithm. It is not likely that the positions will change significantly within the period of special data taking during a GRB. It will be sufficient to measure the positions of the PMTs at the time of the GRB, and these positions can be kept the same in the filter and reconstruction algorithms of the described methods for the entire data set. The calibration procedure can be triggered by the same satellite message that triggers the special data taking. The change in the relative time offsets of the PMTs will not be a problem either. These are expected to be stable for a period of several hours.

6.4.2 Directional dependence

The sensitivity for a GRB not only depends on the random background, but also on the GRB coordinates, mainly its declination. The FlashBack program already partly takes the dependence on the direction into account by setting a maximum transverse distance between PMTs depending on the direction of the neutrinos (see section 4.4). This constraint, and the orientation of the PMTs within a storey, makes the FlashBack filter more efficient for some directions than others. The directional dependence manifests itself further in the reconstruction. Up to now only GRB 030329 was considered in the analysis, and the cuts introduced in section 6.1 are based on this specific burst. Three other bursts, namely GRB 030101, GRB 041006, and GRB 040511, have been analysed. Together with the burst GRB 030329, these four GRBs are representative to test the directional dependence of the methods described as they were all below the horizon of the ANTARES detector, and the directions of the neutrinos from these sources in the ANTARES reference frame are sufficiently separated from each other.

Although the background from atmospheric muons increases for more horizontal directions (see table 4.2), the corresponding distribution of the Λ^* value is similar for all GRBs. For each of the GRBs the cut values were determined for the 3σ and 5σ background levels for a data sample covering 4 minutes of data taking. As the background and signal events show similar Λ^* distributions, these values are only slightly different for the four GRBs. Figure 6.8 shows the effective volumes for the four GRBs as a function of the neutrino energy. The smaller effective volume for horizontal directions is mainly due to the geometry of the detector (see section 4.6).

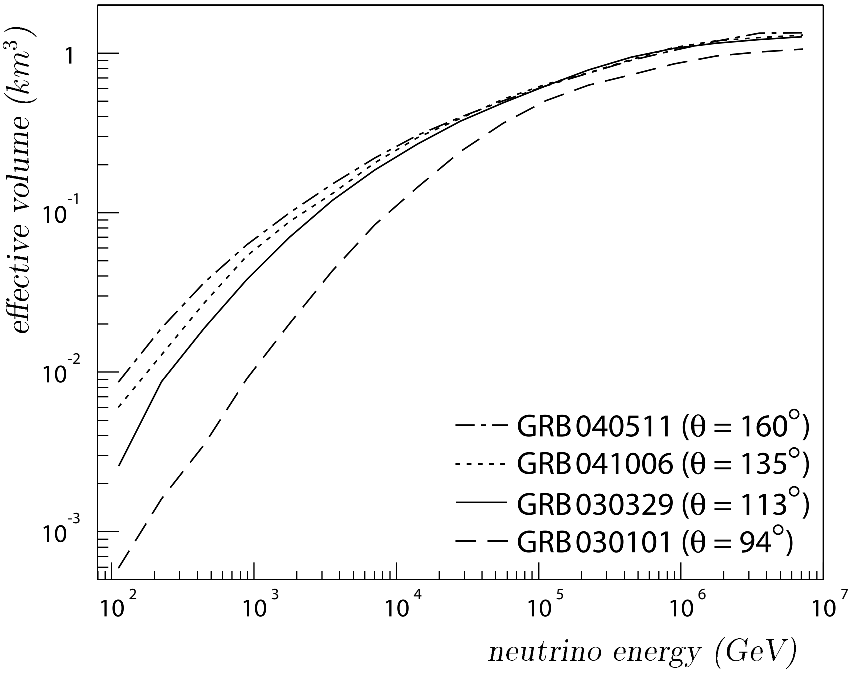

Figure 6.8: *Effective volumes for four GRBs as a function of the neutrino energy. The background level is at 3σ for a data sample covering 4 minutes. The different directions indicate the angle between the GRB direction and the zenith.*

The sensitivity of the detector to a neutrino flux can also be expressed in terms of the neutrino effective area, given in equation 2.6. The effective area for the four GRBs is shown in figure 6.9 as a function of the neutrino energy. The background level is at 3σ for a data sample covering 4 minutes. For vertically upward directions the effective area decreases at high energies because the probability of transmission of a neutrino through the Earth decreases (see figure 2.11). This effect is not taken into account in the effective volumes shown in figure 6.8.

6.4.3 Burst duration

The durations of GRBs vary between a few milliseconds to a few hundreds of seconds (see figure 1.2). At the time of the detection of the first gamma rays by the satellite,

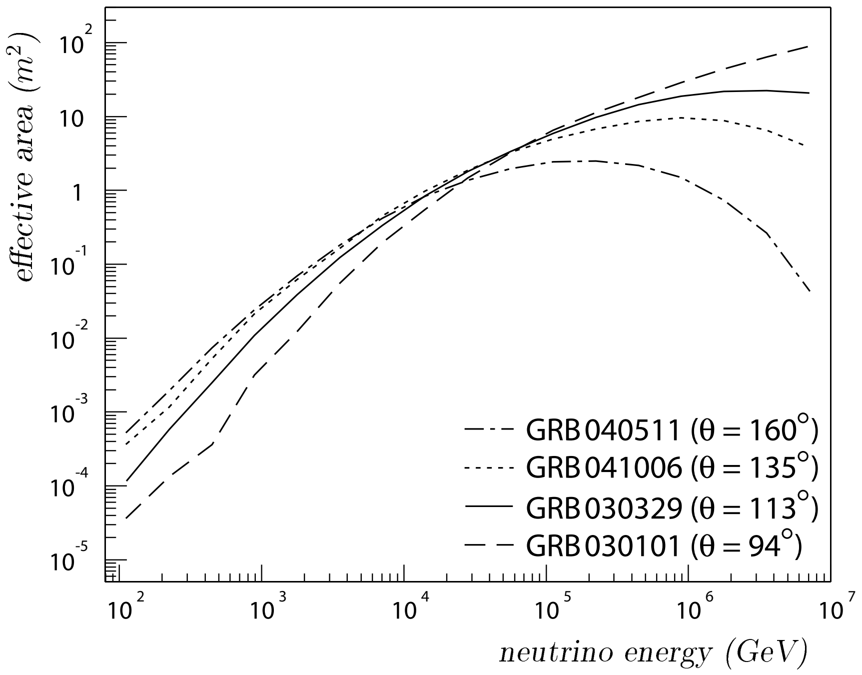

Figure 6.9: *Effective areas for four GRBs as a function of the neutrino energy. The background level is at 3σ for a data sample covering 4 minutes. The different directions indicate the angle between the GRB direction and the zenith.*

and the arrival of the alert message at the ANTARES site, this duration is not known yet. The duration of a GRB will be distributed later via the GCN Circulars (see section 1.4.1). In this work a duration of 30 seconds is taken as the typical burst duration. To cover some period before and after the time of the burst the special data taking will last for a few minutes. In the end, all data covering a period of about 4 minutes are used for the analysis. When afterwards the duration of the GRB appears to be very short, the data need not be analysed all together. The data could be split up in pieces with a duration corresponding to two or three times the burst duration. This would result in a better signal to background ratio. Only the data fragment will be accepted that covers completely the time during which the MeV gamma rays were detected. During the period covered by this data fragment also the neutrino signal is expected, as all processes that are assumed to produce neutrinos take place in coincidence with the gamma-ray production, or shortly before or after that (see section 1.3). The selection of a smaller data fragment could have been done for GRB 030329, which had a duration of 30 seconds. The background in each data fragment would have been reduced with a factor of 3–4. For a burst that lasted for 1 second, like GRB 030101, the background in each data fragment would be reduced by a factor of about 100.

The introduced cuts that define the 3σ and 5σ background levels are related to the period covered by the data fragment. The 3σ and 5σ background levels that were mentioned earlier are all for a data sample covering 4 minutes. All but one of the GRBs for which the effective volumes and neutrino effective areas were determined and shown in figures 6.8 and 6.9 had a duration of about 30 seconds. If for these

GRBs the data sample had indeed been split up into data fragments each covering a period of 90 seconds (three times the burst duration), the background in each data fragment would be reduced and the cut values could be adjusted. The neutrino effective areas then obtained are shown in figure 6.10 by a single solid line, relative to those obtained for a data sample covering 4 minutes. One of the four bursts, GRB 030101, had a duration of 1 second. Splitting up the data sample for this GRB into smaller fragments each covering 3 seconds (three times the burst duration) yields new cut values for the 3σ background level. The obtained neutrino effective area relative to the situation where the entire data sample was used is shown by the dashed line in the figure. For high energies ($E_\nu \geq 10^5$ GeV) the difference becomes smaller as the contribution from background is small. For lower energies the increase of the neutrino effective area is significant.

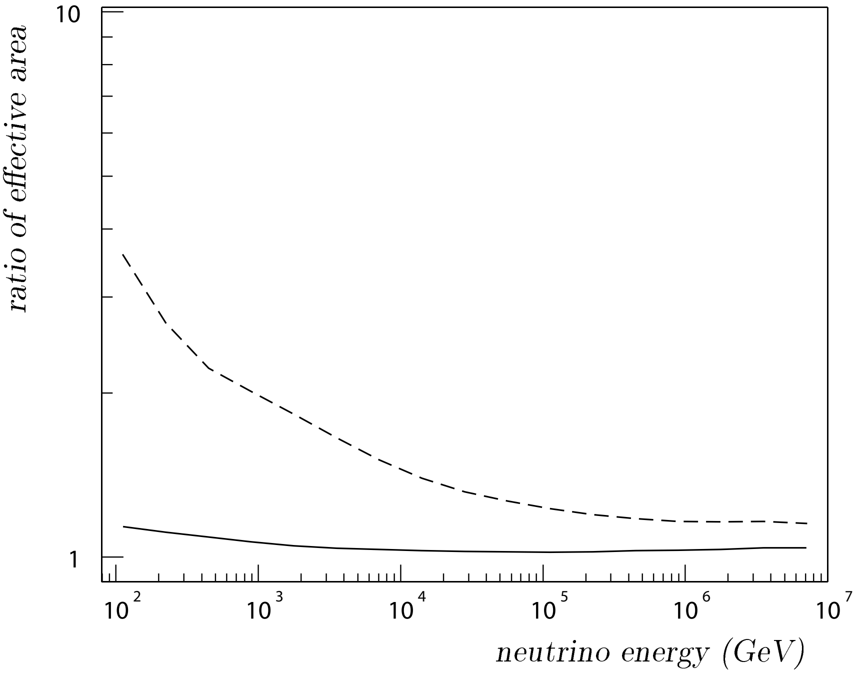

Figure 6.10: *Neutrino effective areas for data fragments covering 90 seconds (solid line) and 3 seconds (dashed line), relative to the neutrino effective area for a data fragment covering 4 minutes.*

The background level is thus not only related to the location of the GRB, but also to its duration. This should be kept in mind when calculating the event rate for a given burst. The presented effective volumes and neutrino effective areas in figures 6.8 and 6.9 are representative for GRBs with a duration of about 80 seconds, as three times this burst duration corresponds to the data sample covering 4 minutes. For GRBs with a duration shorter than 80 seconds these effective volumes and neutrino effective areas are underestimated. In the analysis of GRB data the knowledge of the duration of the burst is crucial, all the more since Swift is able to detect short GRBs, which produce a hard photon spectrum (see section 1.1). If the neutrino spectrum from short bursts is hard as well, the discovery potential for these bursts will increase significantly.

6.4.4 Random triggers

The analysis of the data with the methods described can be repeated many times on other data than the data taken during the GRB, as if there were again a GRB in exactly that direction. Data covering 4 minutes can be saved to disk at random times, and filtered and reconstructed assuming the same neutrino direction as that of the GRB at the time of the burst. Data will undoubtedly be saved to disk many times, as many alert messages are received while afterwards it appeared not to be a GRB. The distribution of false alert messages happened on average about once a day over the last 4 years. These data can also be considered as data taken at random times. By analysing these data as well, pretending a specific burst took place, the contribution of the background to the distribution of the Λ^* quantity can be measured. More statistics lead to more refined knowledge of the tail in the distribution of the background towards positive values of Λ^*. As a result, these measurements contribute to a more reliable determination of the value of the final cut. When the data samples from random triggers are compared with the data sample that was taken during the GRB, the net result could be a signal that does not appear in any of the data samples taken with a random trigger but shows up in the GRB data sample.

This exercise was done for GRB 030329. Background data corresponding to 4 minutes were filtered and analysed using the location of GRB 030329 at the time of the burst, but no neutrino events were added. This simulates the same situation as shown in figure 5.8, but at a different time. Figure 6.11 shows the result of the distributions of the Λ^* quantity of all data from both the snapshots. At negative and

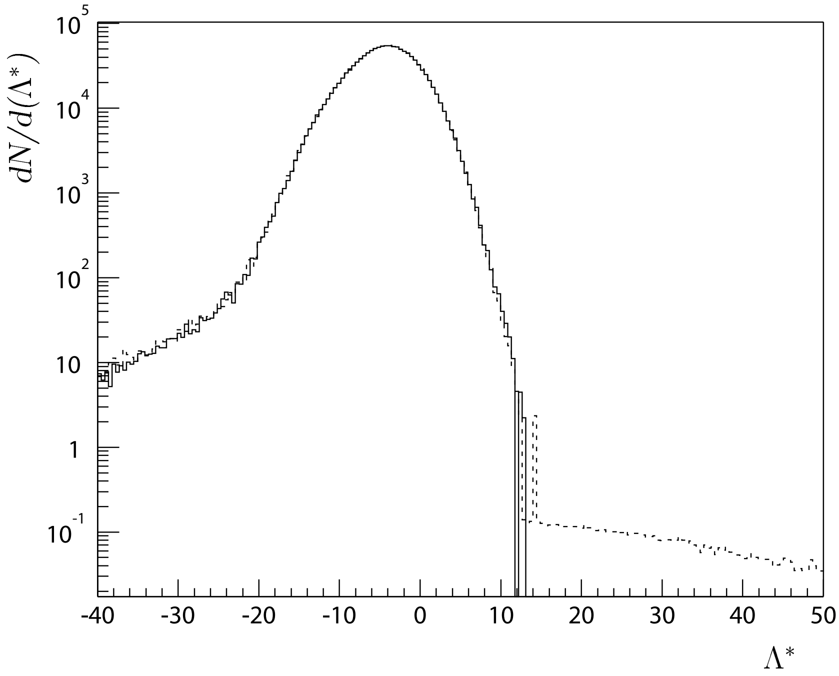

Figure 6.11: *The Λ^* distributions for two different data sets, both covering 4 minutes of data taking, filtered and analysed with the direction of GRB 030329 at the time of the burst. One of the data sets, indicated by the dashed line, includes a neutrino signal.*

small positive values of Λ^* the events are considered as background. As expected, the distributions from both data samples are similar in that range. Towards larger values of Λ^*, the contribution from the signal can be distinguished that is only present in one of the data samples. When the 3σ cut is applied to the value of the Λ^* quantity that was determined for this specific burst, the background is indeed rejected and the signal remains.

6.5 Field of view

The results of filtering the data with FlashBack, and after that analysing the events found with the special GRB reconstruction method are obtained assuming that the absolute orientation and position of the detector are known. In the filter and reconstruction algorithms the location of the GRB as it is provided by the satellite is taken as the direction of the neutrinos. If there were a systematic offset in the absolute orientation of the detector, the assumed direction used in the algorithms would differ from the true neutrino direction. This could result in an inefficiency of the methods that explicitly use the direction of the neutrinos. This inefficiency is quantified for the FlashBack filter as a function of the difference between the true neutrino direction and the assumed direction. For this, neutrinos covering all upward directions have been used. The result is shown in figure 6.12. The efficiency shown is relative to the efficiency obtained when the assumed direction is correct (at 0°). When the angle between the assumed direction and the true direction is increased more and more, the efficiency decreases slowly. At a difference of 90° the efficiency is still above 90%.

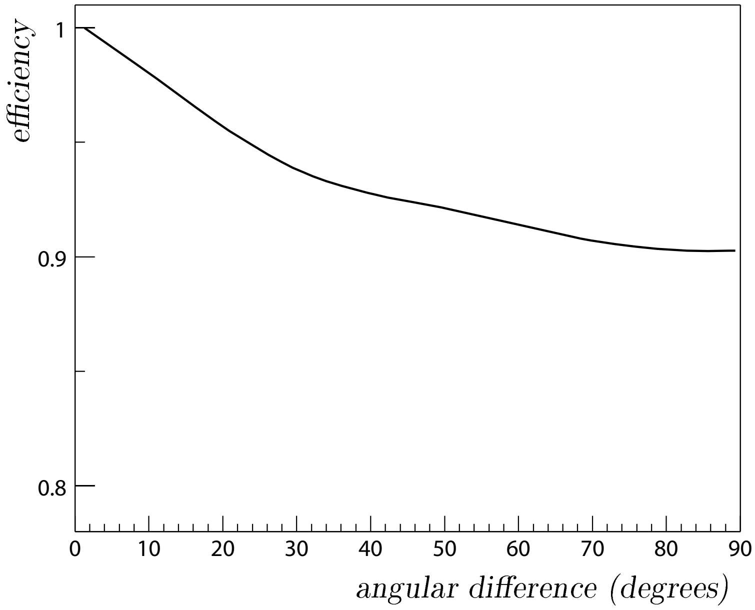

Figure 6.12: *Efficiency of the FlashBack filter as a function of the difference in angle between the true neutrino direction and the assumed direction for events in the energy range from* 10 *to* 10^5 *GeV.*

On top of the inefficiency of the filter process, signal might get lost in the reconstruction process when the chosen neutrino direction does not correspond with the GRB direction. In fact, the Λ^* quantity provided by the GRB reconstruction already indicates in a way how well the chosen neutrino direction corresponds with the GRB direction. After all, each event is reconstructed many times, each time using a different direction than the assumed neutrino direction (see section 5.3). For each direction the quantity $\Lambda_1 - \Lambda_0$ is calculated, which is a measure for the compatibility of the event with a neutrino from that direction. This value is maximal for the direction that is most compatible with the event. As it is assumed that the direction that is taken as the neutrino direction corresponds to the direction of neutrinos from the GRB with the specified location, it is expected that the value of $\Lambda_1 - \Lambda_0$ is largest for that direction. Therefore the Λ^* quantity should yield positive values for signal events, in which case it indicates that the assumed neutrino direction matches better with the event than any other direction. In case the assumed neutrino direction is taken incorrectly, the value of the $\Lambda_1 - \Lambda_0$ quantity should be larger for another direction than the assumed neutrino direction. Consequently the values of the Λ^* quantity will on average decrease. The effect of the decrease in the values of the Λ^* quantity with the increase in the angle between the true neutrino direction and the assumed neutrino direction is shown in figure 6.13. For angular differences of 8° and more, the average value of the Λ^* quantity drops below 0. As a consequence, most of the signal events will be identified as events from a different direction than the true neutrino direction.

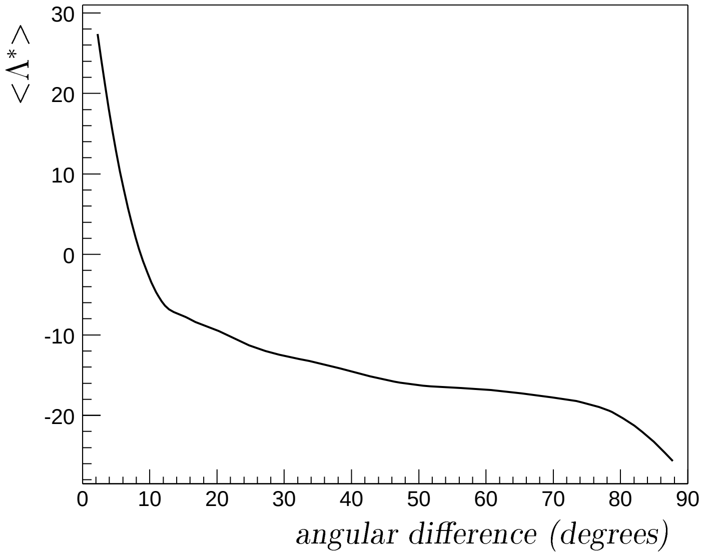

Figure 6.13: *Average value of the Λ^* quantity as a function of the angular difference between the GRB direction and the assumed neutrino direction.*

The first criterion in the event selection is to accept only the events that have a positive value for the Λ^* quantity. With this requirement part of the signal is rejected. The greater the angular difference between the assumed neutrino direction and the true neutrino direction becomes, the more signal events are rejected.

Figure 6.14 shows the signal efficiency as a function of the angle between the true neutrino direction and the assumed neutrino direction when applying this requirement to the events. As expected, the efficiency drops quickly when the angle becomes larger. This inefficiency is additional to the (minor) inefficiency in the filter process when looking in the wrong direction. When the angular difference is 6° or more, the efficiency drops below 50%. For an offset as big as this the prospect of detecting a neutrino from a GRB is reduced considerably.

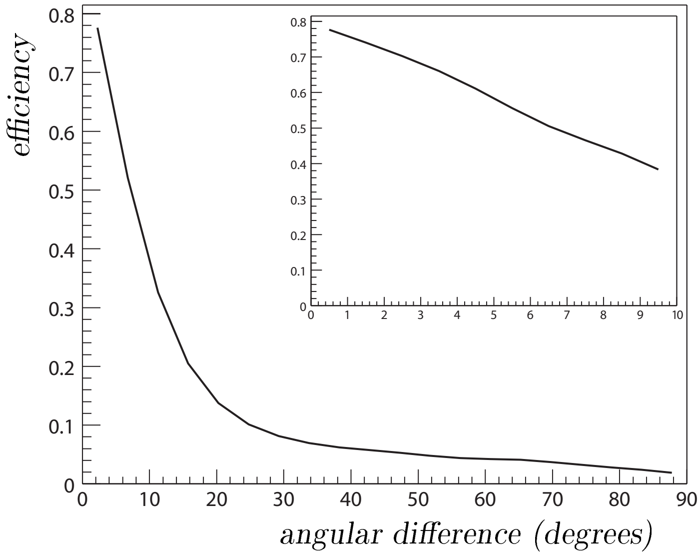

Figure 6.14: *Efficiency as a function of the difference in the angle between the true neutrino direction and the assumed neutrino direction. Only the events are selected that yield a positive value for the Λ^* quantity. The inset shows the same for small angular differences.*

When using the direction information in the filter and reconstruction algorithms, the detector is used as a telescope, looking for neutrinos from a specific direction. The field of view of this telescope is then about 6°. The detection of a neutrino from a GRB when the complete analysis is applied to the data taken during the GRB would to some extent indicate how well the absolute position of the detector is known. On the other hand, the special GRB reconstruction method can be repeated for different assumed directions until a possible neutrino signal is detected, using only the data that were taken during the short period. The loss of neutrino signal due to a systematic offset in the absolute orientation of the detector could then be recovered.

An alternative method to calibrate the orientation of the detector is based on the detection of the 'shadow' of the moon. This relies on the determination of the atmospheric muon flux from the direction of the moon and comparing it with that from any other point in the sky above the detector. Cosmic rays will be absorbed by the moon on their way to the Earth. Consequently a lower atmospheric muon flux is expected from the direction of the moon than from other directions. If a consistent deficit in atmospheric muon signal is observed when looking in the direction of the moon, the absolute orientation of the detector could be verified.

The error on the coordinates of the GRBs provided by the instruments on board the GRB satellites is smaller than 0.15° (see section 1.4). The refined positions that may be distributed later via the GRB warning systems have an error of the order of a few arcminutes. Such a deviation on the location of the GRB obviously has no effect on the efficiency of the described methods.

The location of a GRB is given in the equatorial coordinates right ascension and declination. These are converted into the zenith angle and azimuthal angle for the filter and reconstruction algorithms, using the geographical coordinates of the detector. The resulting angles depend on the universal time of the GRB. The direction to the GRB from the ANTARES site changes as time goes by. The declination of the source determines to what extent this direction changes. The data that are used for the analysis with the tools that depend on the direction of the GRB cover 4 minutes. During this period the source can move at most 1° away from the initial direction. The loss in efficiency due to this effect can be neglected, and all data can be analysed using the same direction at the time of the burst.

The difference in the direction between the incident neutrino and the resulting muon has an effect on the efficiency for neutrino energies below about 100 GeV (see figure 2.3). This effect is included in the analysis.

6.6 Applying the GRB analysis in other cases

It could happen that the location of a GRB comes out while during the burst no special data taking was triggered, for example when the alert message was missed, or when the GRB was not detected by one of the satellites that distribute alert messages. In this case the data were processed the standard way using DataFilter. As the time the GRB took place is known, as well as its location, these data could still be analysed using the special GRB reconstruction method to obtain a higher efficiency than when the standard reconstruction is used. Figure 6.15 shows the efficiency for signal events that were found by DataFilter and analysed with the special GRB analysis method as a function of the neutrino energy and relative to the efficiency obtained when the data were filtered using FlashBack. As expected this yields a lower efficiency for low-energy events as these will in general not be found by the DataFilter program.

Knowing that the GRB reconstruction yields a higher efficiency than the standard reconstruction, this method could just as well be used for other point sources for which the direction is known. It is even possible to use directional information at the filter level for persistent sources. But, as will be described in the following, these methods will never obtain an efficiency as high as the methods used for GRBs.

6.6.1 Non-transient sources

The special GRB analysis can be applied to other sources with known direction, that are also believed to emit neutrinos. For these sources the data will in principle be filtered the standard way. The detection efficiency will then be lower than when

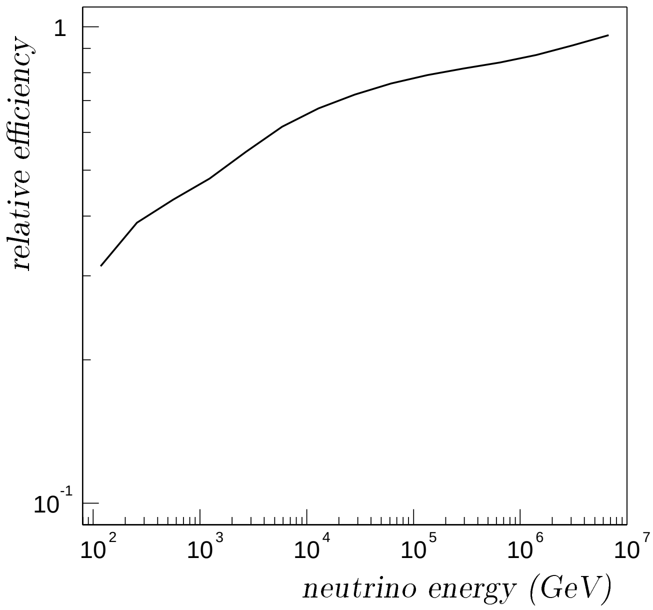

Figure 6.15: *Efficiency for signal events compatible with the GRB when using the special GRB analysis method on events found by DataFilter relative to the efficiency obtained when the data are filtered with FlashBack.*

the special data taking and filtering were applied, like in case of a GRB alert, but it still yields a higher efficiency than that obtained with the standard filter and reconstruction methods.

For most other neutrino sources it is not possible to apply the special data taking and filtering because of the high data rate. The fact that a GRB lasts for only a short time makes it possible to store all data that were taken during the event. These data can be processed within a reasonable time. But for other known sources, that are persistent or that can be observed during longer periods, the amount of data cannot be handled by FlashBack in the way it is done for GRBs.

The recent discoveries of TeV gamma rays from sources near the centre of the Galaxy [92] and supernova remnants [93, 94] suggest that these are a result of the acceleration mechanisms in these regions. The acceleration of protons could also result in the production of high-energy neutrinos. Another possible explanation for the production of TeV gamma rays in the centre of the Galaxy could be the presence of dark matter. Neutralinos, particles that are considered as dark matter candidates, are gathered in high concentrations in the centre of the Galaxy or the Sun. They can annihilate into two photons [95], and also into pairs of fermions or bosons, of which the decay products could include neutrinos [96]. Also microquasars are believed to emit neutrinos [97].

The special GRB reconstruction can be used to detect neutrinos from these sources, as their positions are known. However, the efficiency for neutrinos from these sources will never be as high as for GRBs, as atmospheric neutrinos start to play a more prominent role when looking for a source in the data covering a longer period. This does not apply to the data taken during a GRB, as these events last for a relatively short period.

6.6.2 Tracking sources

The direction of a source seen from the ANTARES site is determined by the coordinates of the source and the time of day. When the GRB reconstruction method is used for a continuous source or a source that can be observed during a long period in comparison with the duration of a GRB, the assumed neutrino direction has to be updated regularly. How often this should be done depends on the field of view of the detector. Figure 6.14 shows that for an angular difference of 1° between the direction set in the reconstruction algorithm and the location of the source the efficiency is still about 75%. It depends on the declination of the source how quickly it disappears from the field of view. However, the direction does not change by more than 1° within 4 minutes. When the neutrino direction is continuously updated to the new position of the source, at least every 4 minutes, the reconstruction efficiency remains 75% for this source. In this way sources can be tracked continuously.

If the principle of the FlashBack algorithm were applied to the filtering of the data for continuous sources, the efficiency could be increased even further. At present, FlashBack cannot be used for this because the filter requirements slow down the data processing too much. For continuous sources, the filtering process has to be done online, as is normally done with DataFilter. An increased filter efficiency for a specific source and an acceptable speed of the filter process can be achieved by using combinations of the requirements used in the FlashBack and DataFilter processes. The DataFilter program looks for correlated L1 hits (local coincidences), while the FlashBack program looks for correlated L0 hits (see section 4.4). To suppress the event rate due to the random background, the FlashBack filter requires at least one L1 hit for small clusters only. Whether a small cluster contains an L1 hit is checked after the correlations between the L0 hits were already found. The algorithm could just as well first look for an L1 hit, and then find correlated L0 hits. Filtering the data online requires at least one L1 hit in each cluster. Finding the correlations in the order described would speed up the filter process considerably as the L1 rate is typically 300 times less than the L0 rate. Other possibilities would be to relax the required number of L1 hits in the DataFilter process, or to apply the algorithm that uses the direction information to the L1 hits. A more detailed study is needed to obtain the optimal configuration for a data filter that filters the data online, meanwhile following a specific source, and at the same time yields a high efficiency. A preliminary study shows that about 100 2.8 GHz PCs are needed for every source. As in the case when using the GRB reconstruction method for continuous sources, the neutrino direction should be updated regularly with time. With such a data filter it would be possible to track a source on the filter level continuously.

6.7 Discovery potential

The detection of an event in the data taken during a GRB can be interpreted as a discovery. The background distribution for each burst can be measured with high statistics using the random triggers, described in section 6.4.4. This makes it possible to accurately determine the cut values for each burst separately, and to reliably reduce the background to the 3σ or 5σ levels. This means that the survival of one event can be interpreted as a discovery with the corresponding significance level. Such a discovery is then made with a single GRB. This distinguishes the methods described from other point source search methods, described in [83] and [98], where a discovery can be claimed when a minimum number of events is detected after a certain number of years. Because of the transient nature of a GRB, and the fact that each GRB is unique, the discovery potential is worked out for a single GRB.

The number of detectable events from GRB 030329 is calculated assuming the total neutrino flux shown in figure 1.5. The number of muons, produced by neutrinos from this GRB that penetrated the Earth, that cause at least one hit in the detector is 0.8. In this, the muon propagation through the water, the production and propagation of the Cherenkov light, and the detector response are included. About 0.5 muons from this GRB cause at least 6 hits in the detector. As was already stated in section 6.2, the efficiency from the detection of at least 6 hits to a 3σ background free event sample is 52%, and for a 5σ background free event sample 35%. This corresponds to the detection of 0.27 (0.19) events from this particular GRB for the 3σ (5σ) background level. This means that 34% (24%) of all muons resulting from neutrinos from this GRB that cause at least one hit in the detector are detected with a 3σ (5σ) background level. This includes the rejection of the 70 kHz rate per PMT due to random background, and the rejection of several hundreds of atmospheric muons per second that traverse the detector. This is a pessimistic estimation considering the fact that a higher significance level is achieved when the data sample covering 4 minutes of data taking is divided into smaller fragments according to the 30 second duration of this burst (see section 6.4.3).

Figure 6.16 shows the total estimated neutrino flux from GRB 030329 for the burst, supranova, and early afterglow components shown separately in figure 1.5. Also shown in this figure are the fluxes needed to detect at least one event from this specific GRB with a 90% (left) and 99% (right) confidence level, for both the 3σ and 5σ background levels for the entire data sample covering 4 minutes.

The estimated neutrino flux from GRB 030329 is not representative for most of the GRBs as this GRB was exceptionally nearby. To be able to give an idea of the discovery potential for neutrinos from an average GRB, a neutrino flux was estimated for a GRB with redshift 1 and a duration of 10 seconds. For such a burst the data sample can be split up into fragments covering 30 seconds each, three times the burst duration. The assumed flux has a typical E^{-2} spectrum and is indicated in figure 6.17 by the dashed line. Also shown are the required fluxes for the detection of one or more events with a 90% (left) and 99% (right) confidence level, for both

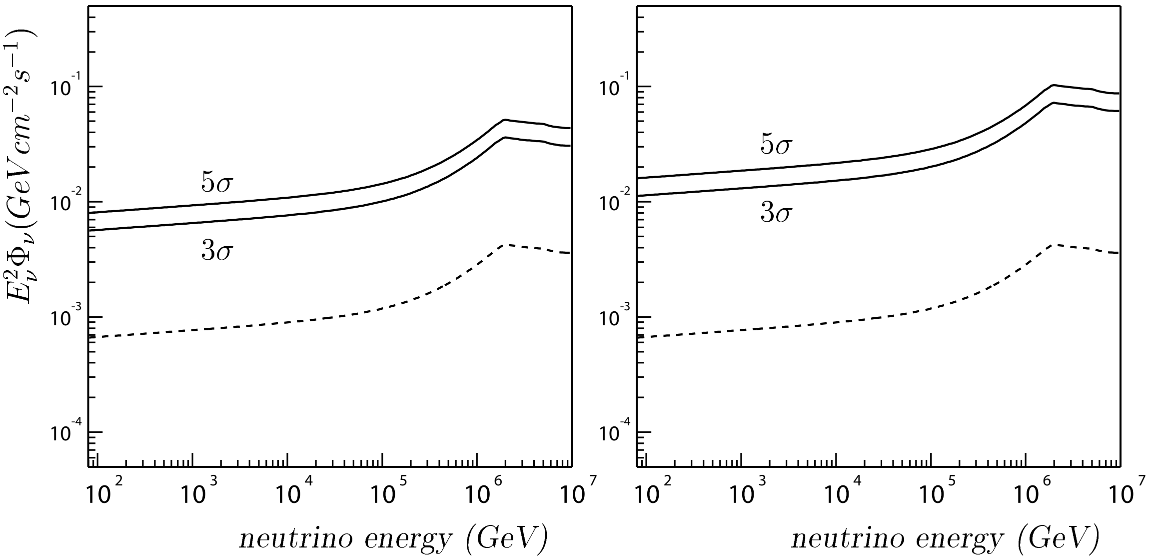

Figure 6.16: *Flux needed to detect one or more events from GRB 030329 for the 90% CL (left) and 99% CL (right). The background levels are at 3σ and 5σ for a data sample covering 4 minutes. The dashed line indicates the total neutrino flux from GRB 030329 for the scenario with the burst, supranova, and early afterglow components, shown separately in figure 1.5.*

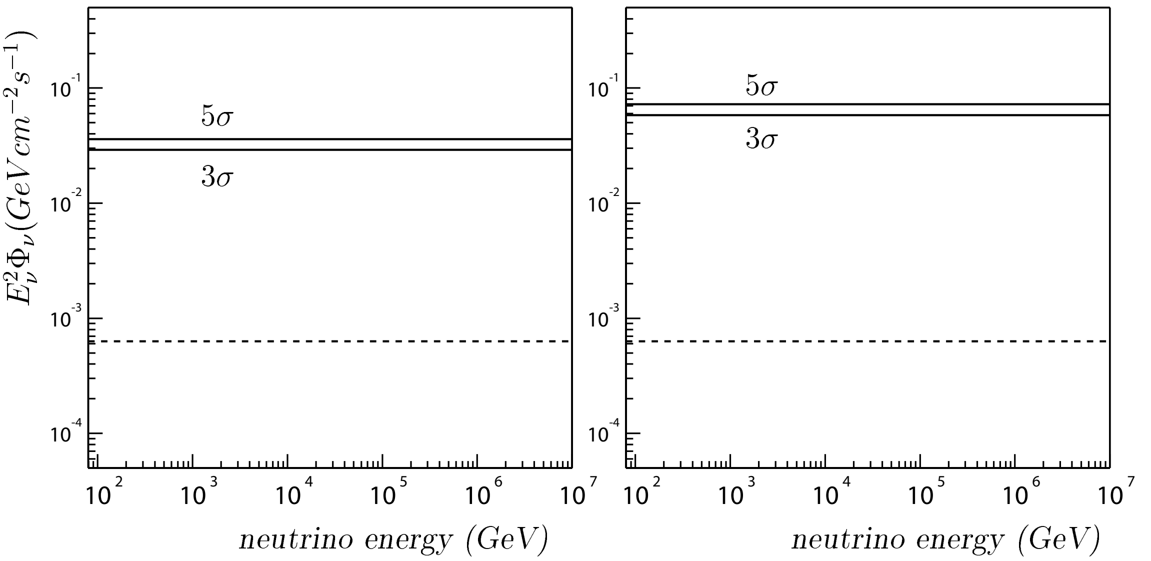

Figure 6.17: *Flux needed to detect one or more events from an average GRB with redshift 1 and a duration of 10 seconds for the 90% CL (left) and 99% CL (right). The background levels are 3σ and 5σ for a data sample covering 30 seconds. The dashed line indicates the estimated neutrino flux from such a GRB [99].*

the 3σ and 5σ background levels for a data sample covering 30 seconds.

The estimated required fluxes and the stated number of detected neutrinos are of course model dependent. Considering the expected rate of at least 100 GRBs per year that will be detected by satellites, at least one event should be detected after one year, taking into account that half of the GRBs will be below the horizon for the ANTARES site at the moment they occur. The discovery potential will even increase knowing that Swift is sensitive to short bursts, for which the background is reduced considerably. The methods developed and described in this work yield a significantly higher probability for detecting a neutrino from a GRB compared to other methods. If these methods are also used in future neutrino telescopes [10, 11], the discovery potential of these experiments would increase as well.

Chapter 7

Summary and conclusions

In this thesis new methods are described that are used to detect neutrinos from gamma-ray bursts with a neutrino telescope. These methods are devised and developed in the framework of the ANTARES experiment. A quantification of the ability to detect neutrinos from gamma-ray bursts is done for this experiment. The methods can also be incorporated in future neutrino experiments that are capable of detecting high-energy neutrinos.

Gamma-ray bursts (GRBs) are short and very intense flashes of MeV gamma rays. The moment of the GRB event and its location on the sky are unpredictable. GRBs occur at very large distances; the mean measured redshift is 1.3, which corresponds to a distance of 2.5 Gpc. The emission of gamma rays is often followed by an afterglow of lower energy photons that can last for months. Since the discovery of GRBs by satellites, about thirty years ago, thousands of GRBs have been detected by satellites dedicated to the detection and study of GRBs. The origin of GRBs remained unclear for many years. A better understanding of GRBs was obtained when it became possible to observe the afterglow. The afterglow is studied using ground based telescopes which are sensitive to other wavelength regions than the gamma-ray instruments on board satellites. Nowadays also satellite instruments are used to study the afterglow. The afterglow can only be observed under certain circumstances. First of all, knowledge of the position of the GRB with an accuracy of the order of a few arcminutes is required to be able to point a telescope in the right direction. Also, as the afterglow fades quickly, the telescope has to be pointed in the right direction when the GRB signal is still being detected, or shortly after that. Therefore the occurrence of a GRB has to be announced as quickly as possible. To meet these requirements, GRB warning systems have been developed. These systems distribute a message announcing the occurrence of the GRB around the world as soon as a GRB candidate is detected by a satellite. Also the location of the GRB on the sky is distributed in this way.

After many years of GRB research it became clear that a GRB is related to a relativistic jet. The underlying physics of a relativistic jet and its composition are not very well understood. It is generally believed that jets are capable of accelerating charged particles to very high energies, but the acceleration mechanism is not clear. It is concluded from the observations that electrons, positrons, and photons are present in the jet. It is also suggested by different models that baryons play an important role. If the presence of baryonic matter in relativistic jets is confirmed, the acceleration mechanism will be better understood. In this way, information could be obtained about the origin of GRBs. It has already been noticed that some GRBs can be associated with a supernova explosion, but not all. The knowledge of GRBs can be improved by the detection of neutrinos. Neutrinos would indicate the presence of baryons in jets, and thus explain more about the acceleration processes, and the physics processes that cause the GRB.

The neutrinos produced by GRBs are expected to have high energies. High-energy neutrinos can be detected by a detector like ANTARES. The ANTARES detector will be built on the bottom of the Mediterranean Sea, and it will consist of 12 vertical strings, each with a length of about 500 m. The strings are at a spacing of 60 m from each other, and together they cover a surface area of about 0.03 km^2. Each line is equipped with 75 photomultiplier tubes (PMTs). The PMTs are grouped in triplets, which are spread over the length of the string. When a high-energy neutrino undergoes a charged current interaction near the detector, the charged lepton that emerges moves with relativistic speed through the water. When it does this, it emits Cherenkov light that can be detected by the PMTs. Mainly muon neutrinos are considered, as the muon that emerges from the interaction can travel large distances.

The signal detected by the PMTs is digitised off-shore, and the raw data are sent to shore. This is known as the all-data-to-shore concept, which is specific to the ANTARES experiment. The data stream from the detector is distributed over a farm of PCs. Each PC has a filter program running, which has an algorithm implemented that looks for space-time correlations in the data. This is done using the known positions of the PMTs, and the measured arrival times of the Cherenkov photons. The filter processes run in parallel and filter the physics signal from the background continuously. This has to be done in real time because the detector will operate 24 hours a day. The filtering is necessary to reduce the data to a manageable amount for the detailed data analysis. Only the data that are considered as physics signal are stored on disk.

The all-data-to-shore concept in combination with the GRB warning systems make it possible to apply a different way of data taking at the moment a GRB occurs. When a GRB is detected by a satellite, a message is distributed by these warning systems. Just like these messages are distributed to astronomy observatories, they are also distributed to the ANTARES site. The aim is then to keep all raw data that were taken during the GRB event to prevent any signal being lost in the filter process. So at the moment such an alert message arrives, all filter programs will react and stop filtering. Instead, all raw data that are detected from that moment on are saved to disk. This situation will continue for a few minutes, as the neutrino signal from a GRB is expected to arrive within a few burst durations, and most

GRBs have a duration of less than 1 minute. After this period the system goes back to the normal situation where the data are filtered online. It is also possible to buffer the raw data using the memories of the PCs. The maximum period that can be covered depends on the number of PCs, the size of their memory, and the data output rate of the detector. Under normal conditions and with the current technology this period can be several minutes. The buffered data will cover the delays in the warning systems and a possible early neutrino signal. So not only all data following the GRB alert message, but also the raw data that were taken before the alert message arrived (even before the GRB was detected) will be stored on disk. All raw data covering a few minutes around the burst are thus available, including any possible neutrino signal that is correlated to the GRB. Because of the high data output rate of the detector, this special way of data taking is only possible for a short period. This way of data taking will be applied on average once a day, as this is the frequency at which the alert messages are typically received. The GRB warning systems also distribute the location of the GRB on the sky. This location corresponds to the direction of the neutrinos emitted by the GRB, and thus to the direction of the muons emerging from the neutrino interaction. With the launch of new satellites, the location of the GRB is distributed within a few minutes of the GRB occurrence with an accuracy of the order of a few arcminutes. When the message containing the location of the GRB has arrived, an offline filter method is applied to the raw data that are stored on disk. This method takes into account the known direction of the neutrinos. This filter also separates the physics signal from the background, but the found physics events primarily come from the direction of the GRB. As in the case of standard filtering, only the physics events are stored on disk for further analysis.

The performance of the special data taking method and the new filter method is evaluated with simulated data. The new filter method yields a higher efficiency than when the standard filter method is used. However, the event rate is increased. Most of the events found are due to accidental correlations in the random background. In this thesis, it is assumed that the random background corresponds to a singles rate of 70 kHz per PMT. Reports of several tests have however shown that the singles rate at the ANTARES site can be much higher due to the bioluminescence activity in the seawater. This has an effect on the amount of data that can be buffered, the performance of the filter, and the resulting event rate. The effect of an increase in the singles rates has already been studied for the standard filter method [100]. Adjusting the filter requirements to the high rates decreases the efficiency. The effect on the methods described is not quantified yet. Although many events are found that are caused by the random background, most of them will be rejected in the next step of the analysis. The efficiency of the new filter method is about 82%, compared to an efficiency of about 55% for the standard filter method. The efficiency depends on the direction of the neutrino and the neutrino energy. The detector is in general less sensitive to neutrinos that traverse the detector horizontally because of the geometry of the detector.

The increased efficiency can only be obtained with the all-data-to-shore concept in combination with the GRB warning systems. The real time warning systems are used for the purpose they are designed for, but then applied to neutrino astronomy. There is currently no other neutrino telescope that can do this. The detection efficiency of the methods described relies greatly on the performance of the real time warning systems. These systems are optimised for regular astronomy. Astronomers need the initial message that announces the GRB quickly to be able to observe the GRB afterglow. But this message is only of use if it is accompanied by the accurate location of the GRB. Of all satellites, Swift has the highest GRB detection rate. It will be the most important satellite for the ANTARES experiment in the coming few years. For this satellite it is decided to determine the position of the GRB before sending a message. So the initial message already contains the position. This however introduces an extra delay. The extra delay is a drawback for the detection of neutrinos from GRBs. For neutrino astronomy the initial alert message is needed instantly to save all data to disk that could include a neutrino signal. The accurate location of the GRB is also required, but this information is needed later, when all necessary data are safely stored on disk. Moreover, a less accurate location than that which is required in astronomy is sufficient for neutrino astronomy. So at this point, astronomers and neutrino physicists have conflicting interests. For neutrino astronomy the warning systems can be improved. It is crucial that the importance of these systems for neutrino astronomy gets more attention in the GRB community. When the specific needs for neutrino astronomy are better known, these requirements could also be taken into account for future GRB satellites, provided that the necessary changes in the warning systems or satellites have no effect on the science program of astronomers.

Although all physics events found by the filter method are compatible with only one specific direction, still many of these events are caused by background. Subsequent to the filtering of the data, a special GRB analysis method is applied to each of the events found, to be able to distinguish the neutrino signal from the background. This analysis method reconstructs the time and position of the muon path from the data assuming many different directions, including the GRB direction. The reconstruction of the event is repeated assuming each of these directions. For each muon path that is found, the likelihood is calculated. The likelihood ratio method is used to test if the event found is compatible with a neutrino from the GRB. With this method a neutrino signal can clearly be distinguished from the background: 80% of the signal is accepted, and 90% of the background is rejected.

When a final cut is applied to the likelihood ratio quantity provided by the analysis method, a discovery can be made if sufficient events remain. For one specific GRB, namely GRB 030329, the required number of events was calculated using the new methods and compared to the results obtained by the standard methods. The value of the cut was chosen such that the probability that one or more background events remain was smaller than 2.7×10^{-3} (3σ) or 5.7×10^{-7} (5σ). For the new methods (special data taking, special filter method, special GRB analysis method) the total efficiency is found to be 52% (35%) for a 3σ (5σ) background free event sample. This efficiency is normalised to the number of events that caused at least 6 detected Cherenkov photons. For the standard methods the total efficiency is 27% for a 3σ background free event sample. With the new methods the effective volume of the detector is increased by a factor of 1.5–10, depending on the neutrino energy. At the 3σ background level the effective volume exceeds 1 km^3 for neutrino energies above 400 TeV. For this particular GRB, simulations show that 0.5 events would cause at least 6 detected photons using a model prediction of the neutrino flux. Given the efficiency, this amounts to 0.27 detected events at the 3σ background level using the new methods. With the new methods the sensitivity of the ANTARES detector is increased by a factor of 2 compared to the standard methods.

The gain in efficiency of the new filter method is in particular remarkable at low neutrino energies. However, in any analysis method, the distinction between signal and background is difficult to make at low energies. Therefore, few low-energy events remain after the final cut in the analysis is applied. It is also shown that a small fraction of high-energy events cannot be distinguished from the background. Considering the large number of detected photons that these events produce, the analysis could be improved.

The increase in the discovery potential is also achieved because of the short duration of a GRB. As for each GRB a data sample covering only a few minutes is analysed (the special data taking lasts for only a few minutes) the background is limited. The main advantage here is the reduction of background from atmospheric neutrinos. These neutrinos produce the same signal in the detector as the neutrinos emitted by a GRB. However, the probability that there is an atmospheric neutrino from the same direction as the GRB at the time of the GRB event is very small. Another advantage that arises from the short duration of a GRB is the simplification of the calibration of the detector. The performance of the filter and analysis methods rely on the accurate knowledge of the positions of the PMTs. Because of the water flow, these positions change with time, and a calibration has to be done regularly during normal data taking to determine these positions. For the filtering and analysis of the GRB data this is not needed, as the positions of the PMTs are not expected to change significantly during the short period of the GRB. Therefore a single set of calibrations can be used for one GRB.

The stated number of events detected from GRB 030329 are specific to this burst. The detection efficiency will be different for each GRB, as each GRB is unique. The discovery potential depends on the neutrino flux, the distance of the GRB, and the detection efficiency. Another factor that plays an important role in both the detection efficiency and the discovery potential is the duration of the GRB, that is also different for each GRB. The time during which the special data taking is applied is fixed to a few minutes. The analysis method is applied to the whole data sample. Some time after the GRB, the duration of the GRB is known. This duration can appear to be very short compared to the period covered by the data sample. In this case, a fraction of the entire data sample can be selected for the final analysis.

The selected data sample covers a few burst durations, and should coincide with the gamma-ray signal. This reduces the background proportionally. This results in an increase of the efficiency by a factor of 1.5–3 (depending on the neutrino energy) for bursts with a duration of 1 second.

Although the same GRB event will never be repeated, the methods described can still be used to repeat the experiment for a specific GRB. The same filter method and analysis can be applied to the data that were taken in the same way, but at a different moment. In this way, more statistics on the background are obtained and this results in a better distinction between the neutrino signal and the background.

The new methods can also be used for the detection of neutrinos from non-transient sources for which the location on the sky is known. The same data analysis method can be used. With some small changes in the requirements of the filter method, and extra PCs, it is possible to filter data online, looking only in the direction of a specific source. As the filter requirements have to be adjusted to be able to do this, the filter efficiency will be lower than in the case for GRBs. The atmospheric neutrino background will play a more important role when the sources are observed over a long period. During the observation of a non-transient source in this way, the direction of the incident neutrinos changes with time. Therefore, the assumed neutrino direction has to be adjusted regularly taking into account the field of view of about 6°.

The methods described offer a great potential for the detection of neutrinos from sources for which the location on the sky is known, especially GRBs. The current GRB detection rate by satellites is about 100 per year, and this number is expected to increase with future GRB satellites. The methods described in this work make it possible to obtain a measurable signal from GRBs within one year of data taking. The methods also open up the possibility of measuring the neutrino flux of each gamma-ray burst with future cubic kilometre size neutrino telescopes.

References

[1] K. Hirata et al., *Observation of a Neutrino Burst from the Supernova SN1987A.* Phys. Rev. Lett. **58** (1987) 1490

[2] R. M. Bionta et al., *Observation of a Neutrino Burst in Coincidence with Supernova SN1987A in the Large Magellanic Cloud.* Phys. Rev. Lett. **58** (1987) 1494

[3] J. N. Bahcall and R. Davis, *Solar Neutrinos: A Scientific Puzzle.* Science **191** (1976) 264

[4] Q. R. Ahmad et al., *Direct Evidence for Neutrino Flavor Transformation from Neutral-Current Interactions in the Sudbury Neutrino Observatory.* Phys. Rev. Lett. **89** (2002) 011301

[5] J. G. Learned and K. Mannheim, *High-Energy Neutrino Astrophysics.* Annu. Rev. Nucl. Part. Sci. **50** (2000) 679

[6] P. Bhattacharjee and G. Sigl, *Origin and Propagation of Extremely High Energy Cosmic Rays.* Phys. Rept. **327** (2000) 109

[7] E. Andres et al., *The AMANDA neutrino telescope: principle of operation and first results.* Astropart. Phys. **13** (2000) 1

[8] V. A. Balkanov et al., *The Lake Baikal neutrino experiment.* Nucl. Phys. B (Proc. Suppl.) **87** (2000) 405

[9] P. Grieder, *Nestor Neutrino Telescope Status Report.* Nucl. Phys. Proc. Suppl. **97** (2001) 105

[10] A. Karle et al., *IceCube – the next generation neutrino telescope at the South Pole*, 2002. 20th International Conference on Neutrino Physics and Astrophysics

[11] http://km3net.org

[12] R. W. Klebesadel et al., *Observations of gamma-ray bursts of cosmic origin.* Astrophys. J. **182** (1973) L85

[13] N. Gehrels et al., *The Compton Gamma Ray Observatory.* Scient. Am. **269** (1993) 68

[14] G. J. Fishman et al., *The first BATSE gamma-ray burst catalog.* Astrophys. J. Suppl. **92** (1994) 229

[15] C. A. Meegan et al., *Spatial distribution of* γ*-ray bursts observed by BATSE.* Nature **355** (1992) 143

[16] C. Kouveliotou et al., *Identification of two classes of gamma-ray bursts.* Astrophys. J. **413** (1993) L101

[17] L. Scarsi et al., *SAX overview.* Astron. Astrophys. Suppl. Ser. **97** (1993) 371

[18] J. van Paradijs et al., *Gamma-Ray Burst Afterglows.* Annu. Rev. Astron. Astrophys. **38** (2000) 379

[19] J. I. Katz, *The Biggest Bangs.* Oxford University Press, 2002

[20] M. R. Metzger et al., *Spectral constraints on the redshift of the optical counterpart to the gamma-ray burst of 8 May 1997.* Nature **387** (1997) 878

[21] T. J. Galama et al., *An unusual supernova in the error box of the gamma-ray burst of 25 April 1998.* Nature **395** (1998) 670

[22] J. Hjorth et al., *A very energetic supernova associated with the* γ*-ray burst of 29 March 2003.* Nature **423** (2003) 847

[23] B. Zhang and P. Mészáros, *Gamma-Ray Bursts: Progress, Problems & Prospects.* Int. J. Mod. Phys. **A19** (2004) 2385

[24] T. Piran, *Gamma-Ray Bursts and the Fireball Model.* Phys. Rep. **314** (1999) 575

[25] A. I. MacFadyen and S. E. Woosley, *Collapsars: Gamma-Ray Bursts and Explosions in Failed Supernovae.* Astrophys. J. **524** (1999) 262

[26] R. Narayan et al., *Gamma-Ray Bursts as the Death Throes of Massive Binary Stars.* Astrophys. J. **395** (1992) L83

[27] J. E. Rhoads, *How to Tell a Jet from a Balloon: A Proposed Test for Beaming in Gamma-Ray Bursts.* Astrophys. J. **487** (1997) L1

[28] M. J. Rees and P. Mészáros, *Unsteady outflow models for cosmological gamma-ray bursts.* Astrophys. J. **430** (1994) L93

[29] P. Mészáros and M. J. Rees, *Relativistic fireballs and their impact on external matter - Models for cosmological gamma-ray bursts.* Astrophys. J. **405** (1993) 278

[30] M. S. Longair, *High Energy Astrophysics: Stars, the Galaxy and the interstellar medium*, Vol. 2. Cambridge University Press, 1994

[31] C. Akerlof et al., *Observation of contemporaneous optical radiation from a γ-ray burst.* Nature **398** (1999) 400

[32] A. Dar and A. De Rújula, *Towards a complete theory of Gamma Ray Bursts.* Phys. Rept. **405** (2004) 203

[33] S. Razzaque et al., *Neutrino Tomography of Gamma Ray Bursts and Massive Star Collapses.* Phys. Rev. D **68** (2003) 083001

[34] A. Dar and A. De Rújula, *The Cannonball Model of Gamma Ray Bursts: high-energy neutrinos and γ-rays.* astro-ph/0105094, 2001. CERN-TH/01-121

[35] S. Razzaque et al., *High Energy Neutrinos from Gamma-Ray Bursts with Precursor Supernovae.* Phys. Rev. Lett. **90** (2003) 241103

[36] B. Paczyński and G. Xu, *Neutrino bursts from gamma-ray bursts.* Astrophys. J. **427** (1994) 708

[37] E. V. Derishev et al., *The Neutron Component in Fireballs of Gamma-Ray Bursts: Dynamics and Observable Imprints.* Astrophys. J. **521** (1999) 640

[38] E. Waxman and J. Bahcall, *High Energy Neutrinos from Cosmological Gamma-Ray Burst Fireballs.* Phys. Rev. Lett. **78** (1997) 2292

[39] E. Waxman and J. Bahcall, *Neutrino afterglow from Gamma-Ray Bursts: $\sim 10^{18}$ eV.* Astrophys. J. **541** (2000) 707

[40] S. Razzaque et al., *Neutrino signatures of the supernova - gamma ray burst relationship.* Phys. Rev. D **69** (2004) 023001

[41] S. D. Wick et al., *High-Energy Cosmic Rays from Gamma-Ray Bursts.* Astropart. Phys. **21** (2004) 125

[42] Z. G. Dai and T. Lu, *Neutrino Afterglows and Progenitors of Gamma-Ray Bursts.* Astrophys. J. **551** (2001) 249

[43] Z. Li et al., *Long-term Neutrino Afterglows from Gamma-Ray Bursts.* Astron. Astrophys. **396** (2002) 303

[44] F. Halzen and D. W. Hooper, *Neutrino Event Rates from Gamma-Ray Bursts.* Astrophys. J. **527** (1999) L93

[45] J. Alvarez-Muñiz et al., *High energy neutrinos from gamma ray bursts: Event rates in neutrino telescopes.* Phys. Rev. D **62** (2000) 093015

[46] D. Guetta and J. Granot, *Neutrinos of Energy* $\sim 10^{16}$ *eV from Gamma-Ray Bursts in Pulsar Wind Bubbles.* Phys. Rev. Lett. **90** (2003) 201103

[47] D. Guetta and J. Granot, *Neutrinos from Pulsar Wind Bubbles as Precursors to Gamma-Ray Bursts.* Phys. Rev. Lett. **90** (2003) 191102

[48] D. Band et al., *BATSE observations of gamma-ray burst spectra. I – Spectral diversity.* Astrophys. J. **413** (1993) 281

[49] S. D. Barthelmy et al., *GRB Coordinates Network (GCN): A Status Report.* Proc. of the 5th Huntsville GRB Workshop, AIP Conference Series **526** (2000) 731

[50] G. R. Ricker et al., *The High Energy Transient Explorer (HETE): Mission and Science Overview.* AIP Conference Proc. **662** (2003) 3

[51] C. Winkler et al., *The INTEGRAL mission.* Astron. Astrophys. **411** (2003) L1

[52] N. Gehrels et al., *The Swift Gamma-Ray Burst Mission.* Astrophys. J. **611** (2004) 1005

[53] N. Gehrels and P. Michelson, *GLAST: the next-generation high energy gamma-ray astronomy mission.* Astropart. Phys. **11** (1999) 277

[54] V. Cocco et al., *The science of AGILE: part I & II.* Nucl. Phys. B (Proc. Suppl.) **113** (2002) 231

[55] R. Vanderspek et al., *What HETE sends to the GCN.* AIP Conference Proc. **662** (2003) 101

[56] S. Mereghetti et al., *The INTEGRAL Burst Alert System.* Astron. Astrophys. **411** (2003) L291

[57] K. Hurley et al., *The Current Performance of the Third Interplanetary Network.* AIP Conference Proc. **662** (2003) 473

[58] D. Griffiths, *Introduction to elementary particles.* John Wiley & Sons, 1987

[59] M. A. Markov, *On high energy neutrino physics*, 1960. Proc. of the Int. Conf. on High Energy Physics, Rochester

[60] J. D. Jackson, *Classical Electrodynamics.* John Wiley & Sons, 1998

[61] J. A. Aguilar et al., *Transmission of light in deep sea water at the site of the ANTARES neutrino telescope.* Astropart. Phys. **23** (2005) 131

[62] Particle Data Group, *Passage of particles through matter.* Eur. Phys. J. **C15** (2000) 163

[63] J. G. Learned and S. Pakvasa, *Detecting ν_τ Oscillations at PeV Energies.* Astropart. Phys. **3** (1995) 267

[64] P. Amram et al., *The ANTARES optical module.* Nucl. Instrum. Meth. **A484** (2002) 369

[65] F. Feinstein, *The analogue ring sampler: A front-end chip for ANTARES.* Nucl. Instrum. Meth. **A504** (2003) 258

[66] D. J. L. Bailey, *Monte Carlo tools and analysis methods for understanding the ANTARES experiment and predicting its sensitivity to Dark Matter.* Ph.D. thesis, Wolfson College, Oxford, 2002

[67] G. Ingelman et al., *LEPTO 6.5 - A Monte Carlo Generator for Deep Inelastic Lepton-Nucleon Scattering.* Comput. Phys. Commun. **101** (1997) 108

[68] T. Sjöstrand, *High-energy-physics event generation with PYTHIA 5.7 and JETSET 7.4.* Comput. Phys. Commun. **82** (1994) 74

[69] H. L. Lai et al., *Global QCD analysis and the CTEQ parton distributions.* Phys. Rev. D **51** (1995) 4763

[70] R. Gandhi et al., *Ultrahigh-Energy Neutrino Interactions.* Astropart. Phys. **5** (1996) 81

[71] I. A. Sokalski et al., *MUM: Flexible precise Monte Carlo algorithm for muon propagation through thick layers of matter.* Phys. Rev. D **64** (2001) 074015

[72] S. Navas and L. Thompson, *KM3 User Guide and Reference Manual*, 1999. ANTARES internal note Soft/1999-11

[73] L. A. Kuzmichev, *On the velocity of light signals in deep underwater neutrino experiments.* Nucl. Instrum. Meth. **A482** (2002) 304

[74] Application Software Group, *Detector description and simulation tool*, 1993. CERN Program Library Writeup W5013

[75] P. Antonioli et al., *A three-dimensional code for muon propagation through the rock: MUSIC.* Astropart. Phys. **7** (1997) 357

[76] J. Wentz et al., *Simulation of atmospheric muon and neutrino fluxes with CORSIKA.* Phys. Rev. D **67** (2003) 073020

[77] N. N. Kalmykov et al., *Quark-Gluon-String Model and EAS Simulation Problems at Ultra-High Energies.* Nucl. Phys. B (Proc. Suppl.) **52B** (1997) 17

[78] B. Wiebel-Sooth et al., *VII: Individual element spectra: prediction and data.* Astron. Astrophys. **330** (1998) 389

[79] E. V. Bugaev et al., *Atmospheric Muon Flux at Sea Level, Underground and Underwater.* Phys. Rev. D **58** (1998) 054001

[80] V. Agrawal et al., *Atmospheric neutrino flux above 1 GeV.* Phys. Rev. D **53** (1996) 1314

[81] M. Thunman et al., *Charm production and high energy atmospheric muon and neutrino fluxes.* Astropart. Phys. **5** (1996) 309

[82] J. Brunner, *Simulation of* ^{40}K *signals*, 1999. ANTARES internal note Site/1999-2

[83] A. Heijboer, *Track reconstruction and point source searches with ANTARES.* Ph.D. thesis, University of Amsterdam, 2004

[84] R. Gurin and A. Maslennikov, *ControlHost: Distributed Data Handling Package*, 1995. Available on `/afs/caspur.it/project/ControlHost/`

[85] R. Brun and F. Rademakers, *ROOT - An Object Oriented Data Analysis Framework.* Nucl. Instrum. Meth. **A389** (1997) 81

[86] P. J. Lucas, *An Object-Oriented Language System for Implementing Concurrent, Hierarchical, Finite State Machines*, Technical report UIUCDCS-R-94-1868, University of Illinois at Urbana-Champaign, 1993, available on `http://homepage.mac.com/pauljlucas/software/chsm/`

[87] M. Bouwhuis, *RunControl user manual*, 2003. ANTARES internal note Soft/2003-4

[88] M. Circella, *Toward the ANTARES Neutrino Telescope: Results from a Prototype Line*, 2003. Proc. 28th Int. Cosmic Ray Conf.

[89] E. F. Codd, *A Relational Model of Data for Large Shared Data Banks.* Commun. ACM **13** (1970) 377

[90] B. W. Caroll and D. A. Ostlie, *An Introduction to Modern Astrophysics.* Addison Wesley, 1996

[91] W. H. Press et al., *Numerical Recipes in C.* Cambridge University Press, 1988

[92] F. Aharonian et al., *Very high energy gamma rays from the direction of Sagittarius A*.* Astron. Astrophys. **425** (2004) L13

[93] F. Aharonian et al., *Very high energy gamma rays from the composite SNR G0.9+0.1.* Astron. Astrophys. **432** (2005) L25

[94] F. Aharonian et al., *High-energy particle acceleration in the shell of a supernova remnant.* Nature **432** (2004) 75

[95] Z. Bern et al., *Neutralino annihilation into two photons.* Phys. Lett. B **411** (1997) 86

[96] D. Hooper and J. Silk, *Searching for dark matter with neutrino telescopes.* New J. Phys. **6** (2004) 23

[97] E. Waxman, *Probing Microquasars with TeV Neutrinos.* Phys. Rev. Lett. **87** (2001) 171101

[98] E. Carmona, *Study of the event reconstruction and expected performances for point-like sources of the future ANTARES neutrino telescope.* Ph.D. thesis, University of Valencia, 2003

[99] E. Waxman, *private communication*

[100] B. A. P. van Rens, *The software trigger in ANTARES*, 2004. ANTARES internal note Soft/2004-1

Samenvatting

Het bestuderen van astronomische bronnen gebeurt voornamelijk door het detecteren van elektromagnetische straling. Uit de waarnemingen van elektromagnetische straling afkomstig uit het heelal is gebleken dat sommige bronnen zeer hoog-energetische fotonen uitzenden ($10^6 - 10^{12}$ eV). Deze energieën zijn veel hoger dan de energieën van fotonen die worden uitgezonden door een ster. Hoog-energetische fotonen zijn een direct gevolg van straling van geladen deeltjes. Blijkbaar zijn sommige bronnen in staat deeltjes te versnellen tot zeer hoge energieën. Hoe deze bronnen werken en hoe ze ontstaan is niet duidelijk. Verondersteld wordt dat de versnellingsmechanismen in een zogenaamde relativistische straal plaatsvinden. Relativistische stralen worden veroorzaakt door zeer compacte objecten in het heelal, die materie met hoge snelheid en in een nauwe bundel van zich af blazen. Hierbij kunnen de deeltjes die zich in die straal bevinden zeer hoge energieën krijgen.

Andere informatie van astronomische bronnen die zeer hoog-energetische deeltjes uitzenden hebben we uit de detectie van zeer hoog-energetische kosmische straling (10^{20} eV). Kosmische straling bestaat uit geladen deeltjes, vaak protonen, die de atmosfeer van de aarde binnenkomen. De oorsprong van deze deeltjes is niet goed bekend. Men denkt dat er een verband bestaat tussen relativistische stralen en hoog-energetische kosmische straling. Het zou namelijk kunnen dat in die relativistische stralen naast elektronen en positronen (die de waargenomen elektromagnetische straling veroorzaken), ook protonen worden versneld. Als dat bevestigd zou kunnen worden, dan zouden we te weten kunnen komen hoe het komt dat de deeltjes tot zulke gigantische snelheden worden versneld, en door wat voor soort objecten dat gebeurt.

De aanwezigheid van protonen in relativistische stralen is echter niet aan te tonen door detectie van alleen fotonen en protonen. Protonen hebben elektrische lading, en worden daardoor afgebogen door magneetvelden die ze op hun weg door het heelal tegenkomen. Dus de detectie van een kosmisch proton geeft geen informatie over waar hij vandaan komt. Neutrino's hebben dat probleem niet. Ze hebben geen elektrische lading, en ze vliegen vrijwel ongehinderd overal doorheen. Neutrino's worden geproduceerd wanneer hoog-energetische protonen met fotonen of andere protonen botsen. Wanneer een neutrino wordt gedetecteerd en zijn richting kan worden bepaald, dan staat ook vast waar hij is geproduceerd. Omdat men denkt dat een relativistische straal hoog-energetische protonen produceert, zou dat betekenen dat er ook hoog-energetische neutrino's uit moeten komen. Neutrino's zijn dus heel geschikt om astronomische bronnen te bestuderen die hoog-energetische deeltjes uitzenden. De detectie van hoog-energetische neutrino's uit deze bronnen zou meteen de aanwezigheid van protonen aantonen. Dan zouden ook de astrofysische processen die een rol spelen in deze bronnen duidelijker worden.

Een voorbeeld van een astronomisch verschijnsel dat wordt geassocieerd met een relativistische straal is een gammaflits. Gammaflitsen zijn korte en zeer intense flitsen van hoog-energetische fotonen. Deze flitsen duren ongeveer een minuut. De flitsen vinden plaats op willekeurige momenten en plaatsen in het heelal. Ze werden ongeveer dertig jaar geleden per toeval ontdekt door militaire satellieten. Sinds die tijd zijn er meerdere satellieten gelanceerd, speciaal bedoeld voor onderzoek naar gammaflitsen. Tegenwoordig worden er per jaar ongeveer 100 gammaflitsen gedetecteerd.

In het begin was het volkomen onduidelijk wat dit voor soort bronnen waren. Dit werd twintig jaar na de ontdekking duidelijker. Toen slaagde men er voor het eerst in om het zogenaamde nagloeien van een gammaflits te meten. Dat is een uitstoot van elektromagnetische straling die direct op de gammastraling volgt, maar deze fotonen hebben een lagere energie dan de fotonen van de gammaflits. Het nagloeien kan maanden duren. Toen het eenmaal mogelijk was om het nagloeien waar te nemen, werd ook duidelijk dat gammaflitsen zich op gigantische afstanden van de aarde bevinden.

Het nagloeien kan gedetecteerd worden met telescopen op aarde, die gevoelig zijn voor de golflengten van deze fotonen. Om de telescoop op de bron te kunnen richten moet op het moment dat de gammaflits afgaat de positie van de gammaflits aan de hemel bekend zijn. Deze informatie is heel snel nodig na het detecteren van de eerste gammastraling door de satelliet, omdat het nagloeien snel in intensiteit afneemt. Om deze informatie snel te verspreiden zijn waarschuwingssystemen ontwikkeld. De satellieten die gammaflitsen detecteren zijn geïntegreerd in deze systemen. Zodra een gammaflits wordt gedetecteerd, seint de satelliet een bericht naar de aarde. Dit bericht wordt via het internet de wereld rondgestuurd. De positie van de gammaflits aan de hemel wordt ook zo snel mogelijk op deze manier rondgestuurd.

Nog steeds zijn bepaalde fysische aspecten van gammaflitsen onduidelijk, ondermeer de eerdergenoemde relativistische stralen die ermee gepaard gaan. Waarschijnlijk worden samen met de gammastraling ook hoog-energetische neutrino's uitgezonden. De detectie van neutrino's die worden geassocieerd met gammaflitsen zou veel duidelijkheid verschaffen over de werking van zo'n relativistische straal.

In dit proefschrift worden nieuw ontwikkelde methoden beschreven om neutrino's uit gammaflitsen te detecteren. Deze methoden zijn ontwikkeld in het kader van het ANTARES experiment. De ANTARES detector is een neutrinodetector waarmee hoog-energetische neutrino's gedetecteerd kunnen worden. De detector wordt gebouwd op de bodem van de Middellandse zee, op een diepte van ongeveer 2.5 km. Hij bestaat uit 12 verticale lijnen, elk met een lengte van ongeveer 500 meter. De lijnen staan op gelijke afstand van elkaar, en zijn zo gerangschikt dat ze een oppervlakte van ongeveer 0.03 km^2 bestrijken. Elke lijn is uitgerust met 75 fotobuizen. De fotobuizen zijn gegroepeerd in drietallen, die weer op gelijke afstanden van elkaar aan de lijn zijn bevestigd. Op deze manier wordt een groot drie-dimensionaal rooster gemaakt met fotobuizen.

De neutrino's die worden geproduceerd tijdens een gammaflits kunnen de detector bereiken. Neutrino's worden echter niet direct gemeten. Soms ondergaat een neutrino een interactie met het zeewater waarbij geladen deeltjes ontstaan. Wanneer dit in de buurt van de detector gebeurt, dan bewegen die geladen deeltjes met hoge snelheid door het water waarbij ze detecteerbaar licht uitzenden. Dit wordt Cherenkov-licht genoemd. In het ANTARES experiment wordt bij voorkeur naar interacties van het muon-neutrino type gekeken waarbij een muon wordt geproduceerd. Een muon kan lange afstanden in water afleggen waarbij het veel Cherenkov-licht produceert. Het Cherenkov-licht kan door de fotobuizen gedetecteerd worden. Omdat de posities van de fotobuizen bekend zijn, en ook de aankomsttijden van de Cherenkov-fotonen, kan de richting van het muon gereconstrueerd worden. De richting van het muon komt nagenoeg overeen met de richting van het neutrino waar het uit voortkwam, en dus kan achterhaald worden waar het neutrino is geproduceerd. In principe staat de detector de hele tijd aan, 24 uur per dag. Er wordt dus continu in alle richtingen gezocht naar signalen die door een neutrino veroorzaakt kunnen worden.

Door gebruik te maken van de nieuw ontwikkelde methoden die beschreven staan in dit proefschrift wordt de gevoeligheid voor neutrino's die worden geassocieerd met gammaflitsen aanzienlijk vergroot. Hierbij wordt er gebruik gemaakt van de eerdergenoemde waarschuwingssystemen voor gammaflitsen. Het gebruik van deze systemen op de manier waarvoor ze zijn gemaakt wordt mede mogelijk gemaakt door het specifieke ontwerp van het dataverwerkingssysteem van de ANTARES detector. Door het experiment te koppelen aan de waarschuwingssystemen kan op het moment dat een gammaflits afgaat op een speciale manier data worden genomen. De detector kan dan worden beschouwd als een telescoop die in de richting van de gammaflits wordt gericht op het moment dat deze wordt gedetecteerd door een satelliet.

Door de voorkennis van de aankomsttijd en de richting van de neutrino's in de analysemethoden te gebruiken wordt de kans om een neutrino te detecteren veel groter. Een ander groot voordeel bij deze methoden is de korte duur van een gammaflits. Andere bronnen die door ANTARES bestudeerd worden schijnen altijd, en worden gedurende lange tijd geobserveerd, waardoor het achtergrondsignaal toeneemt. In het geval van een gammaflits is de achtergrond laag vanwege de korte duur van de flits.

Uit de resultaten van deze nieuwe methoden blijkt dat de gevoeligheid van de detector voor neutrino's die worden geassocieerd met gammaflitsen ongeveer twee keer zo hoog is als bij andere methoden. Bovendien kunnen de analysetechnieken ook goed gebruikt worden voor andere neutrinobronnen die altijd schijnen, en waarvan de plaats aan de hemel bekend is. Gezien de verkregen gunstige resultaten zijn deze methoden aan te bevelen bij de toekomstige neutrinodetectoren die nog veel groter zijn.

Dankwoord

De waardevolle adviezen die ik heb gekregen van veel mensen op het NIKHEF en het Sterrenkundig Instituut “Anton Pannekoek”, en van collega’s in de ANTARES collaboratie, hebben mij geholpen met het werk beschreven in dit proefschrift. Ik ben vooral veel dank verschuldigd aan Maarten de Jong.
In het bijzonder wil ik Karel Gaemers bedanken omdat hij mijn promotor wilde zijn, en Ger van Middelkoop omdat hij mij heeft aangenomen op het NIKHEF.